Doctorate Dissertation

博士論文

Buffer Layer-Enhanced Epitaxial Growth of Oxynitride Thin Films for Photoelectrochemical Applications

（光電気化学応用へ向けたバッファ層を用いた酸窒化物薄膜のエピタキシャル成長）

A Dissertation Submitted for Degree of Doctor of Philosophy

July 2018

平成 30 年 07 月博士（理学）申請

Department of Chemistry, Graduate School of Science,

The University of Tokyo

東京大学大学院理学系研究科化学専攻

MOTANEEYACHART Vitchaphol

モタニーヤシャート　ビッチャプール

Buffer Layer-Enhanced Epitaxial Growth of Oxynitride Thin Films for Photoelectrochemical Applications

by

Vitchaphol Motaneeyachart

Development of Chemistry
Graduate School of Science
The University of Tokyo

July 2018

Abstract

Photoelectrochemical (PEC) solar light-induced water splitting has received significant attention as a promising process for hydrogen and oxygen production with no greenhouse gas emission. Two fundamental requirements for an electrode material to achieve better photocatalytic efficiency are (1) visible light absorption with suitable band edge potentials for water splitting and (2) low amount of defects to reduce the recombination of photogenerated electrons and holes. Although transition metal oxides with d^0 electronic configuration have suitable band edge potentials for water splitting, most of them show large band gaps. Anion substitution is a way to overcome this problem through negative shift of the valence band maximum. Among the anion substituted oxides, oxynitrides are particularly promising for visible light-driven solar water splitting. However, oxynitrides obtained by conventional synthesis method, where bulk or polycrystalline film of precursor oxides are partially nitrided by high temperature ammonia, usually show high density of pores and defects on their surface. These surface defects have negative influence on the photocatalytic activity because they work as recombination centers. Therefore, to enhance the efficiency of PEC solar water splitting using an oxynitride, it is important to synthesize dense specimens with smooth surfaces and little defects. For this purpose, heteroepitaxial growth of single crystalline films is a promising method. In this study, I especially focused on the interface between oxynitride film and substrate, and attempted to improve the crystallinity and chemical stoichiometry of the films by inserting a self-seed layer for lowering crystallization temperature or inserting a buffer layer for reduction of the density of defects arising from lattice mismatch between the film and the substrate.

Firstly, I focused on a simple ternary oxynitride with d^0 electronic configuration, baddeleyite NbON, which is suggested to have a smaller bandgap than baddeleyite TaON (β-TaON), being one of the most widely studied oxynitrides with a bandgap of ~2.5 eV. NbO_xN_y thin films were deposited by nitrogen plasma assisted pulsed laser deposition (NPA-PLD) on (100) plane of yttria-stabilized zirconia (YSZ) substrates, of which lattice constants are matched with those of (100) plane of baddeleyite NbON. XRD measurements revealed that the films grown at Ts ≤475 ºC were amorphous whereas the films grew at Ts ≥500 ºC showed h00 diffraction peaks of baddeleyite structure, of which intensity increased with increasing Ts. However, the color of the film fabricated at high Ts (600 ºC) was black, indicating formation of a large amount of nitrogen deficiency. To overcome this dilemma, I introduced a self-seed layer of NbO_xN_y. As a result, a nearly stoichiometric film with a composition of $NbO_{0.89}N$ (nominal charge of Nb was +4.77) was successfully obtained.

The baddeleyite NbON thin film exhibited a bandgap of ~2.3 eV, which is smaller than that of β-TaON (2.5 eV) as expected. The NbON film showed n-type semiconducting behavior, of which electrical resistivity (ρ), carrier density (n), and mobility (μ_H) were 2.5×10^{-1} Ωcm, 1.5×10^{22} cm^{-3} and 1.6×10^{-3} cm^{2}V^{-1}s^{-1}, respectively, at room temperature. The high n_e value is attributable not only to the slight reduction of Nb (nominal charge of +4.77) but also to the presence of NbN_x phase as suggested by in-gap optical absorption. These results demonstrate the benefit of self-seed layer technique for low temperature epitaxial growth of baddeleyite NbON thin film, although slight reduction of Nb generated carriers.

Next, I focused on a perovskite-type quaternary oxynitride based on chemically stable Ta^{5+}, $BaTaO_2N$, with a small absorption edge (~1.9 eV). In this study, I fabricated $BaTaO_2N$ epitaxial thin films with improved crystallinity on STO substrate by inserting a $BaSnO_3$ (80 nm thick)/$Sr_{0.5}Ba_{0.5}SnO_3$ (10 nm thick) double layered buffer layer.

The $BaTaO_2N$ thin films directly grown on STO (001) substrate showed epitaxial growth of perovskite crystal with multiple orientation of (001) and (110). On the other hand, the film deposited on $BaSnO_3$/$Sr_{0.5}Ba_{0.5}SnO_3$ buffer layer exhibited epitaxial growth of (001)-oriented thin film with a suppressed but finite amount of (110) oriented grains, indicating improved crystallinity.

The $BaTaO_2N$ film grown directly on STO (110) substrate showed only the *hh*0 diffractions of perovskite crystal without any impurities such as Ta_2O_5, TaON and $BaTaO_x$. However, the crystallinity of the film was low (FWHM on (110)-oriented peak = ~1.25°). Furthermore, the surface of the film was rather rough, of which root-mean-square (RMS) roughness was ~5 nm. On the other hand, the $BaTaO_2N$ thin film fabricated on the $BaSnO_3$ buffer layer indicated epitaxial growth of a (110)-oriented perovskite $BaTaO_2N$ thin film. Notably, the crystallinity and the surface morphology of the film was much improved (FWHM on (110)-oriented peak = 0.3° and the RMS of surface roughness = ~1 nm) compared with the films directly grown on STO (110) substrate.

Then, I compared the physical properties of the $BaTaO_2N$ thin films grown directly on STO (110) substrate and those of the films grown on the $BaSnO_3$ buffer layer. Both of the films showed clear visible light absorption with absorption edges of ~1.9 eV, being consistent with the previous report. On the other hand, stronger absorption in visible light region with sharper absorption onset was observed in the $BaTaO_2N$ film grown on the $BaSnO_3$ buffer layer.

While the crystallinity, the surface morphology, and the optical properties were improved by using the $BaSnO_3$ buffer layer, defects in the film were not completely suppressed: Dielectric measurements of the films by using an LCR meter indicated large dielectric loss tangent even on the $BaSnO_3$ buffer layer, suggesting the existence of anion deficiency. Furthermore, the photoelectrochemical current measured by linear sweep voltammograms in aqueous solution (pH = 13, 0.1M Na_2SO_4) under visible light illumination was very low, although a small increase was observed by inserting the buffer layer. Further improvement of anion stoichiometry would be necessary for improving the PEC performance of the $BaTaO_2N$ film.

In summary, I have succeeded in synthesizing epitaxial thin films of narrow band gap oxynitrides, baddeleyite NbON and perovskite $BaTaO_2N$, by inserting a self-seed layer or a buffer layer. These results demonstrate that insertion of a seed/buffer layer with suitable crystal structure and lattice constants is an effective way to improve anion stoichiometry as well as crystallinity and surface morphology. Further optimization of anion stoichiometry is probably needed for enhanced electrical and PEC properties.

Acknowledgement

First and foremost I would like to express my gratitude to my supervisor, Professor Tetsuya Hasegawa for giving me an invaluable opportunity to study at the University of Tokyo under Solid State Chemistry laboratory and his constant support, advice and simulating discussions throughout the whole project and thesis. It has been an honor to be his student. I really appreciate all his precious time, knowledge and also research funding to make my Ph.D. study productive. Apart from collaborative and effective research environment, he also give advice on almost everything related studying in Japan. I am confident that this thesis has not been done in the right way without him.

I am also give special thanks to Associate Professor Yasushi Hirose who always give me very useful advices and supports me with patience and kindness through my research. He taught me from the principle of experimental devices thought out the forefront study. His way of thinking and ideas have inspired me to become the one like him. Without his support, I would not be able to attain this degree. His door is always open for me for research discussion even late night or weekends. He also and always help me prepared for manuscript submission, conference preparation and wrote a grant application for funding. I has been a great pleasure to have him as a mentor throughout the course.

I would also appreciate Assistant Professor Akira Chikamatsu, Dr. Hideyuki Kamisaka and Dr. Shoichiro Nakao, Dr. Tsukasa Katayama, and Dr. Yang Chang for their kindness and generous advice to support me in experimental techniques, research discussion and conference presentations. I also would like to acknowledge to members in Ishitani-Maeda laboratories from Tokyo Institute of Technology for their support and gave me a precious opportunity in measuring photoelectrochemical water splitting of my samples. I am also give my thanks to Mr. Takuto Wakasugi for his technical help in photoelectrochemical measurement in sample preparation, experimental construction and data calculation. I would also like to appreciate Mr. Satoshi Fujiwara for his helps in Elastic Recoil

Detection Analysis and Rutherford Backscattering Spectroscopy analysis and calculation. I would like to thank Dr. Daichi Oka, Dr. Atsushi Suzuki, Dr. Thantip S. Krasienapibal and Dr. Masahito Sano for their support in my early research and living here in Japan.

Special thanks go to secretaries in our laboratory, Ms. Mie Umino, Ms. Miki Komazawa and Ms. Aya Imoji for their support in preparation for my university and financial documents.

The members in the Hasegawa laboratory have contributed immensely to my research and personal life. This group has high levels of collaboration and international student-friendly. I would like to thanks all members in this laboratory: Dr. Sohei Okazaki, Dr. Daisuke Ogawa, Dr. Youngok Park, Dr. Kei Shigematsu, Dr. Jie Wei, Dr. Shungo Kojima, Dr. Jeon Il, Dr. Mayuko Oka, Dr. Ryosuke Sei, Dr. Tomoya Onozuka, Dr. Kenichi Kaminaga, Mr. Jumpei Takahashi, Mr. Kyohei Yamatake, Mr. Keisuke Kawahara, Mr. Yuji Kurauchi, Mr. Fahd S. Kahn, Mr. Yutaka Uchida, Mr. Dai Kutsuzawa, Mr. Takuma Takeda, Mr. Takanori Yamazaki, Mr. Shunsuke Shibata, Mr. Naoki Kashiwa, Mr. Naoaki Hashimoto, Mr. Keisuke Yamada, Mr. Toru Koizumi, Mr. Takaaki Shiina, Mr. Michitaka Fukumoto, Mr. Takahiro Maruyama, Ms. Zhu Yuting, Mr. Ruocheng Han, Mr. Shunya Tanaka, Mr. Ken Hayahara, Mr. Shishin Mo, Mr. Kuni Yamada, Mr. Jin Gou, Mr. Gu Ke, Mr. Zhong Jiangnan, Mr. Ryosuke Ishigami, Mr. Takuya Sahashi, Mr. Masato Tsuchii and Mr. Kento Magara for their supports and research instrumentals assistance.

I have appreciated and would like to give special thanks to Japanese government (Monbukagakusho) scholarships for my financial support for 5 years throughout my master's and Ph.D. studies at the University of Tokyo. Moreover, I want to thank Marubun Research Promotion Foundation for their support for my international conference trip during my Ph.D. course.

Lastly, I would like to express my sincere gratitude to my parents, my brother, and my beloved for their constant support me and their understanding even while I lived far away, especially my mom who is always be there and stood by me during the hardest years of my study life. She has listened whatever has been bothering me and made sure that I still have the chance to go on. I own my life for her constant love and moral supports.

I am very much pleased regarding my degree, I have learned a tremendous amount over 5 years by staying here.

"*We set sail on this new sea because there is new knowledge to be gained, and new rights to be won, and they must be won and used for the progress of all people. Not because it is easy, but because they are hard; because that goal will serve to organize and measure the best of our energies and skills, because that challenge is one that we are willing to accept, one we are unwilling to postpone, and one we intend to win, and the others, too*" – JFK's speech, Rich University, 1962

July, 2018

Vitchaphol Motaneeyachart

Contents

Chapter 1

General introduction

1.1 Semiconductor photocatalysis

Globally, major energy sources are relied on fossil fuels such as oil and coal. These energy resources have brought an important role in many large-scale industries and transportation. Nevertheless, fossil fuels have a marked influence on our atmosphere with releasing carbon dioxide and other global warming gases. These gases in the atmosphere result in an increase in the amount of heat on the Earth's surface. One way to solve this problem is using solar power as a source to produce an energy. Photocatalytic semiconductor is one of the materials that have been paid much attention as clean and efficient materials to transform solar energy into chemical energy (hydrogen) without emitting greenhouse gases.

In the early 1970s, Honda and Fujishima, for the first time, demonstrated the water splitting effect by using TiO_2 electrode, i.e., decomposition of water into hydrogen and oxygen gases with UV light [1]. Many recent studies have focused on d^0 transition metal cations (Ti^{4+}, Zr^{4+}, Nb^{5+}, Ta^{5+} and W^{6+}) because the locations of their conduction bands are suitable for water splitting redox reaction. Table 1.1 shows d^0 transition metal oxides with photocatalytic activity under UV irradiation. The valence bands of oxides are generally electropositive so that most of them show large band gaps, resulting in high photoactivity only to the UV light. Anion substitution is a way to overcome this problem through the shift of the valence band maximum to higher energy side and thus narrowing of band gap. This smaller band gap achieves maximum absorption ability in the visible light region, *as will be discussed in Section 1.3*.

Table 1.1. Oxide photocatalysts based on *d*^{0} metal ions for water splitting under UV irradiation.

						Activity/μmol h^{-1}			
Photocatalyst	Crystal structure	BG/eV	Co-catalyst	Light source[a]	Reactant solution	H_2	O_2	QY (%)	Ref. (Year)
Ti photocatalysts									
TiO_2	Anatase	3.2	Rh	Hg–Q	Water vapor	449		29	43 (1985)
TiO_2	Anatase	3.2	NiO_x	Hg–P	3 M NaOH	6	2		54 (1987)
TiO_2	Anatase	3.2	Pt	Hg–Q	2.2 M Na_2CO_3	568	287		55 (1997)
TiO_2	Anatase	3.2	Pt	Hg–Q	Pure water	106	53		56 (1995)
B/Ti oxide	Anatase	3.2	Pt	Hg–Q	Pure water	22	11		57 (1998)
$CaTiO_3$	Perovskite	3.5	NiO_x	Hg–Q	0.2 M NaOH	30	17		58 (2002)
$SrTiO_3$	Perovskite	3.2	NiO_x	Hg–P	5 M NaOH	40	19		46, 59–63 (1980)
$SrTiO_3$	Perovskite	3.2	Rh	Hg–Xe–P	Pure water	27	14		42, 43, 64 (1980)
$Sr_3Ti_2O_7$	Layered perovskite	3.2	NiO_x	Hg–Q	Pure water	144	72		65 (2006)
$Sr_4Ti_3O_{10}$	Layered perovskite	3.2	NiO_x	Hg–Q	Pure water	170		4.5 (at 360 nm)	66 (2002)
$K_2La_2Ti_3O_{10}$	Layered perovskite	3.4–3.5	NiO_x	Hg–Q	0.1 M KOH	2186	1131		67, 68 (1997)
$Rb_2La_2Ti_3O_{10}$	Layered perovskite	3.4–3.5	NiO_x	Hg–Q	0.1 M RbOH	869	430	5 (at 330 nm)	67 (1997)
$Cs_2La_2Ti_3O_{10}$	Layered perovskite	3.4–3.5	NiO_x	Hg–Q	Pure water	700	340		67 (1997)
$CsLa_2Ti_2NbO_{10}$	Layered perovskite	3.4–3.5	NiO_x	Hg–Q	Pure water	115	50		67 (1997)
La_2TiO_5	Layered perovskite		NiO_x	Hg–Q	Pure water	442			69 (2005)
$La_2Ti_3O_9$	Layered perovskite		NiO_x	Hg–Q	Pure water	386			69 (2005)
$La_2Ti_2O_7$	Layered perovskite	3.8	NiO_x	Hg–Q	Pure water	441		12 (<360 nm)	69–78 (1999)
$La_2Ti_2O_7$:Ba	Layered perovskite		NiO_x	Hg–Q	Pure water	5000		50	69 (2005)
$KaLaZr_{0.3}Ti_{0.7}O_4$	Layered perovskite	3.91	NiO_x	Hg–Q	Pure water	230	116	12.5	79 (2003)
$La_4CaTi_5O_{17}$	Layered perovskite	3.8	NiO_x	Hg–Q	Pure water	499		20 (<320 nm)	70 (1999)
$KTiNbO_5$	Layered structure	3.6	NiO_x	Hg–Q	Pure water	30	10		80 (1999)
$Na_2Ti_6O_{13}$	Tunnel structure		RuO_2	Xe–Q	Pure water	7.3	3.5		81–84 (1990)
$BaTi_4O_9$	Tunnel structure		RuO_2	Xe–Q	Pure water	33	16		84–90 (1992)
$Gd_2Ti_2O_7$	Cubic pyrochlore	3.5	NiO_x	Hg–Q	Pure water	400	198		76 (2006)
$Y_2Ti_2O_7$	Cubic pyrochlore	3.5	NiO_x	Hg–Q	Pure water	850	420	6 (at 313 nm)	76, 91, 92 (2004)
ZrO_2		5.0	None	Hg–Q	Pure water	72	36		93–97 (1993)
Nb photocatalysts									
$K_4Nb_6O_{17}$	Layered structure	3.4	NiO_x	Hg–Q	Pure water	1837	850	5 (at 330 nm)	45, 98–108 (1986)
$Rb_4Nb_6O_{17}$	Layered structure	3.4	NiO_x	Hg–Q	Pure water	936	451	10 (at 330 nm)	105 (1997)
$Ca_2Nb_2O_7$	Layered perovskite	4.3	NiO_x	Hg–Q	Pure water	101		7 (<288 nm)	70 (1999)
$Sr_2Nb_2O_7$	Layered perovskite	4.0	NiO_x	Hg–Q	Pure water	217	97		70, 109–111 (1999)
$Ba_5Nb_4O_{15}$	Layered perovskite	3.85	NiO_x	Hg–Q	Pure water	2366	1139	7 (at 270 nm)	112 (2006)
$NaCa_2Nb_3O_{10}$	Layered perovskite		RuO_2	Hg–Q	Pure water	118	56		113 (2005)
$ZnNb_2O_6$	Columbite	4.0	NiO_x	Hg–Q	Pure water	54	21		114 (1999)
$Cs_2Nb_4O_{11}$	Pyrochlore like	3.7	NiO_x	Hg–Q	Pure water	1700	800	3 (at 270 nm)	115 (2005)
La_3NbO_7	Cubic fluorite	3.9	NiO_x	Hg–Q	Pure water	35	17		76, 116 (2004)
Ta photocatalysts									
Ta_2O_5		4.0	NiO_x	Hg–Q	Pure water	1154	529		94, 105, 117, 118 (1994)
$K_2PrTa_5O_{15}$	Tungsten bronze	3.8	NiO	Hg–Q	Pure water	1550	830		12, 119 (2000)
$K_3Ta_3Si_2O_{13}$	Tungsten bronze	4.1	NiO	Hg–Q	Pure water	390	200		120 (1997)
$K_3Ta_3B_2O_{12}$	Tungsten bronze	4.0	None	Hg–Q	Pure water	2390	1210	6.5 (at 254 nm)	121 (2006)
$LiTaO_3$	Ilumenite	4.7	None	Hg–Q	Pure water	430	220		117, 122 (1998)
$NaTaO_3$	Perovskite	4.0	NiO	Hg–Q	Pure water	2180	1100	20 (at 270 nm)	117, 122–124 (1998)
$KTaO_3$	Perovskite	3.6	Ni	Hg–Q	Pure water	6	2		105, 117, 122 (1996)

Table 1.1. Oxide photocatalysts based on d^0 metal ions for water splitting under UV irradiation. (*Cont.*)

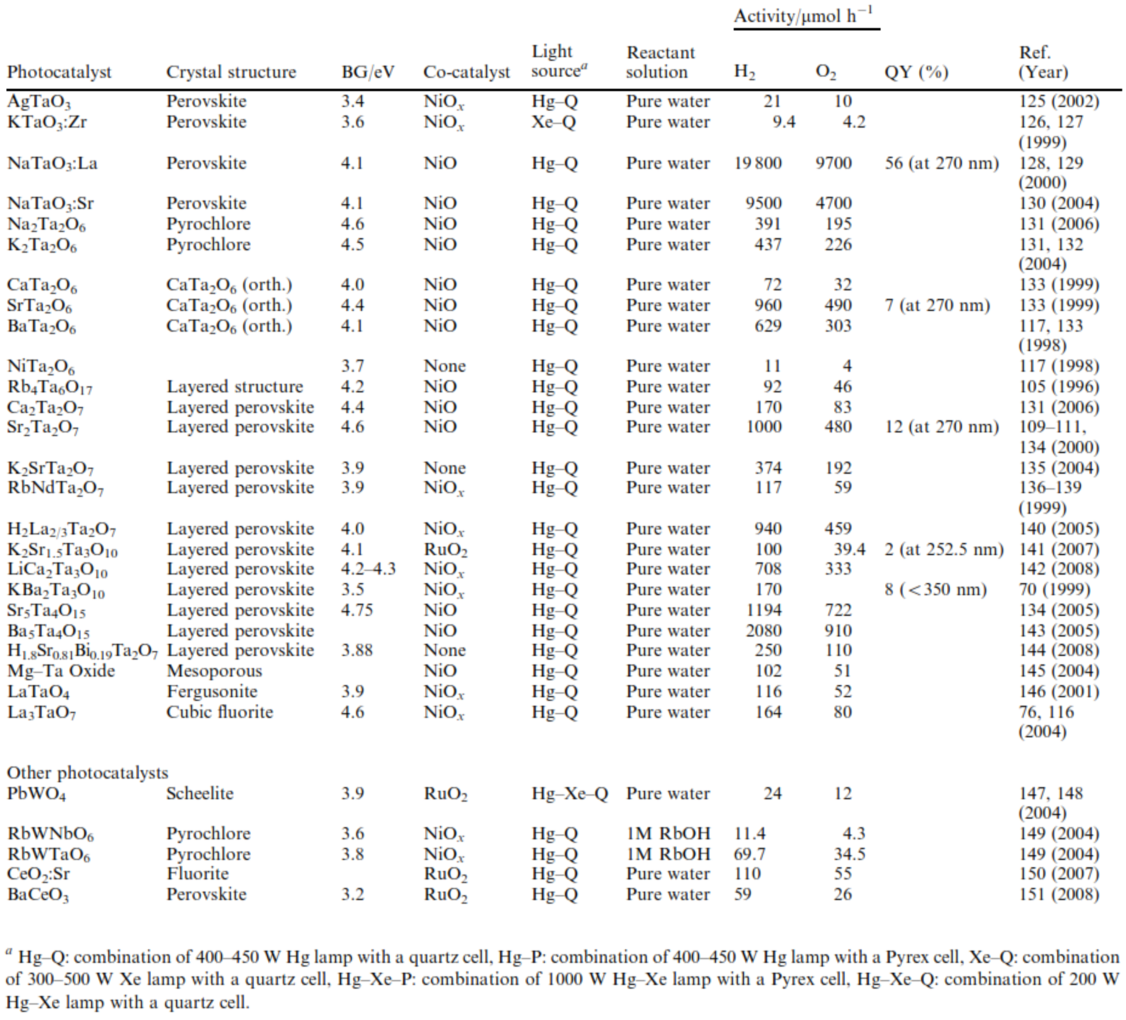

Photocatalyst	Crystal structure	BG/eV	Co-catalyst	Light source[a]	Reactant solution	Activity/μmol h^{-1} H$_2$	Activity/μmol h^{-1} O$_2$	QY (%)	Ref. (Year)
$AgTaO_3$	Perovskite	3.4	NiO_x	Hg–Q	Pure water	21	10		125 (2002)
$KTaO_3$:Zr	Perovskite	3.6	NiO_x	Xe–Q	Pure water	9.4	4.2		126, 127 (1999)
$NaTaO_3$:La	Perovskite	4.1	NiO	Hg–Q	Pure water	19 800	9700	56 (at 270 nm)	128, 129 (2000)
$NaTaO_3$:Sr	Perovskite	4.1	NiO	Hg–Q	Pure water	9500	4700		130 (2004)
$Na_2Ta_2O_6$	Pyrochlore	4.6	NiO	Hg–Q	Pure water	391	195		131 (2006)
$K_2Ta_2O_6$	Pyrochlore	4.5	NiO	Hg–Q	Pure water	437	226		131, 132 (2004)
$CaTa_2O_6$	$CaTa_2O_6$ (orth.)	4.0	NiO	Hg–Q	Pure water	72	32		133 (1999)
$SrTa_2O_6$	$CaTa_2O_6$ (orth.)	4.4	NiO	Hg–Q	Pure water	960	490	7 (at 270 nm)	133 (1999)
$BaTa_2O_6$	$CaTa_2O_6$ (orth.)	4.1	NiO	Hg–Q	Pure water	629	303		117, 133 (1998)
$NiTa_2O_6$		3.7	None	Hg–Q	Pure water	11	4		117 (1998)
$Rb_4Ta_6O_{17}$	Layered structure	4.2	NiO	Hg–Q	Pure water	92	46		105 (1996)
$Ca_2Ta_2O_7$	Layered perovskite	4.4	NiO	Hg–Q	Pure water	170	83		131 (2006)
$Sr_2Ta_2O_7$	Layered perovskite	4.6	NiO	Hg–Q	Pure water	1000	480	12 (at 270 nm)	109–111, 134 (2000)
$K_2SrTa_2O_7$	Layered perovskite	3.9	None	Hg–Q	Pure water	374	192		135 (2004)
$RbNdTa_2O_7$	Layered perovskite	3.9	NiO_x	Hg–Q	Pure water	117	59		136–139 (1999)
$H_2La_{2/3}Ta_2O_7$	Layered perovskite	4.0	NiO_x	Hg–Q	Pure water	940	459		140 (2005)
$K_2Sr_{1.5}Ta_3O_{10}$	Layered perovskite	4.1	RuO_2	Hg–Q	Pure water	100	39.4	2 (at 252.5 nm)	141 (2007)
$LiCa_2Ta_3O_{10}$	Layered perovskite	4.2–4.3	NiO_x	Hg–Q	Pure water	708	333		142 (2008)
$KBa_2Ta_3O_{10}$	Layered perovskite	3.5	NiO_x	Hg–Q	Pure water	170		8 (<350 nm)	70 (1999)
$Sr_5Ta_4O_{15}$	Layered perovskite	4.75	NiO	Hg–Q	Pure water	1194	722		134 (2005)
$Ba_5Ta_4O_{15}$	Layered perovskite		NiO	Hg–Q	Pure water	2080	910		143 (2005)
$H_{1.8}Sr_{0.81}Bi_{0.19}Ta_2O_7$	Layered perovskite	3.88	None	Hg–Q	Pure water	250	110		144 (2008)
Mg–Ta Oxide	Mesoporous		NiO	Hg–Q	Pure water	102	51		145 (2004)
$LaTaO_4$	Fergusonite	3.9	NiO_x	Hg–Q	Pure water	116	52		146 (2001)
La_3TaO_7	Cubic fluorite	4.6	NiO_x	Hg–Q	Pure water	164	80		76, 116 (2004)
Other photocatalysts									
$PbWO_4$	Scheelite	3.9	RuO_2	Hg–Xe–Q	Pure water	24	12		147, 148 (2004)
$RbWNbO_6$	Pyrochlore	3.6	NiO_x	Hg–Q	1M RbOH	11.4	4.3		149 (2004)
$RbWTaO_6$	Pyrochlore	3.8	NiO_x	Hg–Q	1M RbOH	69.7	34.5		149 (2004)
CeO_2:Sr	Fluorite		RuO_2	Hg–Q	Pure water	110	55		150 (2007)
$BaCeO_3$	Perovskite	3.2	RuO_2	Hg–Q	Pure water	59	26		151 (2008)

[a] Hg–Q: combination of 400–450 W Hg lamp with a quartz cell, Hg–P: combination of 400–450 W Hg lamp with a Pyrex cell, Xe–Q: combination of 300–500 W Xe lamp with a quartz cell, Hg–Xe–P: combination of 1000 W Hg–Xe lamp with a Pyrex cell, Hg–Xe–Q: combination of 200 W Hg–Xe lamp with a quartz cell.

Reprinted with permission from Royal Society of Chemistry: Chemistry Society Reviews [2], copyright 2009

The ideal photocatalyst should (1) be stable in water, (2) be inexpensive, (3) maximize the use of visible sun light, (4) have an appropriate band structure for water splitting redox reactions, and (5) have excellent capacitance for preventing electron-hole pair recombination. Figure 1.1(a) shows the main processes for water splitting redox reaction.

The first step is photon absorption to generate electrons and holes. In semiconductors, the valence band and conduction band are separated by an energy gap (E_g), where no allowed energy states for electron exist. In order to cause the reaction, the energy of the incident light must be larger than the band gap. The electrons and holes are generated in the conduction band and valence band, respectively. Then, these electrons and holes will cause the redox reactions as in the case of electrolysis. In photocatalysis semiconductors, the levels of the conduction bands need to be more negative than the redox potential of H^+/H_2 (0 V *vs.* NHE), and the valence band has to be more positive than the redox potential of O_2/H_2O (1.23 V). Theoretically, thus, the minimum band gap for water splitting redox reaction is 1.23 eV, corresponding to the wavelength around 1100 nm.

$$\text{Band gap (eV)} = 1240 / \lambda \text{ (nm)}$$

In order to design a visible light active photocatalyst, the band gap should be narrower than 3.0 eV ($\lambda > 415$ nm) and have sufficient band structure to cause a water splitting redox reaction.

The second step is charge separation and migration of photogenerated carriers. In this process, the crystal structure, crystallinity and defects have large influence on the reaction. Generally, the higher the crystallinity is, the smaller the amount of defects is. Defects will promote the recombination between photogenerated electrons and holes and generate heat or light instead of causing a redox reaction, as shown in Figure 1.1(b). Therefore, the recombination effect suppresses the photocatalytic activity. To achieve high efficiency of photocatalytic activity, less amount of defects or high crystallinity is required for decreasing the recombination probability.

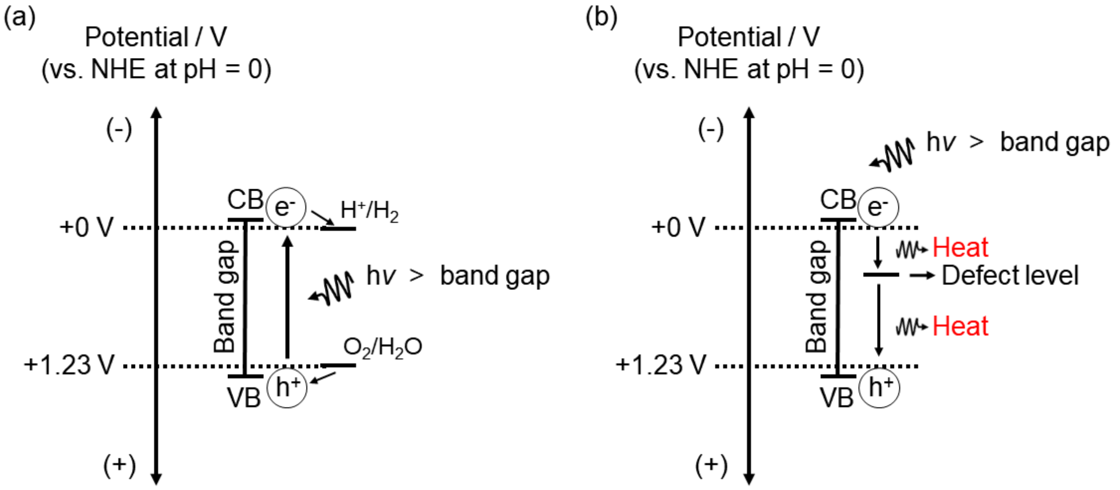

Figure 1.1. Main process in photocatalytic water splitting in semiconductors and relationship between band structure of semiconductor and redox potential of water splitting (a), and recombination of photogenerated electrons and holes by defects (b).

The last step is the surface reaction for H_2 and O_2 evolution. Important points in this step are active sites and surface area to cause the redox reaction. Even though electrons and holes are photogenerated, they will recombine with each other if there are no active sites to cause the redox reaction at the surface. Many researchers usually load co-catalysts such as Pt, NiO and RuO_2 to introduce the active sides for H_2 evolution, *which are not mentioned in this thesis*.

Among photocatalytic materials, TiO_2 and other oxide materials are most effective and widely used in industry at present. This is because they have good band structure with relatively low energy levels of conduction band edges [3]. Meanwhile, most of the transition metal oxides have relatively large band gaps in the range between 3.2 eV and 4.7 eV which is larger than the maximum band gap energy for which absorption of visible light is possible (3.0 eV). Because of this, smaller band gap materials with suitable band edge positions are beneficial for visible light active photocatalysis.

A method to decrease the optical band gaps of semiconductors is to modify or substitute the transition metal with another element as shown in Figure 1.2. This is because the conduction band has a strongly localized character of *d*-electrons, *as will be discussed in detail in Section 1.2*.

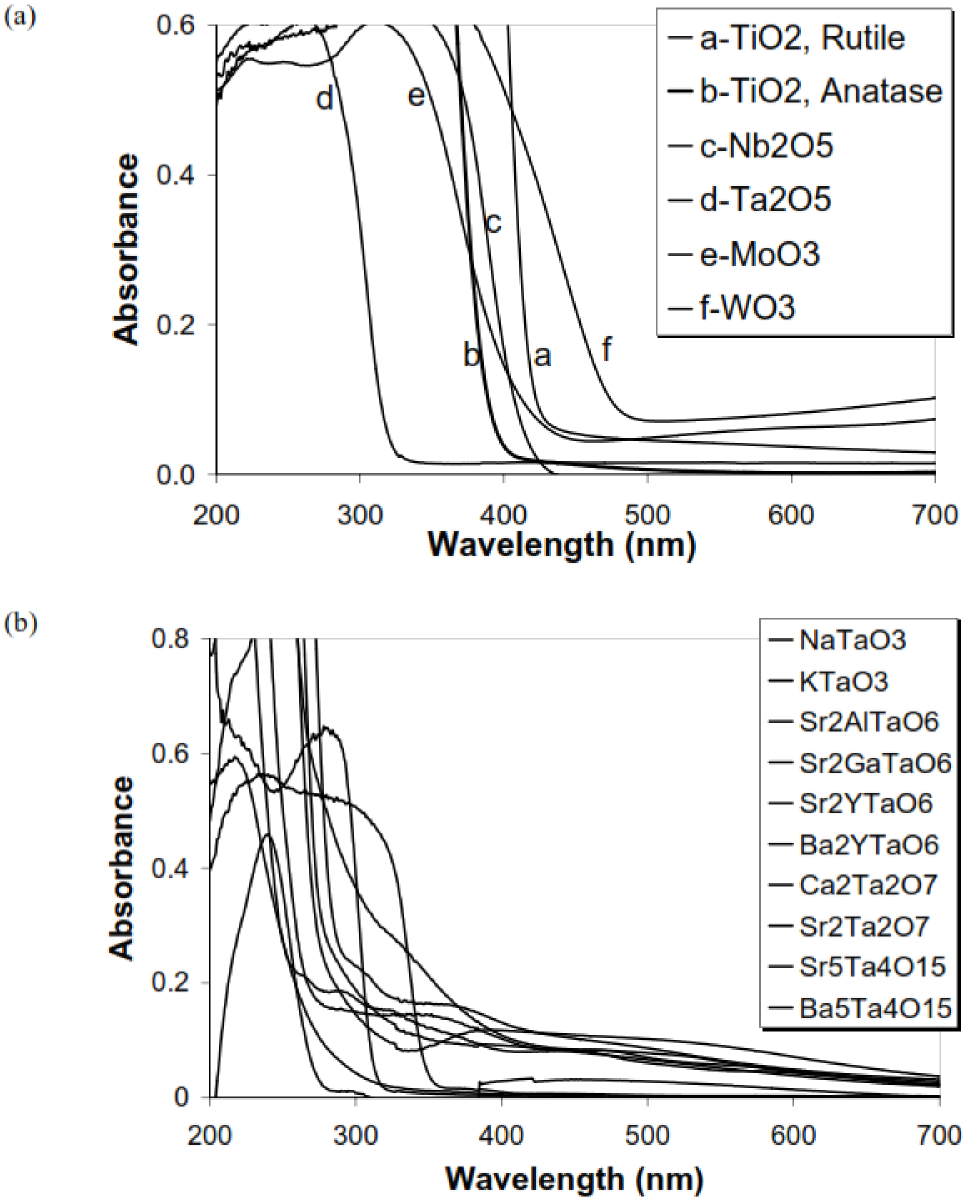

Figure 1.2. (a) Diffuse reflectance spectra of binary d^0 transition metal oxides. (b) Diffuse reflectance spectra of oxides containing Ta^{5+} in octahedral coordination. Reprinted with permission from Elsevier: Journal of Solid State Chemistry [4], copyright 2003

Another way to modify the band gap is to tune the position of valence band by anion substitution. For example, $Ca_{(1-x)}La_xTaO_{(2-x)}N_{(1+x)}$ was reported to change its colored in a designed manner, from yellow to deep red, with the variation of x between 0 and 1 [5]. Moreover, a study on band gap engineering of $KTaO_3$ by anion (nitrogen, fluorine and other halides) substitution [6] reported that the nitrogen substitution had the largest effect on the elevation of valence band. Detailed explanation about oxynitrides (nitrogen substitution) is given in Section 1.3.

1.2 Cation-induced band gap in metal oxides

In a binary metal oxides system, the optical band gap is related to the enthalpy of formation [7-8, 11]: metal oxides are formed by the reaction of molecular oxygen (O_2) and solid metals [9]. From Hess's law and Born Haber cycle theories, the total standard enthalpy of formation (ΔH°_f) consists of enthalpy of vaporization of solid metal, dissociation of oxygen gas, ionization of metal in gas phase ($\Delta H_{I.E.}$), and release of electron affinity ($\Delta H_{E.A.}$). The crystals are formed by separating the O (2p) nature lower-energy valence band and the metal nature the upper-energy conduction band by a band gap (E_g).

Figure 1.3 shows the relationship between band gap and enthalpy of formation for metal oxides. The correlation of E_g, $E_{\Delta H^\circ}$ and ΔH°_f is expressed by the following equations:

$$E_{\Delta H^\circ} = -2 \text{ x } \Delta H^\circ_f \text{ x } 2.512 \text{ x } 10^{19} / (N \text{ x } n_e)$$

$$E_g = A \exp(0.34 \text{ x } E_{\Delta H^\circ})$$

where $E_{\Delta H^\circ}$, N, n_e and A are the enthalpy, the Avogadro number, the number of electrons involved in the formation reaction, and the pre-exponential term depending on cation, respectively.

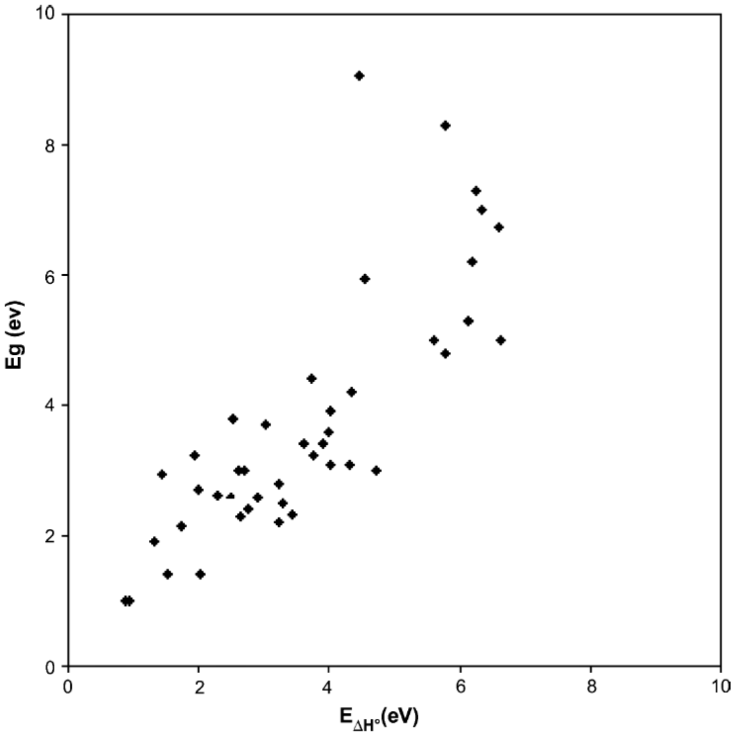

Figure 1.3. Relationship between optical band gaps and $E_{\Delta H^{\circ}}$ for different oxides. Reprinted with permission from Elsevier: Progress in Solid State Chemistry [10], copyright 2004

Table 1.2 shows the literature data on the standard enthalpy of formation and the optical band gap values of metal oxides. For d^0 binary transition metal oxides, the optical band gaps are ZrO_2 (5 eV) > Ta_2O_5 (4.2 eV) > Nb_2O_5 (3.4 eV) > TiO_2 rut. (3 eV) > WO_3 (2.7 eV). The relationship between the enthalpy of formation of ionic compounds and Pauling electronegativity is given by the following equation:

$$\Delta H^{\circ}_{f} = - N_R E_1 (X_M - X_O)^2 \text{ (eV/mol MO)}$$

where X_M and X_O are the Pauling electronegativity of metal element and oxygen, N_R is the number of resonating bonds per atom pair, and E_1 is the extraionic energy unit orbitally dependent [11-14].

The optical band gap in a binary system can be predicted by metal electronegativity. In d^0 transition metals, the Pauling electronegativity is summarized as; Zr^{4+} (1.4) > Ta^{5+} (1.5) > Nb^{5+} (1.6) ~ Ti^{4+} (1.6) > W^{6+} (1.7), which is consistent with the optical band gaps. Comparison of energy band diagram with the redox potential for water splitting (Figure 1.4) revealed that Ta_2O_5,

Nb_2O_5, TiO_2 and WO_3 have most positive positions in the conduction band, resulting in lower band gaps. However, the position of the conduction band of WO_3 is unsuitable to the redox reaction. As a result, Ta_2O_5, Nb_2O_5 and TiO_2 are predicted as high photocatalytic activity materials under ultraviolet light. In the next section, I will discuss the effect of nitrogen substitution on the photocatalytic activity in the visible light region.

Table 1.2. Thermodynamic data and energy-band gaps for some binary oxides.

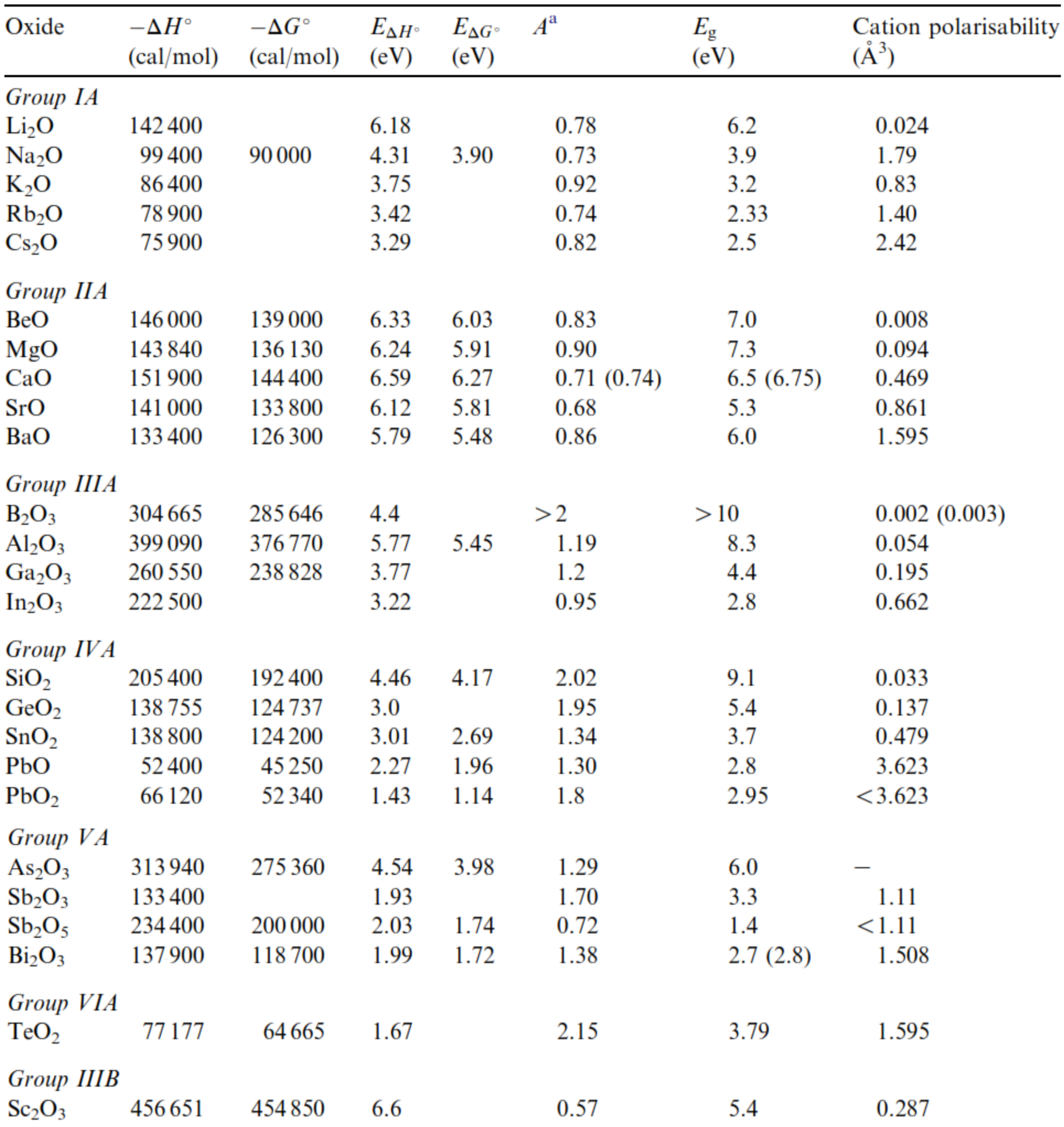

Oxide	$-\Delta H^\circ$ (cal/mol)	$-\Delta G^\circ$ (cal/mol)	$E_{\Delta H^\circ}$ (eV)	$E_{\Delta G^\circ}$ (eV)	A^a	E_g (eV)	Cation polarisability (Å^3)
Group IA							
Li_2O	142 400		6.18		0.78	6.2	0.024
Na_2O	99 400	90 000	4.31	3.90	0.73	3.9	1.79
K_2O	86 400		3.75		0.92	3.2	0.83
Rb_2O	78 900		3.42		0.74	2.33	1.40
Cs_2O	75 900		3.29		0.82	2.5	2.42
Group IIA							
BeO	146 000	139 000	6.33	6.03	0.83	7.0	0.008
MgO	143 840	136 130	6.24	5.91	0.90	7.3	0.094
CaO	151 900	144 400	6.59	6.27	0.71 (0.74)	6.5 (6.75)	0.469
SrO	141 000	133 800	6.12	5.81	0.68	5.3	0.861
BaO	133 400	126 300	5.79	5.48	0.86	6.0	1.595
Group IIIA							
B_2O_3	304 665	285 646	4.4		>2	>10	0.002 (0.003)
Al_2O_3	399 090	376 770	5.77	5.45	1.19	8.3	0.054
Ga_2O_3	260 550	238 828	3.77		1.2	4.4	0.195
In_2O_3	222 500		3.22		0.95	2.8	0.662
Group IVA							
SiO_2	205 400	192 400	4.46	4.17	2.02	9.1	0.033
GeO_2	138 755	124 737	3.0		1.95	5.4	0.137
SnO_2	138 800	124 200	3.01	2.69	1.34	3.7	0.479
PbO	52 400	45 250	2.27	1.96	1.30	2.8	3.623
PbO_2	66 120	52 340	1.43	1.14	1.8	2.95	<3.623
Group VA							
As_2O_3	313 940	275 360	4.54	3.98	1.29	6.0	–
Sb_2O_3	133 400		1.93		1.70	3.3	1.11
Sb_2O_5	234 400	200 000	2.03	1.74	0.72	1.4	<1.11
Bi_2O_3	137 900	118 700	1.99	1.72	1.38	2.7 (2.8)	1.508
Group VIA							
TeO_2	77 177	64 665	1.67		2.15	3.79	1.595
Group IIIB							
Sc_2O_3	456 651	454 850	6.6		0.57	5.4	0.287

Table 1.2. Thermodynamic data and energy-band gaps for some binary oxides. (*Cont.*)

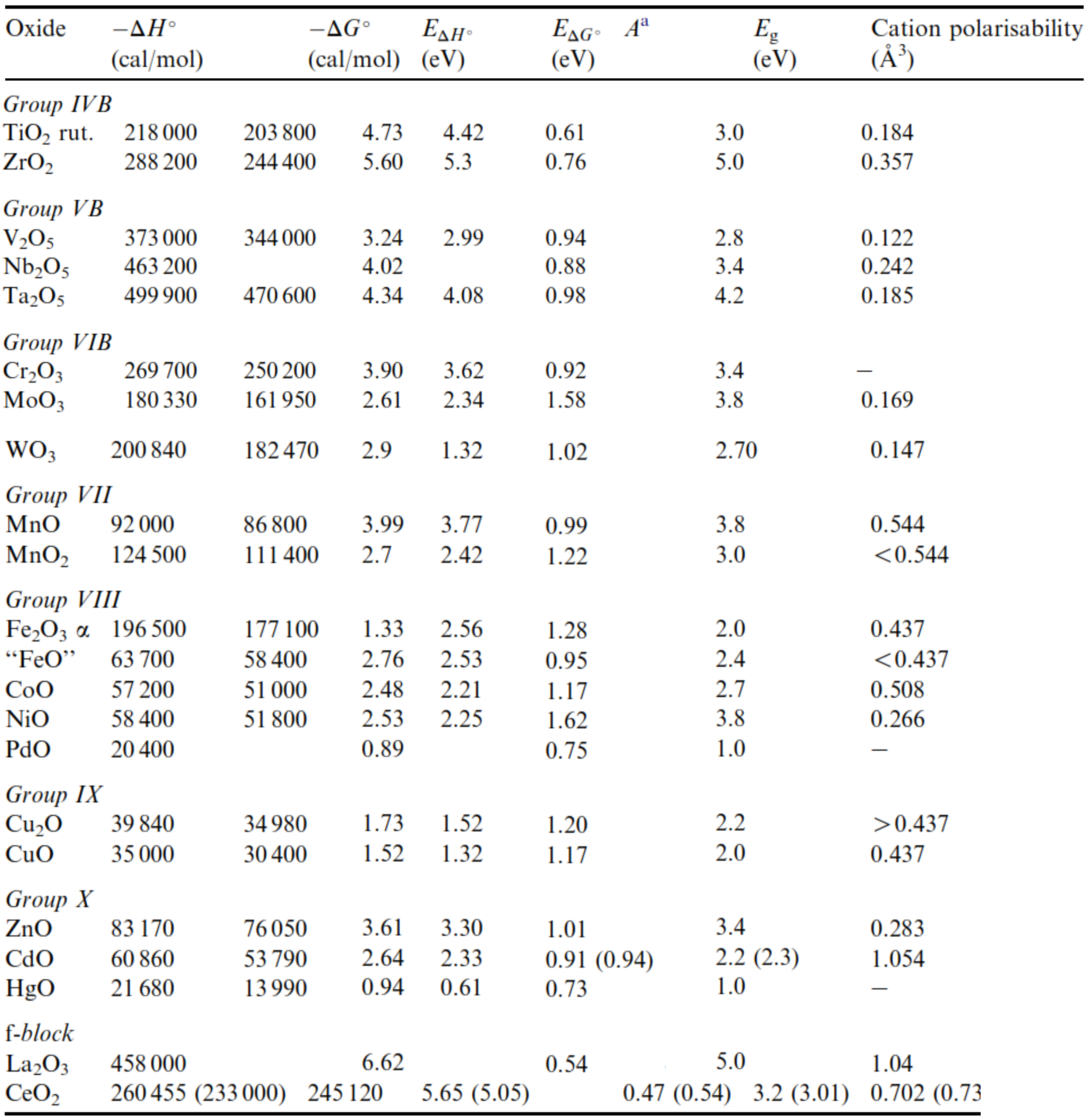

Oxide	$-\Delta H^\circ$ (cal/mol)	$-\Delta G^\circ$ (cal/mol)	$E_{\Delta H^\circ}$ (eV)	$E_{\Delta G^\circ}$ (eV)	A^a	E_g (eV)	Cation polarisability (Å^3)
Group IVB							
TiO_2 rut.	218 000	203 800	4.73	4.42	0.61	3.0	0.184
ZrO_2	288 200	244 400	5.60	5.3	0.76	5.0	0.357
Group VB							
V_2O_5	373 000	344 000	3.24	2.99	0.94	2.8	0.122
Nb_2O_5	463 200		4.02		0.88	3.4	0.242
Ta_2O_5	499 900	470 600	4.34	4.08	0.98	4.2	0.185
Group VIB							
Cr_2O_3	269 700	250 200	3.90	3.62	0.92	3.4	–
MoO_3	180 330	161 950	2.61	2.34	1.58	3.8	0.169
WO_3	200 840	182 470	2.9	1.32	1.02	2.70	0.147
Group VII							
MnO	92 000	86 800	3.99	3.77	0.99	3.8	0.544
MnO_2	124 500	111 400	2.7	2.42	1.22	3.0	<0.544
Group VIII							
Fe_2O_3 α	196 500	177 100	1.33	2.56	1.28	2.0	0.437
“FeO”	63 700	58 400	2.76	2.53	0.95	2.4	<0.437
CoO	57 200	51 000	2.48	2.21	1.17	2.7	0.508
NiO	58 400	51 800	2.53	2.25	1.62	3.8	0.266
PdO	20 400		0.89		0.75	1.0	–
Group IX							
Cu_2O	39 840	34 980	1.73	1.52	1.20	2.2	>0.437
CuO	35 000	30 400	1.52	1.32	1.17	2.0	0.437
Group X							
ZnO	83 170	76 050	3.61	3.30	1.01	3.4	0.283
CdO	60 860	53 790	2.64	2.33	0.91 (0.94)	2.2 (2.3)	1.054
HgO	21 680	13 990	0.94	0.61	0.73	1.0	–
f-*block*							
La_2O_3	458 000		6.62		0.54	5.0	1.04
CeO_2	260 455 (233 000)	245 120	5.65 (5.05)		0.47 (0.54)	3.2 (3.01)	0.702 (0.73

Reprinted with permission from Elsevier: Progress in Solid State Chemistry [10], copyright 2004

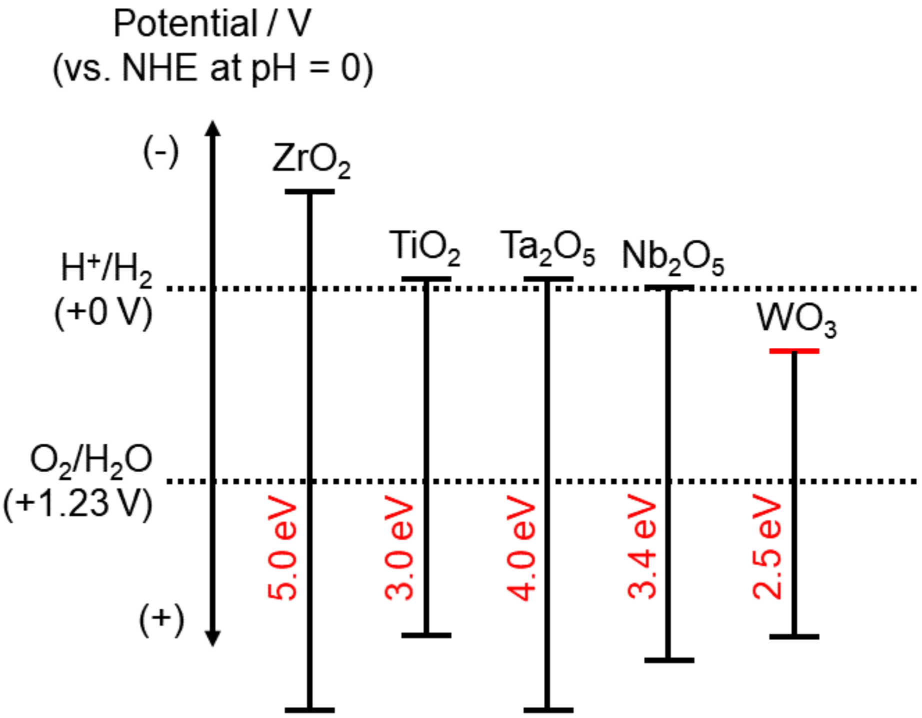

Figure 1.4. Position of the conduction and valence bands and band gap values for *d*^{0} transition metal oxides. Adapted from [2, 15-16].

1.3 Anion substitution-induced band gap in metal oxides

Many oxide photocatalysts have been developed since 1980s. However, most of them have wide band gaps which require ultraviolet light to generate electrons and holes, although the solar spectrum has large weights in the visible and infrared regions. These wide band gap oxides are not suitable for the purpose of efficient use of the solar energy. As mention in the previous section, the main cations for water splitting photocatalyst are *d*^{0} transition metals, and the *d* orbitals of these cations contribute to the lowest part of the conduction band while the upper part of the valence band is mainly constructed by O 2p orbitals. Mostly, the position of the valence band of oxides is located at ~3 eV (versus normal hydrogen electrode), which is significantly positive compared with the O_2/H_2O redox potential.

Referring from previous reports, one may notice that many researches have focused on narrowing of band gaps through positive shift of conduction band. With this cation substitution, optical band gap can be successfully reduced [2, 17-20].

Another approach is the substitution of oxygen with different anionic components for introducing a new filled energy state in more negative electrode potential side than O 2p state, which is expected to reduce the band gap by negatively shift of the valence band as shown in Figure 1.5. Many recent reports claim that metal nitride/oxynitride photocatalysts have suitable band gaps for visible-light active water splitting without photodissociation [21-25]. Nitrogen is appropriate for replacing oxygen because both of them have close electronic configurations and ionic radii [30]. In an oxynitride system, the N 2p orbitals fill the energy states with more negative potential than O 2p orbitals, and therefore the band gap becomes narrow, resulting in enhanced photocatalytic activity in the visible light region. Because the ionic radii of N^{3-} and O^{2-} are similar, partial or full substitution of O by N is possible. Moreover, it is expected that the nitrogen substitution for oxygen has no effect on the conduction band level [23].

Most of the d^0 transition metal oxynitrides possess the absorption edges above 600 nm. For over 15 years, transition metal oxynitrides based Ti^{4+}, Ta^{5+} and Nb^{5+} have been extensively studied as visible light active photocatalysts [26-27]. Two typical transition metal oxynitrides used as photocatalysts are depicted in Figure 1.6. TaON with baddeleyite structure has a band gap of 2.4-2.5 eV, which corresponds to an absorption edge around 500 nm [28].

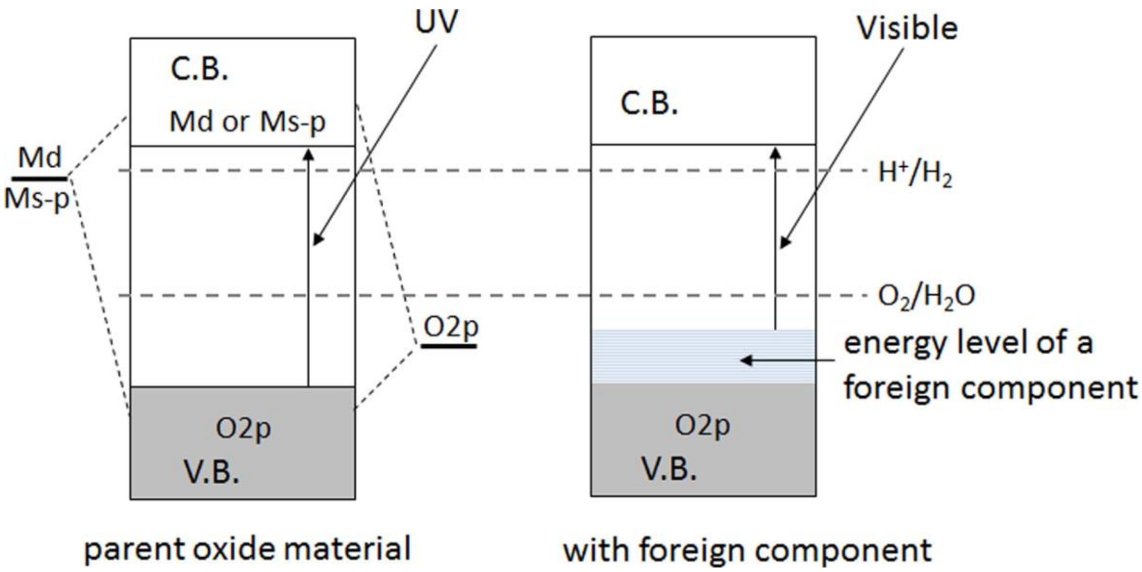

Figure 1.5. Strategy to design visible light active photocatalysts for water splitting. Reprinted with permission from Taylor & Francis Online by CC BY 3.0: Science and Technology of Advanced Materials [25], copyright 2015 (Open Access)

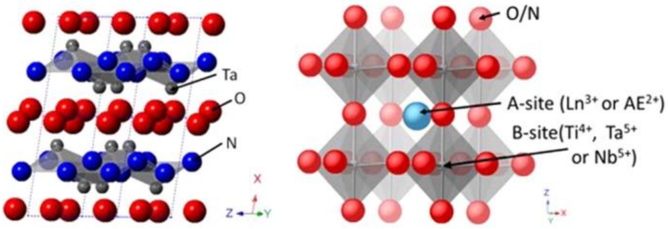

Figure 1.6. Crystal structures of TaON (left), and perovskite oxynitrides (right). Adapted and reprinted with permission from Taylor & Francis Online by CC BY 3.0: Science and Technology of Advanced Materials [25], copyright 2015 (Open Access)

Quaternary metal oxynitrides with perovskite structure ABX_3 have also been a target of intensive researches (Figure 1.6). This crystal structure is governed by Goldschmidt tolerance factor (t) [29]:

$$t = (r_A + r_X) / \sqrt{2}\ (r_B + r_X)$$

where r_A, r_B and r_X are the ionic radii of *A*-site cation, *B*-site cation and anion (nitrogen and oxygen), respectively. The ideal perovskite structure has $t = 1$.

Table 1.3. Photocatalytic activity of (oxy)nitrides of d^0 electronic configuration for H_2 and O_2 evolution under visible light ($\lambda \geq 420$ nm). Reprinted with permission from Taylor & Francis Online by CC BY 3.0: Science and Technology of Advanced Materials [25], copyright 2015 (Open Access)

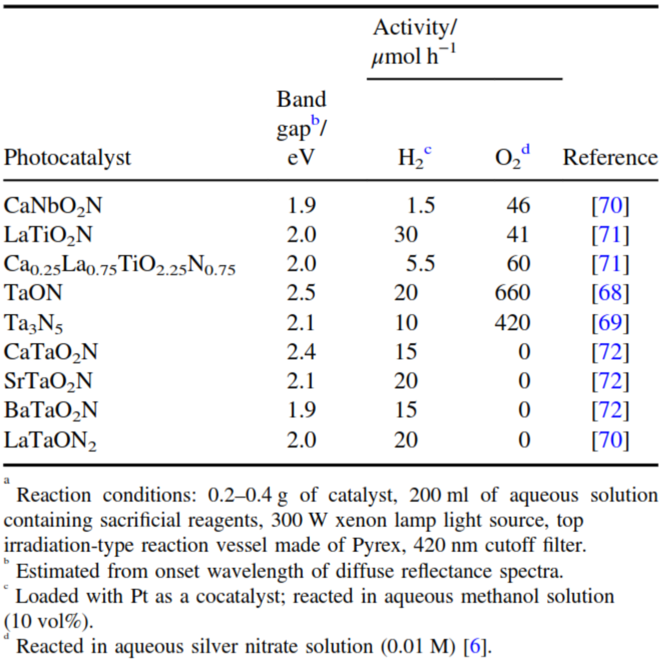

Photocatalyst	Band gap[b]/ eV	Activity/ μmol h^{-1} H_2[c]	O_2[d]	Reference
$CaNbO_2N$	1.9	1.5	46	[70]
$LaTiO_2N$	2.0	30	41	[71]
$Ca_{0.25}La_{0.75}TiO_{2.25}N_{0.75}$	2.0	5.5	60	[71]
TaON	2.5	20	660	[68]
Ta_3N_5	2.1	10	420	[69]
$CaTaO_2N$	2.4	15	0	[72]
$SrTaO_2N$	2.1	20	0	[72]
$BaTaO_2N$	1.9	15	0	[72]
$LaTaON_2$	2.0	20	0	[70]

[a] Reaction conditions: 0.2–0.4 g of catalyst, 200 ml of aqueous solution containing sacrificial reagents, 300 W xenon lamp light source, top irradiation-type reaction vessel made of Pyrex, 420 nm cutoff filter.

[b] Estimated from onset wavelength of diffuse reflectance spectra.

[c] Loaded with Pt as a cocatalyst; reacted in aqueous methanol solution (10 vol%).

[d] Reacted in aqueous silver nitrate solution (0.01 M) [6].

The *A*-site is occupied by a large cation such as Ca^{2+}, Sr^{2+} and Ba^{2+}, and the *B*-site is by a smaller cation, such as Ti^{4+}, Ta^{5+} and Nb^{5+}. The *X*-site is randomly occupied by O^{2-} and N^{3-}, where the ratio of oxygen and nitrogen is determined by the charge balance of the cation. For example, in case that A and B are divalent and pentavalent, respectively, the O/N ratio is 2 (ABO_2N).

In perovskite oxynitrides, the band gap is around 1.8-2.5 eV, which corresponds to the light absorption in wavelength around 500-700 nm (visible light region). Indeed, evolution of H_2 and O_2 gases under visible light irradiation was confirmed as shown in Table 1.3. Unfortunately, at present, it is impossible to cause the direct water splitting without using Z-scheme photocatalytic system (Figure 1.7) with 2 steps excitation (Figure 1.8). In this system with n-type semiconductor anode, O_2 gas is evolved from the semiconductor photocatalyst electrode and H_2 gas is evolved from the counter electrode. On the other hand, in p-type semiconductor, H_2 gas is evolved from the semiconductor photocatalyst electrode and O_2 gas is evolved from counter electrode [2, 29].

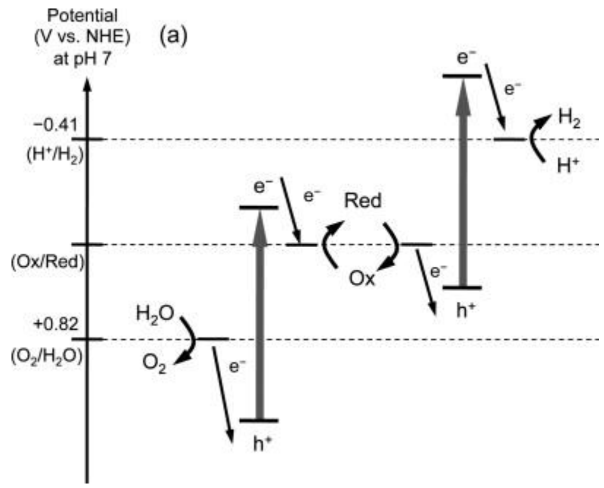

Figure 1.7. Schematic energy diagram of photocatalytic system with two-step photoexcitation system. Adapted and reprinted with permission from Elsevier: Journal of Photochemistry and photobiology C: Photochemistry Reviews [29], copyright 2010

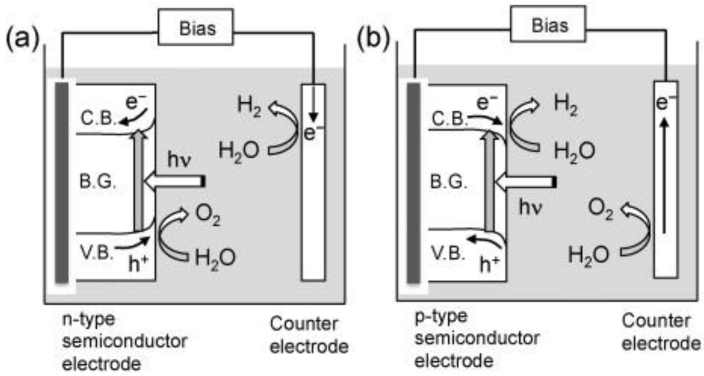

Figure 1.8. Photoelectrochemical water splitting system using n-type semiconductor (a), and p-type semiconductor (b). Adapted and reprinted with permission from Elsevier: Journal of Photochemistry and photobiology C: Photochemistry Reviews [29], copyright 2010

In conclusion, oxynitride photocatalysts is active in solar water splitting in the visible light region though the band gap value differs from a compound to another. In this dissertation, I synthesized oxynitrides in thin film form and investigated their structural, physical and photoelectric properties. In the next section, I briefly introduce conventional synthesis method of oxynitrides and point out its problems.

1.4 Synthesis methods of oxynitrides

At present, oxynitrides are synthesized in powder form with ammonolysis method [31-33] where oxide precursors obtain through the citrate route. With the heat treatment of oxide precursor with NH_3, it can obtain oxynitride with partial dispersion.

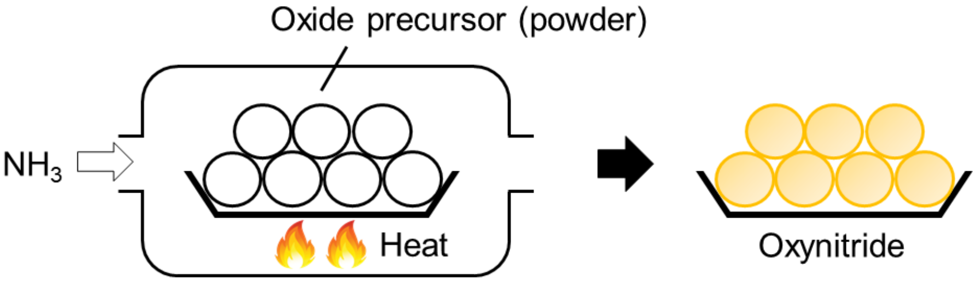

Figure 1.9. Illustration of ammonolysis method using oxide precursor.

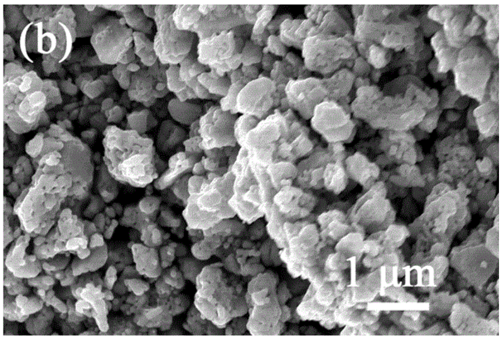

Figure 1.10. SEM image of oxynitride powder produced by ammonolysis method. Adapted and reprinted with permission from Royal Society of Chemistry: Dalton Transactions [36], copyright 2015

Figure 1.9 illustrates this synthesis method, which starts with heating an oxide precursor at temperature over 800 ˚C under ammonia gas flow. At such high temperature, ammonia gas is dissociated into hydrogen and nitrogen gases, which would drive the reaction although the detailed reaction mechanism is still unclear. The bulk powders synthesized by ammonolysis have grain boundaries (Figure 1.10) and defects [34, 35] on the surfaces, which might degrade the photocatalytic activity due to the recombination effect as discussed before.

Recently, direct synthesis methods by using epitaxial growth technique were developed to suppress the grain boundary effect. In these methods, nitrogen was supplied as nitrogen radicals [37-39] created by activating N_2 or NH_3 gases with RF sources [38, 40-41]. By using a single crystal substrate, single crystalline thin films of oxynitrides can be obtained.

1.5 Epitaxial thin film

As mention in the previous section, oxynitrides have mainly been synthesized by ammonolysis method. The specimens obtained by ammonolysis have rough surfaces with defects. In order to understand the intrinsic properties and achieve high photocatalytic activity, single crystalline samples are desired because they are relatively free from extrinsic factors such as defects and grain boundaries.

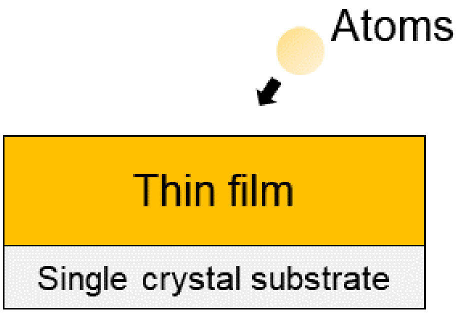

Figure 1.11. Epitaxial growth method for single crystalline thin film.

A technique to fabricate single crystalline thin films is epitaxial growth (Figure 1.11). In this technique, an epitaxial thin film is fabricated on a single crystalline substrate that is matched with the target material in both crystal structure and lattice constants. An epitaxial force from the substrate helps the nucleation process to form a suitable crystalline form. There are two types of epitaxy; one is homo-epitaxy and the other is hetero-epitaxy. Homo-epitaxy is fabrication of a film material on a substrate of the same material. In this case, the films tend to have high quality with less defects due to perfect lattice matching between film and substrate. On the other hand, hetero-epitaxy is the process that the film and substrate materials are different. In hetero-epitaxy, matching of crystal structure and lattice constants is a key to fabricate high quality films. In general, the lattice mismatch/matching (f, %) is defined as follows:

$$f = [\,(A_{\mathrm{film}} - A_{\mathrm{substrate}}) / A_{\mathrm{substrate}}\,] \times 100$$

where A_{film} and $A_{\mathrm{substrate}}$ are the lattice parameters of thin film and substrate, respectively. Usually, the lattice mismatch between film and substrate should not be greater than 2% in epitaxial growth technique. When the lattice mismatch is larger than 2%, introduction of another thin layer, often referred to as a buffer layer, between the main layer and substrate is effective. The buffer layer should have an intermediate lattice constant between main film and substrate. Epitaxial growth on lattice matched substrate or buffer layer is called coherent growth. Generally, the coherent growth is less influenced by defects and misfit transition, resulting in high crystallinity. Moreover, epitaxial growth technique can stabilize metastable phases such as anatase TaON [38] or perovskite $Sm_2Ti_2O_7$ [42]. These films are hard to stabilize in bulk form because they are needed high pressure to synthesis. Epitaxial force from substrate [43-44] or buffer layer [45] can realize such “high pressure” conditions.

1.6 Seed and buffer layers in epitaxial growth

As mentioned in the previous section, an important factor to obtain high quality thin films in hetero-epitaxy is lattice matching between film and substrate. When the lattice mismatch is large, two techniques utilizing inserted layers have been employed so far. The fundamental roles of these layer are serving a suitable nucleation condition with the same crystallographic orientation and lattice constant as the main layer and promoting the lateral growth of the film by decreasing an interfacial free energy between film and substrate [46]. The differences between seed layer and buffer layer are as follows.

Seed layer is usually referred to as a layer inserted to optimize the nucleation rate or make the growth direction in the later deposition process highly uniform. Without seed layer, the film growth rate might be low or the film might contain grains grown in an unexpected direction. As is well known, in heteroepitaxy use of a lattice matched layer can decrease the fabrication temperature [47]. Introduction of seed layer will enable to grow oxynitride films that easily release nitrogen at high temperature. For example, the growth temperature of anatase TaON was reduced by 50-100 ˚C by introducing an anatase TiO_2 seed layer [48] (Figure 1.12). This is because anatase TiO_2 has the same crystal structure as TaON, consisting of edge-shared MX_6 octahedra.

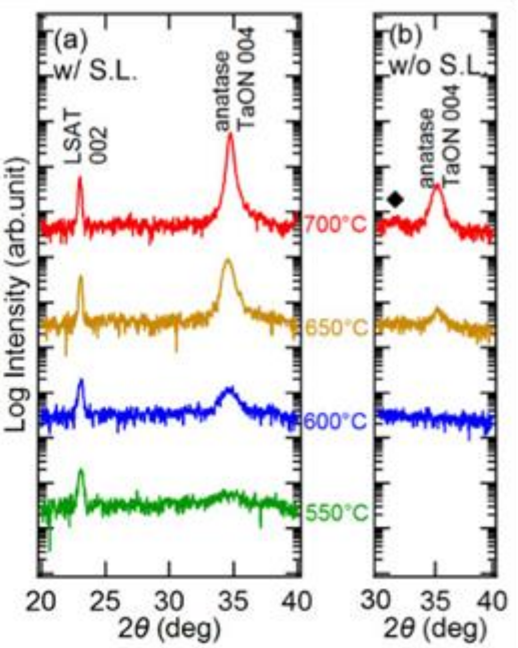

Figure 1.12. XRD patterns of TaON films grown on LSAT substrate (a) with and (b) without anatase TiO_2 seed layer. Reprinted with permission from the Japan Society of Applied Physics: Japanese Journal of Applied Physics [48], copyright 2015

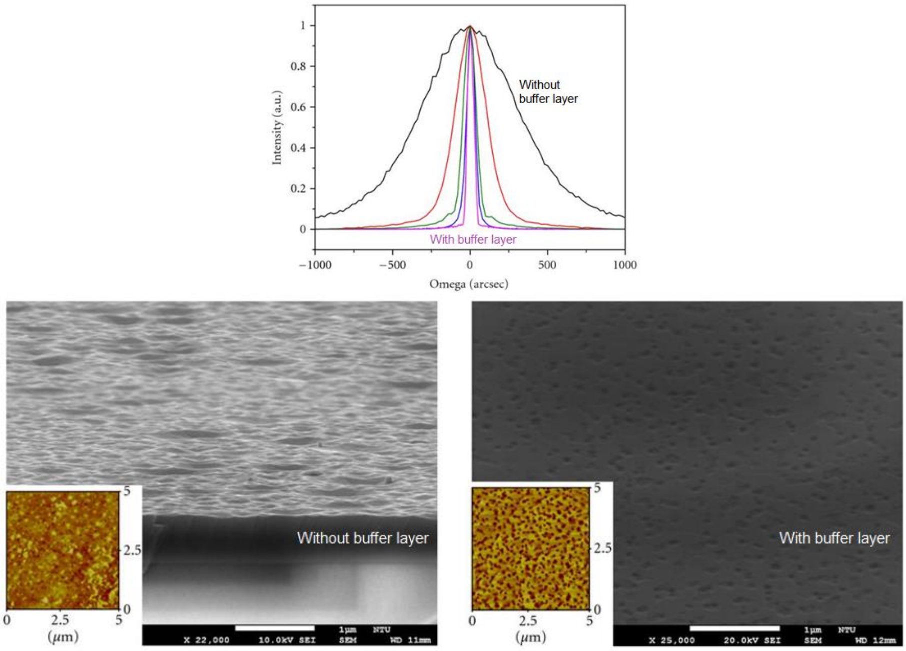

Figure 1.13. X-ray rocking curves and scanning electron microscope and atomic force microscope images of ZnO epitaxial thin films with and without MgO buffer layer. Adapted and reprinted with permission from CC BY 3.0: Journal of Nanomaterials [45], copyright 2012 (Open Access)

On the other hand, buffer layer is used when the film and substrate have large lattice mismatch. In general, buffer layer suppresses lattice mismatch, lattice stress/strain, and adhesion. Use of lattice matched buffer layer between film and substrate can enhance the crystallinity and surface flatness of the film because the buffer reduces the in-plane lattice parameter and allows for batter lattice matching, resulting to thread dislocation density. For example, it was reported that the ZnO epitaxial thin film grown on sapphire substrate with the aid of MgO buffer layer had enhanced surface flatness and improved crystallinity [45], as shown in Figure 1.13.

1.7 Purpose of this study

As mentioned above, for achieving high efficiency in photoelectrochemical solar water splitting, it is highly desired to develop oxynitride materials with narrow energy band gaps and appropriate reduction and oxidation potentials for water splitting. Suppression of the density of defects and improvement of surface flatness will assist charge separation, resulting in higher photocatalytic activity. In this study, I aimed to fabricate single crystalline epitaxial thin films with nitrogen plasma assisted pulsed laser deposition (NPA-PLD) method, where the epitaxial force from the substrate was expected to improve the surface flatness and crystallinity. I focused on oxynitride based on Ta^{5+} or Nb^{5+}, because these two metal ions have suitable H^+/H_2 redox potential and more positive potential among d^0 transition metal ions, which would lead to narrow band gaps. Moreover, nitrogen substitution for oxygen will reduce the optical band gap by adding additional levels of N 2p at the top of the valence band.

With the high quality oxynitride epitaxial thin films, I investigated their intrinsic optical and electric properties. I also examined the photocatalytic properties of Ta based oxynitride thin films, which is promising as an efficient visible light responsive photocatalyst.

Chapter 2

Experimental methods

2.1 Sample preparation: pulsed laser deposition (PLD)

In this study, I mainly used pulsed laser deposition (PLD) for fabrication of my samples. In this section, I will explain the overview of this system.

PLD is a method for synthesizing thin films from vapor phases. High energy pulsed laser is irradiated on the raw material, called target, in a high vacuum chamber. The species generated from the target form a plasma, called plume, and are deposited on a substrate inside the chamber at specific temperature and partial pleasure. The advantages of PLD can be summarized as follows.

- It is easy to control temperature and atmosphere under a specific pressure during the deposition.
- Highly uniform thin films can be obtained.
- It is possible to stabilize a metastable phase because PLD is a non-equilibrium process.
- It is possible to synthesis single crystalline films by using epitaxial growth technique.
- Multi-layer thin films can be obtained by using multiple targets.
- Many kinds of targets, such as oxides, metals and nitrides, can be used.
- It is easy to control the cation ratios by adjusting the composition of the target.

The only disadvantage of PLD is that it is hard to synthesize large area thin films because the film uniformity in the in-plane direction is restricted by the size of the plume. Therefore, PLD method has been mainly used in the field of basic researches. Different methods such as sputtering are adopted to mass production.

The overview of my PLD chamber is shown in Figure 2.1. In order to keep high vacuum in the main chamber, load lock (L/L) chamber is required for preventing air from entering to the main chamber. Introducing/taking out substrate or target into/from the PLD chamber can be done inside the L/L chamber. The L/L chamber was maintained in a high vacuum level by a turbo molecular pump. However, turbo molecular pump cannot be used under atmospheric pressure because the high density molecules cause severe damage to the fan. Accordingly, the L/L chamber was first evaluated by a rotary pump to a certain vacuum level, and, after that, the turbo molecular pump was switched on. Laser beams from an excimer laser was introduced into the main chamber through optical equipment.

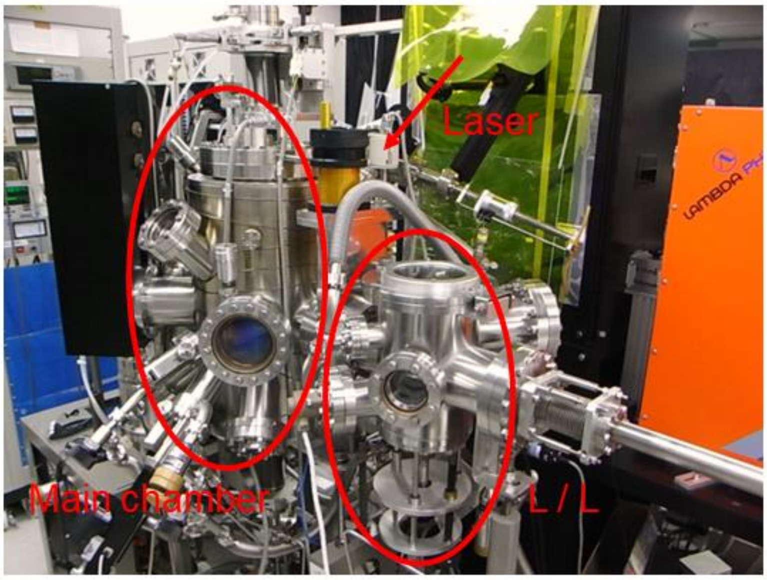

Figure 2.1. Overall picture of the pulsed laser deposition system used in this study.

PLD growth inside the main chamber is schematically illustrated in Figure 2.2. In my experiment, a substrate was put on a holder with a paste and fixed with clamps (Figure 2.3(a)). Either silver or platinum was used as the paste. The paste was not only for fixing substrate but also for improving the thermal contact between film and substrate and the uniformity of temperature at the substrate surface. Moreover, to avoid organic contamination and evaporation of the paste inside the chamber, the substrate was pre-heated at 380 ˚C for at least 30 min.

Inside the chamber, the substrate was heated by an infrared lamp from the backside of the substrate holder. The temperature of the substrate was controlled by the input current of the lamp. The temperature of the holder was evaluated using the spectrum emitted from the platinum paste measured by a pyrometer.

A target was fixed with a silver paste on the target holder (Figure 2.3(b)), and the target was also pre-heated before introducing into the chamber. In every deposition run, the target needed to be pre-ablated for about 20 min to remove oxidized layers or impurities on the target surface.

In this study, oxynitrides were fabricated by using nitrogen plasma assisted pulsed laser deposition (NPA-PLD), where nitrogen was supplied into the film by a using radio-frequency (rf) radical source [38, 49-50]. The rf source could generate nitrogen radicals by breaking the triple bond of nitrogen gas. Consequently, the radicals were irradiated onto the substrate, where high vacuum was kept around the substrate by using a differential evacuation system. An advantage of this NPA-PLD method is high composition uniformity of the films.

A KrF excimer (λ = 248 nm) laser was used as a source to generate pulsed laser beams. Excimer is a molecule in an excited state. Radiation in excimer laser originates from the decomposition of excimer. The frequency of pulsed laser can be controlled by changing the period of the laser chopper which reflects the time of atoms to migrate [51]. Moreover, by changing the condition of the attenuator, laser density can also be changed, which affects the overall laser energy.

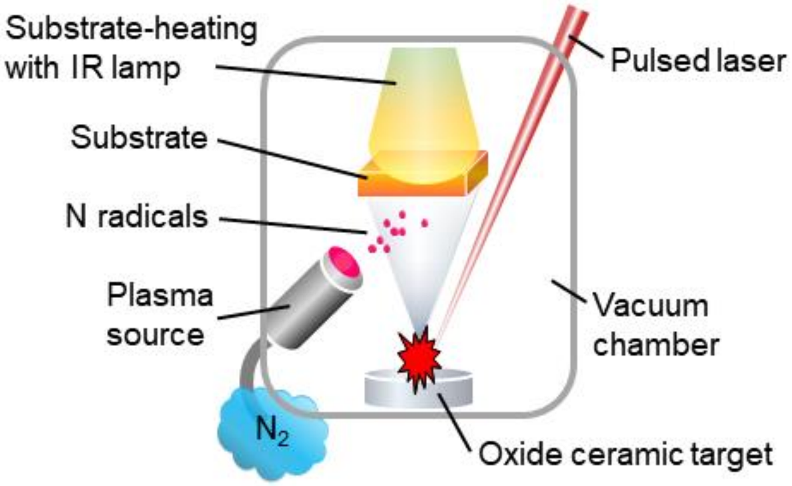

Figure 2.2. Schematic illustration of NPA-PLD method.

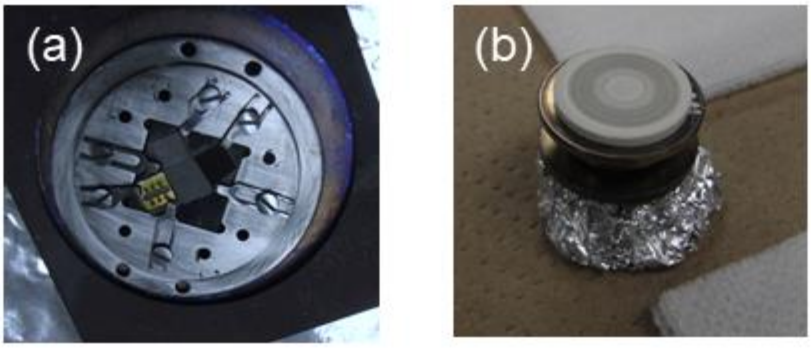

Figure 2.3. Substrates mounted on a substrate holder with and without a titanium mask (a), and a target mounted on a target holder (b).

2.2 Crystallographic characterization

2.2.1 Reflection high energy electron diffraction (RHEED) [52-54]

Reflection high energy diffraction (RHEED), which can observe crystal growth under high-vacuum condition, is a powerful tool to elucidate the film growth mechanism. RHEED informs us of the crystal structure and morphology of the outer layer without signals from the deeper layer. RHEED is based on the interaction between the charged electron beam and the electrons in the samples, similar to the case of X-ray diffraction. Since the incident angle of the electron beam is small, the penetration depth is very small, i.e., RHHED is surface-sensitive. Moreover, this technique does not disturb the film growth so that in-situ observation can be done during film fabrication.

In RHEED measurements, an electron beam is projected from an electron gun to the sample with high voltage (10-50 kV) to generate a diffraction in low incident angles. The wavelength is referred from de Broglie wave $\lambda = h / p$ where p is the momentum. Diffraction will occur when the reciprocal lattice vectors of electron beam and sample are the same. In an ideal sample which is single crystalline with a flat surface, the reciprocal lattice of atoms has a square shape. It means that the atoms align not only in the same direction of the electron beam but also in the perpendicular direction. As a result, the reciprocal lattice is a set of rods which appear as a spotty diffraction pattern on the Laue zones. On the other hand, if the samples have some small domains or rough surfaces, the observed diffraction patterns are no longer spotty but are characterized by steaks. If the surface is very rough, regular spots emerge due to the transmission of the electron beam. In case of polycrystalline samples, ring-like patterns are observed.

As I mention before, RHEED can observe how the crystal is grown during the deposition. There are three kinds of growth modes. The first one is layer-by-layer growth in which the crystal grows in a two-dimensional manner on each terrace until the perfect coverage of the surface. In this case, the RHEED intensity sinusoidally oscillates. The second mode is step-flow, and this growth mode is often observed when the growth temperature is high enough to promote the migration of atoms to the step edges in the step-and-terrace structure. The third case is island growth, in which the crystal favors growing on the top of the first layer rather than covering the original surface. In this mode, the observed RHEED pattern shows regular spots because of rough surface. On the other hand, in layer-by-layer growth mode, the surface roughness is minimized when each atomic layer is completed.

The period of the RHEED oscillation corresponds to the time required for complete growth of one atomic layer, from which the growth rate can be evaluated.

2.2.2 X-ray diffraction (XRD) [52, 55-56]

X-ray diffraction (XRD) is one of the most effective methods to characterize crystal structures. X-ray is an electromagnetic wave of which wavelength is between 1 pm and 10 nm, corresponding to the lengths of crystal lattice.

When X-ray with a wavelength (λ) is irradiated on a crystalline material, it is reflected in specific discrete directions. Giving that the crystal has parallel planes separated by the same distance (d), diffraction takes place when the Bragg's condition is satisfied:

$$2d \sin \theta = n \lambda$$

where θ is the scattering angle, which is equal to the incident angle, and n is a positive integer. Figure 2.4 shows a schematic of XRD instrument in which a sample stage is freely rotated in a three-dimensional manner. The lattice constant is calculated from Bragg's equation by the 2θ values of the experimentally observed diffraction peaks. Usually, XRD is measured in the geometry that the lattice planes are in parallel with the surface, referred to as θ-2θ measurement under the condition of $\theta = \omega$. From the diffraction pattern, i.e., from the diffraction intensity vs 2θ plot, one can determine the crystal structure as well as the lattice constants. XRD pattern also gives the information of phase purity. That is, impurity phases can be detected when tilting the sample by a suitable angle (asymmetric setting). There are three kinds of detectors: 0D, 1D, and 2D. With increasing the dimensions of detector, the resolution becomes worse due to the widened detection range. 2D detector is the easiest to determine the crystal orientation because the detector can detect the X-rays reflected from the horizontal plane. In contrast, 0D and 1D detectors are mostly used for detailed measurements in a specific plane direction.

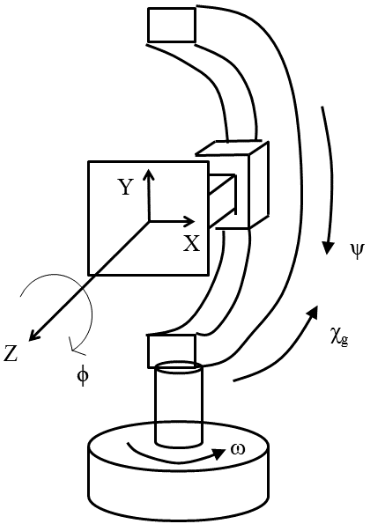

Figure 2.4. Parameters of goniometer of the XRD measurement.

Moreover, the quality of the crystalline thin films can be measured by XRD with the rocking curve method. In this measurement, 2θ is at an angle satisfying Bragg's law, and the diffraction intensity is plotted against ω. The full width half maximum (FWHM) along ω is a measure of the crystallinity of the films: the smaller the FWHM is, the higher the crystallinity is.

Lastly, XRD can also give information about the epitaxial relationship between film and substrate. This method is called reciprocal space mapping (RSM). In RSM measurement, reciprocal space in a specific region is mapped. The parameters 2θ and ω are transformed to the reciprocal space coordination (q_x, q_z). Since the lattice constants are related to the reciprocal lattice vectors, the lattice constants of the films can be determine from RSM measurements. RSM measurements of thin films can manifest the relation between the reciprocal lattices of film and substrate, giving important information whether the film is coherently grown.

2.2.3 Atomic force microscopy (AFM) [57-58]

Atomic for microscopy (AFM) is one of the powerful methods to characterize the surface morphology. AFM is a member of scanning probe microscopy family which detects interaction between the scanning probe and the surface and gives information about surface topography and various physical quantities. The atomic force between probe and surface could have either a positive or negative value, which presents repulsive or attractive force. In many cases, AFM is operated with the contact mode, where repulsive force is detected. Surface corrugation is detected by scanning the probe attached at the end of the cantilever. During the measurement, the probe traces the surface geometry, and the bending of the cantilever is detected by the laser beam reflected at the back-side of the cantilever. With scanning the probe over the sample surface, one can obtain surface topographic images. In this study, SPI4000 with SPA400 (SII-nanotechnology) is used.

2.3 Composition characterization

2.3.1 Energy dispersive X-ray spectroscopy (EDX)

Energy dispersive X-ray (EDX) spectroscopy uses electron beam to obtain information of the chemical compositions from the generated X-ray. This characteristic X-ray is produced because the irradiated electron beam has a higher energy than the binding energies of the electrons in inner shells. When an inner electron is ejected, a hole remains in the inner the shell. Consequently, an electron in a higher energy state (outer shell) falls to the inner shell to fill the hole, and characteristic X-ray is released to conserve the total energy inside the atom. Accordingly, the energy or wavelength of the characteristic X-ray is specific to each element. Using EDX spectroscopy, qualitative and semi-quantitative information about chemical composition can be obtained.

In EDX spectroscopy, controlling the energy of incident electron beam is very important because its penetration depth is an increasing function of the beam energy. In case of thin film samples, high energy incident electron beam reaches to the substrate, resulting in the generation of signals from both film and substrate. If the substrate and thin film contain the same element, the signal from substrate prevents quantitative analysis of the films. The beam energy should be reduced to get rid of this problem. Nonetheless, EDX measurements with high energy beam is favorable because of the following reasons:

- Low energy electron beam cannot excite electrons from the elements which have very deep inner energy levels (higher energy is required).
- Too low energy of electron beam results in poor signal-to-noise (S/N) ratio and peak resolution.

In this study, the acceleration voltage of electron beam was set at less than 2.5 eV, based on the simulation in each material. According to the simulation, the electrons accelerated by such low voltage penetrates 30-50 nm deep into the film, depending on the material.

Another disadvantage of EDX is the overlap of peaks. For example, L_α line of titanium at 452 eV and K_α line of nitrogen at 392 eV severely overlap with each other [59]. Therefore, it is unable to evaluate exact compositions of nitrogen and titanium in Ti-based oxynitride samples.

In this study, scanning electron microscopy equipped with EDX (JEOL JSM-7100F) was used.

2.3.2 Elastic recoil detection analysis (ERDA) [60]

Elastic recoil detection analysis is an ion beam analysis technique to determine the chemical composition and depth profile in thin films. In this technique, an energetic ion beam is irradiated to the sample to obtain unique information such as elastic nuclear interaction between the ion beam and the atoms of the sample, cross section, and loss of energy. As a result, elemental analysis can be quantitatively performed.

Ions with an atomic number (Z_1), atomic mass (M_1), and kinetic energy (E_1) in a range corresponding to the Rutherford scattering are bombarded to the sample, and energy (E_2) is transferred by the projectile ions to sample atoms of mass (M_2) with a recoil angle (θ), as follows:

$$E_2 = \left(\frac{4M_1M_2}{\left(M_1+M_2\right)^2} \cos^2\theta \right) E_1$$

The recoil cross-section for Rutherford scattering cross sections (in a cm^2 unit) for different targets and projectiles with (E_1) MeV energies was corrected by:

$$\sigma_R = 5.18\times10^{-27} \left[\frac{Z_1Z_2\left(M_1+M_2\right)}{M_2E_1} \right]^2 \frac{1}{\cos^3\theta}$$

We can also obtain quantitative depth profiling information on the basis of the energy loss before the recoil atoms (or ions) escape the sample surface. The energy of a recoil ion (E_{ds}), originated at depth d coming out at the surface, is given by:

$$E_{ds} = E_2 - dN\varepsilon_R$$

where N is the atomic density, and ε_R is the recoil stopping cross-section factor.

In this study, ERDA measurements were performed with Cl^{7+} with 38.4 MeV ion beams which was generated by a 5 MV tandem accelerator, located at Micro Analysis Laboratory, Tandem accelerator (MALT), University of Tokyo. The importance of ERDA technique is providing a fast quantitative concentration depth profiling of elements with good sensitivity and high resolution.

2.4 Characterization the physical properties

2.4.1 Electrical transport properties [62]

In this study, electrical properties were measured by van der Pauw 4-probe method. In this method, a current is flown between two electrodes, and voltage is measured between the other two electrodes. Because the voltmeter has high impedance, almost no current flows through the voltmeter. Thus, the voltage drop due to contact resistance is negligible. This method is applicable only to low resistance samples.

The experimental setup for 4-probe measurement is shown in Figure 2.5. For 4-probe measurements, usually, the film is patterned into a so-called Hall bar shape by using a Ti mask. In this study, I decided to use the van der Pauw method to prevent the contamination from Ti mask plate during the film fabrication. In van der Pauw method, the resistivity can measured for arbitrarily shaped samples. In this experiment, four electrodes were attached at the corners of the samples, and resistivity was measured with two geometries as shown in Figure 2.5(b) and (c). In Figure 2.5(b), an electric current is flown between electrodes A and B (I_{AB}), and the voltage drop between C and D (V_{CD}) is measured. On the other hand, in Figure 2.3(c), a current is flown between A and D (I_{AD}), and the voltage drop between B and C (V_{BC}) is measured. The resistivity (ρ) is calculated from resistance $R_{\mathrm{AB,CD}}$ and $\mathrm{R}_{\mathrm{BC,DA}}$ by the following equation:

$$\rho = \frac{\pi d}{In 2} \frac{R_{AB,CD} + R_{BC,DA}}{2} f \left(\frac{R_{AB,CD}}{R_{BC,DA}} \right)$$

where d is the thickness of the film and f is the van der Pauw correction factor to compensate the inhomogeneous of electrode position, irregular shape of the sample and others.

Hall effect measurements for evaluation of carrier density and Hall mobility were also conducted with the same channel geometry. By applying magnetic field (B_Z) perpendicular to the film surface, carriers flows from electrode A to C by the Lorentz force.

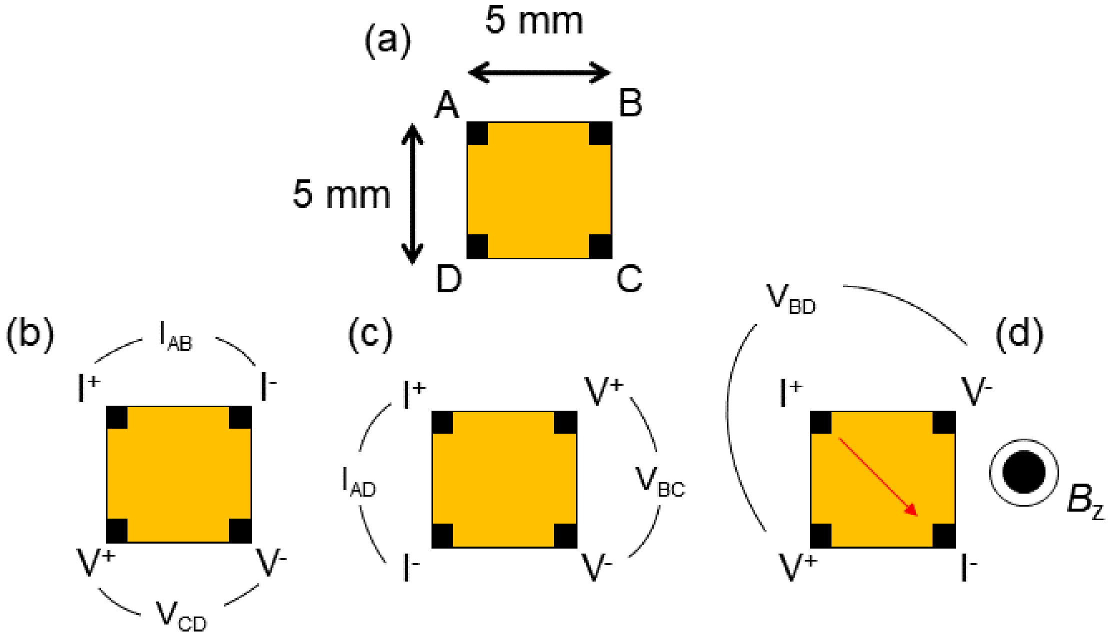

Figure 2.5. (a) Sample with four electrodes in van der Pauw method and geometries for (b), (c) four-probe method and (d) Hall resistance measurement.

This causes the gradient of carrier density in electrode B and D as shown in Figure 2.5(d). Assuming that there is only one type of carrier, the voltage between electrodes B and D (V_{BD}) is given by:

$$V_{BD} = \frac{-I_{AC}B_Z}{d \cdot n \cdot e}$$

where I_{AC} is the current flow from electrode A to C, and e is the elementary charge. With this, the Hall coefficient (R_H) is defined by the following equation:

$$R_H = \frac{V_{BD}}{I_{AC}B_Z} = \frac{R_{BD,AC}}{B_Z} = \frac{-1}{d \cdot n \cdot e}$$

where $R_{BC,AC}$ is the Hall resistance which is measured by four channel geometry of van der Pauw.

Moreover, this method can determine the carrier type from the sign of Hall coefficient: positive and negative R_H correspond to hole and electron carriers, respectively. Lastly, the Hall mobility is defined as:

$$\mu_H = \frac{R_H}{\rho}$$

2.4.2 Measurement of dielectric constant [63]

High resistance materials with large capacitance can be used as dielectric materials. Dielectric materials are used for energy storage of applied electric fields. Dielectric materials are characterized by two factors. One is the capacitance to store an energy which is related to dielectric constant (ε'), and the other is energy loss which is defined by dissipation factor (D).

In an AC current flow, the dissipation factor (D) is determined by the resistance and reactance. The smaller the dissipation factor is, the more ideal the capacitor is. With high dissipation factor value, the reactance of the circuit can be evaluated, but for accurate evaluation low dissipation factor is required. This value is also called loss tangent (tan δ), because it represents the tangent of angle δ of the impedance vector.

The dielectric constant is calculated from the following equation:

$$\varepsilon' = \frac{C \cdot d}{\varepsilon_0 \cdot S}$$

where ε_0 is the vacuum permittivity, d is the distance between electrodes, and S is the measured area. Dielectric constant and loss tangent values are frequency dependent. Therefore, in this study, impedance measurements were carried out in a wide frequency range of 20 Hz ~ 2 MHz. I used a LCR meter (Agilent, E4980) with 2-probe geometry. This measurement set-up is the simplest way to measure the dielectric constant but it is easily affected by the stray capacitance of cables.

2.4.3 Ultra violet-visible-near infrared spectroscopy

Optical properties, especially optical band gaps, of the films were determined by UV-Vis spectroscopy method. In the present UV-Vis experiments, transmittance (T) and reflectance (R) were measured from 200 nm to 2300 nm. The absorbance A was calculated by:

$$A = \frac{1 - T - R}{1 - R}$$

Furthermore, the absorption coefficient (α), which is generally used as a representing factor of materials instead of absorbance, was calculated by:

$$\alpha = \frac{1}{t} \ln\left(\frac{1 - R}{T}\right)$$

where t is the sample thickness. In this study, the thin films deposited on transparent substrates were used as samples. The absorption from the substrate was very week in the visible region, so that in the discussion about the band gaps of oxynitrides the effect of substrate was ingored.

2.4.4 Photoelectrochemical measurement [64-66]

Prior to characterization of photoelectrochemical material, attention needs be paid to the photoelectrodes. Apart from thin film preparation discussed before, care should be taken of the substrate. To provide smooth charge carrier transfer at the interface between film and substrate, it is necessary to achieve an ohmic contact, a linear current response to applied potential. Substrate may present the majority of carriers at the interface. Thus, it is needed to verify the achievement of ohmic contact and not Schottky barrier which reflects carriers back into the sample and blocks charge transport.

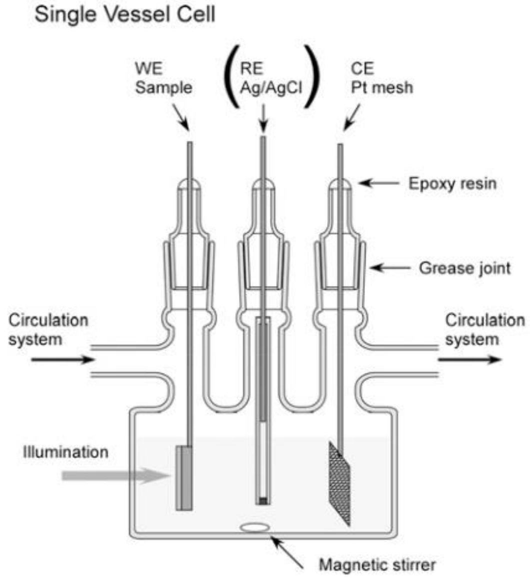

Figure 2.6. PEC cell in a single compartment configuration. Adapted and reprinted with permission from Cambridge University Press: Journal of Materials Research [64], copyright 2010

In fully conductive substrate which I used in this study, the connection was made on the backside of the substrate with silver conductive glue. Lastly, epoxy resin is used to protect all the electric wires from accidental detachment. This epoxy resin needs to be compatible with the electrolyte solution, usually basic solution, which was used for photoelectrochemical cell (PEC) measurements.

Figure 2.6 shows a basic PEC cell, in which there are three main electrodes; working electrode (WE), counter electrode (CE) and reference electrode (RE). The whole experimental setup consists of a light source, light filters, a chopper, a photoelectrochemical cell, and an electrical measurement tool. AM 1.5 G illumination is required for a light source; a Xe lamp with wavelength of 420 nm was used together with chopper attachment. For measurements of short-circuit current density, a low impedance ammeter was utilized. Pt was used as the counter electrode in this study. A large active surface area of CE is crucial for ensuring that the reaction of the sample is not limited by the reaction at the CE surface. For n-type samples, H^+ is reduced into hydrogen gas via the hydrogen evolution reaction (HER) at CE. Lastly, Ag/AgCl was employed as the reference electrode for basic solution (pH 13). This RE is generally used in a wide pH range. In this system, the relationship between the RE potential and reversible hydrogen electrode (RHE) at room temperature is expressed by the following equation:

$$E_{RHE} = E_{Ag/AgCl} + 0.059 \cdot pH(13) + 0.197$$

Chapter 3

Self-seed layer enhanced low temperature growth of single-phase of baddeleyite NbON epitaxial thin films

3.1 Introduction

Transition metal oxynitrides with d^0 electronic configuration have been broadly studied because of its high photocatalytic activity under visible light [67-74]. Among these oxynitrides, tantalum oxynitride (TaON) which is one of the promising visible-light active photocatalyst. Baddeleyite tantalum oxynitride (β-TaON) has a smaller in band gap (E_g = 2.5 eV) which refers to the absorption edge at 500 nm [67], as shown in Figure 3.1, which is red-shifted from that of oxide precursor, as mentioned in Chapter 1. This compound has both sufficiently negative conduction band for H_2 production and a narrow band gap with visible light absorption. Indeed, it was confirmed that β-TaON could oxidize water with maximum quantum yield of 10% under visible irradiation [67-69].

---

* This chapter contains the contents of the following publication.
"Epitaxial Growth of Baddeleyite NbON Thin Films on Yttria-stabilized Zirconia by Pulsed Laser Deposition,"
Vitchaphol Motaneeyachart, Yasushi Hirose, Atsushi Suzuki, Shoichiro Nakao, Isao Harayama, Daiichiro Sekiba, and Tetsuya Hasegawa,
Chemistry Letters, **47**, 65 (2018)
- Published by The Chemical Society of Japan (CSJ)

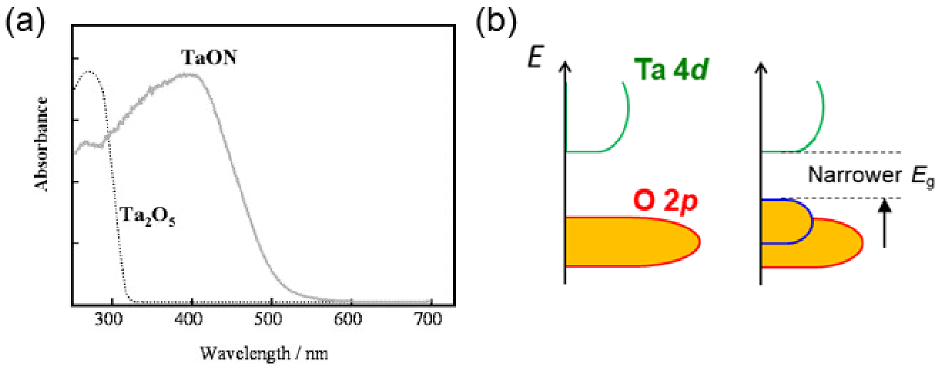

Figure 3.1. UV-Vis diffuse reflectance spectra of TaON and Ta_2O_5 (a), and schematic images of band structure of Ta_2O_5 and TaON (b). Adapted and reprinted with permission from Elsevier: Catalysis Today [75], copyright 2004

The first experimental result for photoelectrochemical water splitting by bulk β-TaON is shown in Figure 3.2. Photocurrent in basic solution was measured under the visible light irradiation, where CoO_x was used as a co-catalyst. From this experiment, it was claimed that CoO_x/TaON had high incident photon-to-current conversion efficiency (IPCE) and was superior in long-term stability, which is required for practical uses. The evolved gases showed almost stoichiometric ratio (336 μmol of H_2 gas and 167 μmol of O_2 gas). In conclusion, TaON exhibited stable photoelectrochemical water splitting under visible light with high IPCE efficiency. However, high cost of Ta prevents its applications.

A Nb-based ternary oxynitride, NbON, is a possible alternative to β-TaON because Nb is more abundant than Ta and the electronic configurations and ionic radii of Nb^{5+} and Ta^{5+} are the same [76]. Furthermore, *4d* transition metals (Nb) have larger electronegativity than *5d* ones (Ta), and therefore the Nb t_{2g} orbital is shallower in energy than Ta one [77]. In other words, NbON has a smaller band gap than TaON because the conduction band minima of NbON is more positive (Figure 3.3). This tendency is widely seen in Nb- and Ta-based d^0 oxides. There is only one publication reporting the

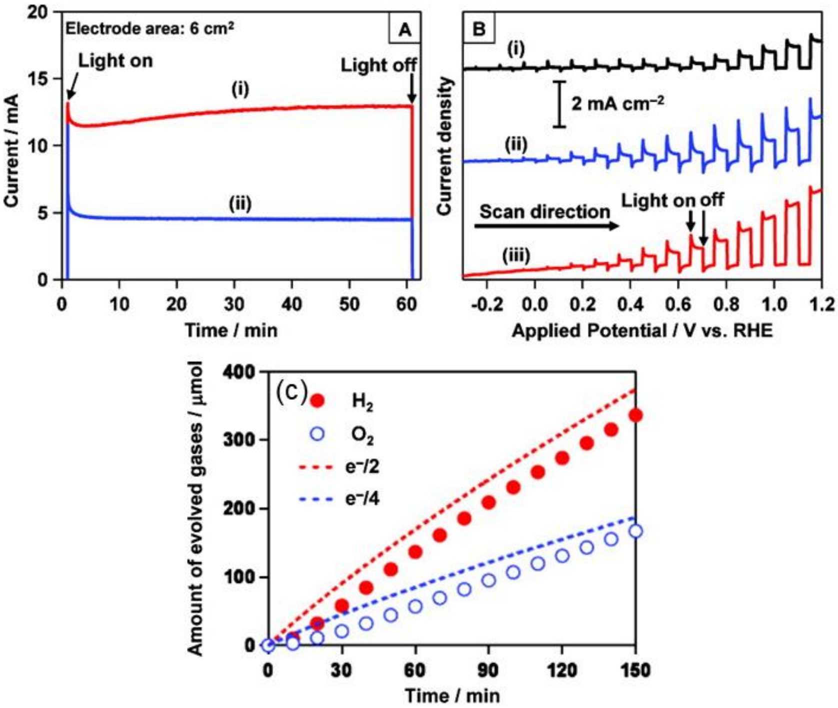

Figure 3.2. (a) Time courses of the photocurrent of CoO_x/TaON electrode in (i) sodium phosphate buffer (ii) Na_2SO_4 solution under visible light irradiation, (b) Current-potential curves under chopped visible light irradiation for (i) unloaded TaON in Na_2SO_4 solution (ii) CoO_x/TaON in aqueous Na_2SO_4 (iii) CoO_x/TaON in aqueous Na_2SO_4 buffer, and (c) time courses of gas evolution for CoO_x/TaON electrode under visible light irradiation. Adapted and reprinted with permission from American Chemical Society: Journal of the American Chemistry Society [80], copyright 2012

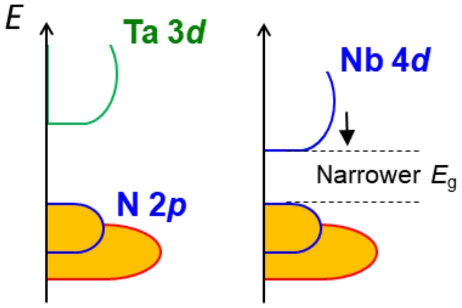

Figure 3.3. Comparison of band structures between TaON and NbON.

absorption edge of polycrystalline samples (Figure 3.4) baddeleyite NbON thin film is smaller than TaON [78], although baddeleyite NbON has been scarcely studied so far [78-79], mainly due to the difficulty in synthesis. In this study, I fabricated single crystal baddeleyite NbON epitaxial thin film for enhancing photoelectrochemical efficiency and understanding the physical properties.

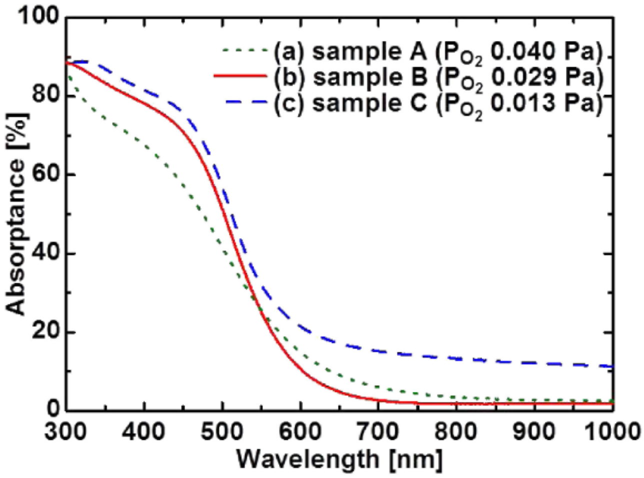

Figure 3.4. UV-Vis absorption spectra: (a) sample A (P_{O2} 0.040 Pa), (b) sample B (P_{O2} 0.029 Pa), and (c) sample C (P_{O2} 0.013 Pa). Reprinted with permission from The Electrochemical Society of Japan: Electrochemistry [81], copyright 2015 (Open Access)

3.2 Selection of substrate

This study, nitrogen plasma assisted pulsed laser deposition method [38] was used to fabricate baddeleyite NbON epitaxial thin film. (100) plane of yttria-stabilized zirconia (YSZ) single crystal substrate was used based on a previous report on epitaxial growth of β-TaON [79]. In addition, YSZ (100) substrate has a fluorite structure which has the same atomic arrangement as baddeleyite structure; baddeleyite structure can be regarded as a monoclinically distorted fluorite structure [82]. The lattice constant of YSZ (100) are nearly the same as NbON (YSZ: 5.15 Å, calculated NbON: 5.19 Å [76]) (figure 3.5).

The lattice mismatching between bulk NbON and substrate is about 1% which is acceptable, as discussed in Chapter 1. Therefore, the epitaxial force from the substrate is expected to stabilize the baddeleyite lattice of film. Moreover, YSZ substrate is transparent, thus, it will not hinder optical property measurements. Furthermore, it is very stable when pre-heated at high temperature and it shows a very high resistance, which is suitable for transport property measurement.

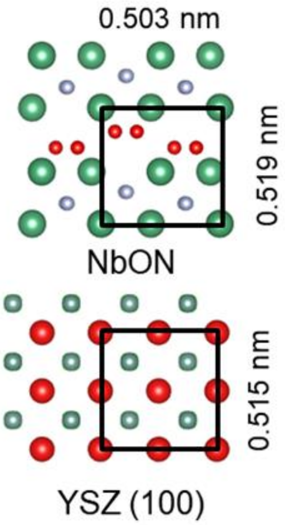

Figure 3.5. Atomic arrangement of baddeleyite NbON (top) and YSZ (100) substrate (bottom) with lattice constants.

3.3 Optimization of substrate temperature (*T*s)

Baddeleyite NbON films on YSZ (100) substrate were fabricated in the following conditions:

Radical source	: radio frequency with input power 350W
Target	: $Nb_2O_{4.8}$ (commercial target)
Substrate	: YSZ (100)
Growth temp. (˚C)	: 475, 500 and 600 ˚C
Repetition rate	: 3 Hz
Atmosphere	: N_2 gas with $1x10^{-5}$ Torr

The target was gradually degraded while repeating the deposition run, so that the laser energy was increased from 8 mJ to 15 mJ in order to keep the deposition rate constant, 10 ~ 15 nm /hour.

Figure 3.6(a) shows θ-2θ XRD patterns of the NbO_xN_y thin films grew on YSZ (100) substrate with various substrate temperature *T*s. The samples fabricated at *T*s ≤475 ˚C showed a weak or undetected peaks, indicating that the films were essentially amorphous. On the other hand, for the films grown at *T*s ≥500 °C, clear diffraction peaks were observed at $2\theta \sim 17^\circ$, 36˚, 55˚, and 76˚ which corresponded to 100, 200, 300 and 400 diffractions of baddeleyite NbON, respectively. Moreover, no impurity phases such as Nb_2O_5 and rock-salt NbO_xN_{1-x} were detected. The diffraction peaks became more intense and sharper with increase of *T*s due to enhanced crystallinity. As a consequence, it was found that *T*s at 500 ˚C was a critical temperature to obtain the baddeleyite phase.

Higher *T*s is beneficial for crystallization of baddeleyite phase but it causes substantial off-stoichiometry due to release of nitrogen, as shown in Figure 3.6(b). The EDX spectrum of the NbO_xN_y film grown at *T*s = 600 ˚C showed almost no nitrogen peak. Nitrogen deficiency was also recognized from the color of the film. Oxynitrides are novel inorganic pigments, and therefore the color of oxynitrides changes with respect to the nitrogen/oxygen ratio, as discussed in Chapter 1. Indeed, stoichiometric films have yellowish color, while nitrogen deficient films showed black color. The films obtained at *T*s ≤500 ˚C had yellowish color while he films fabricated at *T*s >500 ˚C turned to be darker to black color.

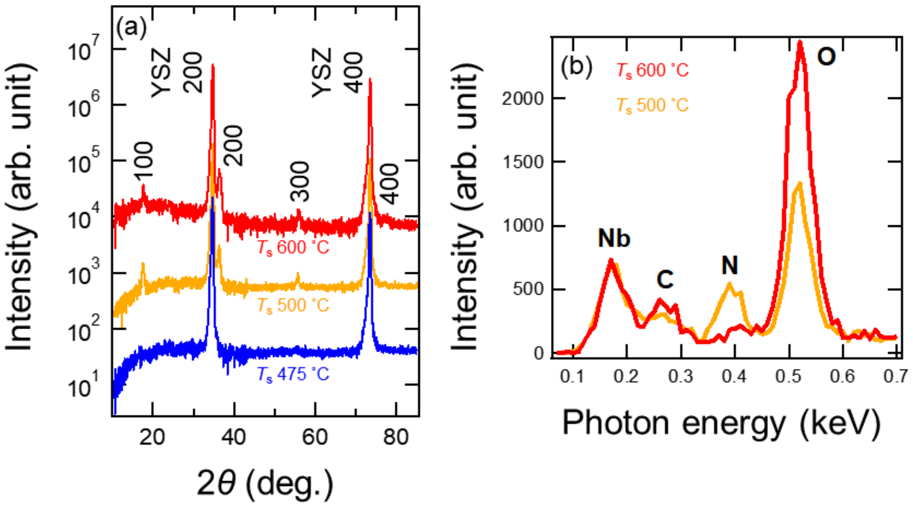

Figure 3.6. (a) θ-2θ XRD patterns of the NbO_xN_y thin films grew on YSZ (100) substrate at various *T*s, and (b) EDX spectra of NbO_xN_y thin films.

There is a dilemma that low *T*s is required for obtaining the stoichiometric films but the film hardly crystallizes. Although high *T*s is effective for the crystal growth, nitrogen deficiency is introduced. This is because nitrogen atoms in oxynitrides are unstable and they are easily released at high temperature. As mentioned before, the critical *T*s to grow baddeleyite phase is 500 ˚C. In the next section, I will discuss the reproducibly of the baddeleyite NbON film grown at critical *T*s.

3.4 Reproducibility of baddeleyite phase at critical *T*s = 500 ˚C

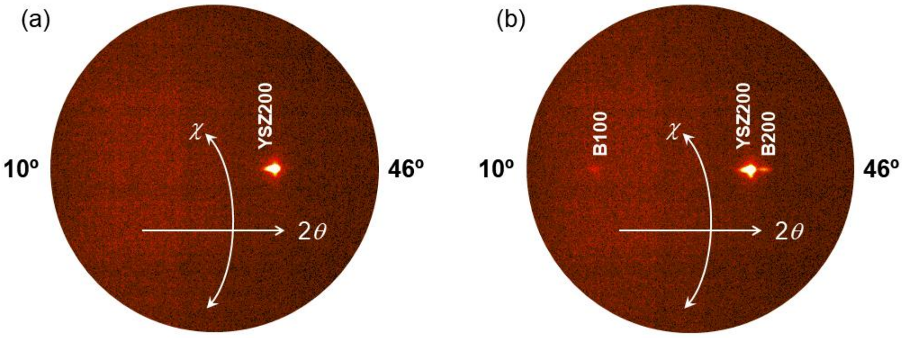

Figure 3.7. Area detector images of XRD patterns of two samples fabricated at *T*s = 500 ˚C.

The purpose of this experiment was to confirm the reproducibility of the film grown at *T*s = 500 ˚C. Figure 3.7 shows XRD data of two different samples fabricated with the same condition. Contrary to my expectation, the two samples showed very different results: one was crystallized and the other was amorphous. There might be some uncontrollable factors, such as a trace amount of gases inside the chamber, which govern the crystallization of NbON. It is also possible that slight deviation of *T*s from 500 ˚C largely affect the crystallization. That is, it is speculated that NbON is highly sensitive to the growth temperature which has an effect on both chemical composition and crystal phase. In conclusion, the films directly deposited on YSZ (100) substrate at *T*s = 500 ˚C were not stable enough to obtain baddeleyite phase. To overcome this difficulty, I reduced crystallization temperature of baddeleyite NbO_xN_y by introducing a self-seed layer [48, 83] as discussed in Chapter 1. In the next section, I describe the influence of the self-seed layer on crystal growth and surface morphology.

3.5 Introduction of self-seed layer

As is well known, use of seed layer helps to control the structure, texture and morphology of the main layer deposited on it [84]. Therefore, I expected that the epitaxial force form seed layer will be high enough to stabilize thin film even at lower *T*s. In this study, I chose NbO_xN_y as a seed layer because there was no lattice mismatch between the seed layer and the film. For the seed layer, crystallinity takes the first priority rather than chemical composition. Thus, the self-seed layer was fabricated at relatively high *T*s, as follows.

Radical source : radio frequency with input power 350W
Target : $Nb_2O_{4.8}$ (commercial target)
Substrate : YSZ (100)
Growth temp. (˚C) : 600 ˚C
Repetition rate : 3 Hz
Atmosphere : O_2 gas with $1x10^{-7}$ Torr
N_2 gas with $1x10^{-5}$ Torr

Figure 3.8(a) shows the θ-2θ XRD diffraction patterns of the self-seed layer. Sharp peaks from baddeleyite structure were clearly observed, indicating high crystallinity of the seed layer. The chemical composition of the film measured by EDX is shown in Figure 3.8(b). The EDX result showed that the self-seed layer is nitrogen deficient despite introduction of both O_2 and N_2 gases during the fabrication. Lastly, the surface morphology of self-seed layer is presented in Figure 3.8(c).

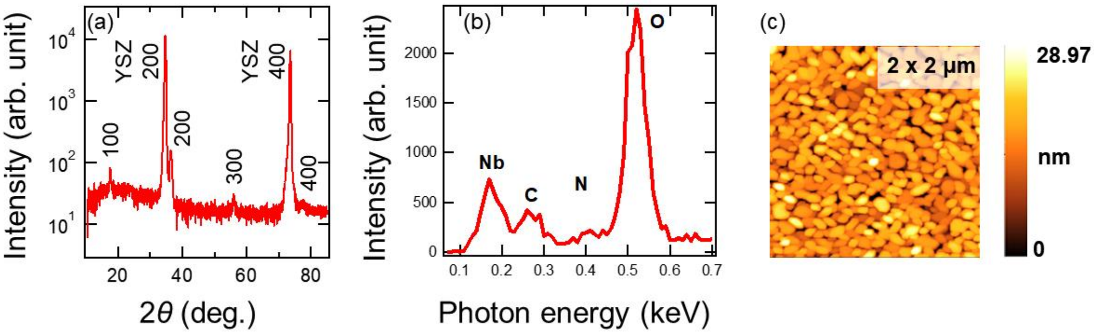

Figure 3.8. (a) θ-2θ XRD patterns of the NbO_xN_y self-seed layer fabricated at *T*s 600 ˚C grown on YSZ (100) substrate, (b) EDX spectrum of self-seed layer, and (c) surface morphology of self-seed layer by AFM.

As seen from the surface morphology, the self-seed layer had large grain size and rough surface. The grain size was about 100 nm with ~29 nm height. In addition to surface roughness, the grain direction is irregularly distributed due to multiple domains of baddeleyite structure, as manifested by the low intensity of the XRD diffraction peaks. Moreover, the resistance measured by two-probe method was high enough not to hinder transport properties measurements.

3.6 Two-step growth of baddeleyite NbON with self-seed layer

The process employed in this study is shown in Figure 3.9. First, a ~1 nm thick seed layer of baddeleyite NbO_xN_y was epitaxially grown on YSZ (100) substrate at *T*s = 600 °C under mixture of oxygen gas (partial pressure of 1×10^{-7} Torr) and activated nitrogen gas. Then, a 40 nm-thick NbO_xN_y film was grown on this seed layer at *T*s = 500 °C under the activated nitrogen gas without O_2 gas introduction.

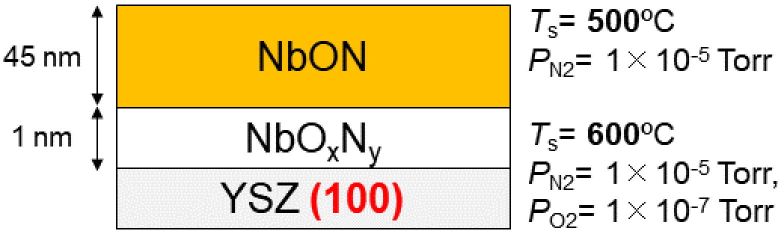

Figure 3.9. Schematic illustration of the NbON with two-step growth process.

During the fabrication of seed layer, RHEED was used as a method to monitor the crystallinity of the seed layer surface. Figure 3.10 shows RHEED patterns of the film surface before and after self-seed layer deposition. The RHEED pattern of YSZ (100) substrate showed very intense streaks (t = 0 s) which represent atomically flat surface with perfect single-crystalline structure. After starting deposition at t = 60 s, the RHEED pattern became weaker, reflecting that an ultra-thin layer has been growth on the surface. After that, at t = 300 s, the RHEED pattern recovered its original shape nearly the same as substrate. Therefore, I decided to fabricated self-seed layer for t = 300 s before fabricating the main layer which has the thickness of about 1 nm.

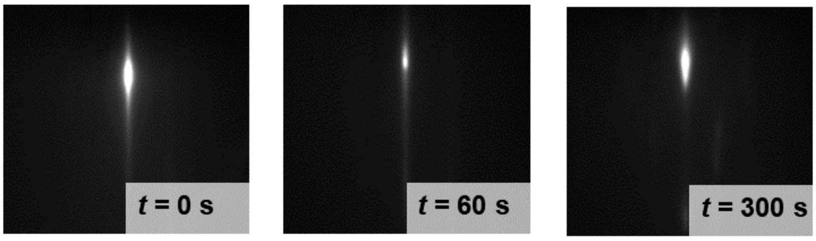

Figure 3.10. Schematics of RHEED patterns of self-seed layer deposition on YSZ (100) substrate with different in deposition time.

The RHEED pattern of the NbO$_x$N$_y$ main layer is shown in Figure 3.11. It presented the modulated streak pattern, indicating single-crystalline surface with multilevel stepped surface or multiple domains. The detail of the crystal structure was determined by XRD. Out-of-plane and in-plane θ-2θ XRD patterns of the NbO$_x$N$_y$ film prepared with the two-step growth method are shown in Figure 3.12(a).

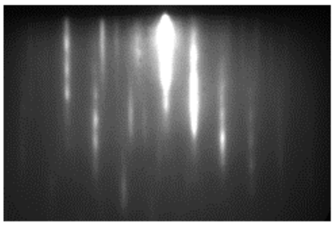

Figure 3.11. Schematic of RHEED patterns of NbO_xN_y grown with two-step growth method.

The XRD pattern proved epitaxial growth of a (100)-oriented baddeleyite NbO_xN_y phase. The lattice constants and β angle were calculated from the following equation:

$$\frac{1}{d^2} = \frac{1}{\sin^2\beta}\left(\frac{h^2}{a^2} + \frac{k^2\sin^2\beta}{b^2} + \frac{l^2}{c^2} - \frac{2hl\cos\beta}{ac}\right)$$

The calculated values were a, c = 4.99 Å, b = 4.97 Å, and β = 102.8°. As compared to theoretical values [85], my film had a little smaller lattice, possibly due to silight non-stoichiometry or epitaxial strain from the self-seed layer.

The chemical composition of the film was nearly stoichiometric, $NbO_{0.9\pm0.1}N_{1.0\pm0.1}$ (*ERDA normalization*), as seen from the EDX data in Figure 3.12(b). The nominal oxidation state of Nb in this film is around +4.8, suggesting formation of a small amount of oxygen deficiency. Hereafter, I will refer to this sample as NbON and discuss its properties.

φ-scan plot of 111 diffraction of the baddeleyite NbON thin film (Figure 3.12(c)) showed four-fold rotational symmetry, confirming multiple domain structure originating from monoclinic symmetry of baddeleyite structure. The epitaxial relationships between the film and substrate were $(100)_{\mathrm{NbON}}$ // $(100)_{\mathrm{YSZ}}$ and $[001]_{\mathrm{NbON}}$ // $[001]_{\mathrm{YSZ}}$, as similar to the case of β-TaON epitaxially grown on YSZ (100) [86]. AFM images of the baddeleyite NbON film showed small grain-like structure (Figure 3.12(d)) reflecting the multiple domain.

Figure 3.13 is an XRD area detector image of the NbON film, where spitting of 111 and 11-1 peaks proves monoclinic phase. In conclusion, I succeeded in fabricating single crystalline baddeleyite NbON thin film with two-step growth method.

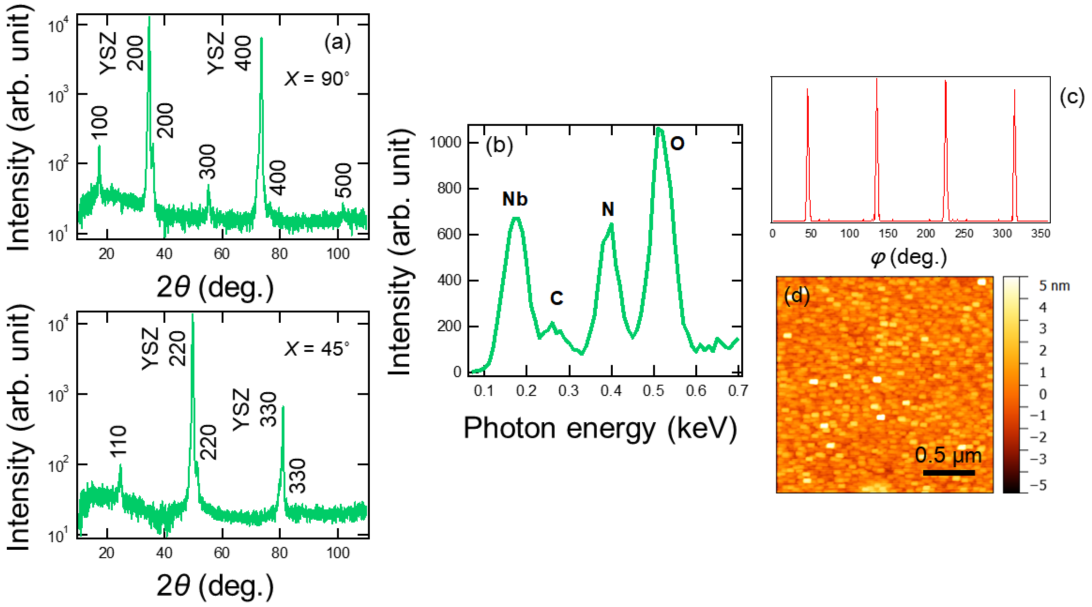

Figure 3.12. (a) θ-2θ XRD patterns of both *in-plane* and *out-of-plane*, (b) EDX spectrum, (c) φ-scan plot of 111 diffraction, and (d) AFM image of the baddeleyite NbON thin film grew at Ts = 500 ˚C with a self-seed layer.

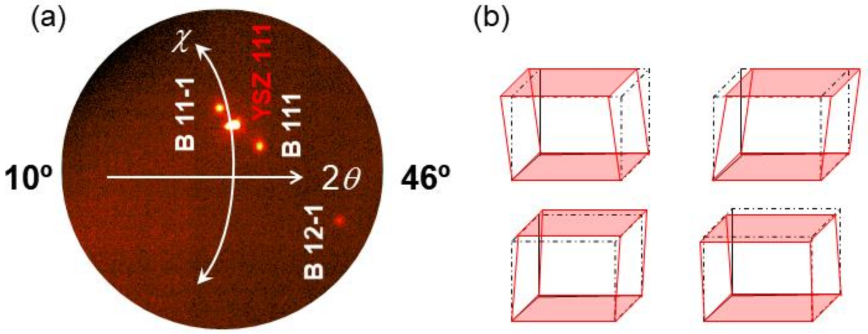

Figure 3.13. (a) Area detector images of XRD pattern of 111 and 11-1 diffraction peaks, and (b) schematic model of the monoclinic phases.

3.7 Physical properties of baddeleyite NbON

As mention in Chapter 1, materials with narrow band gaps will enhance the photoelectrochemical activity due to widened visible light absorption. Figure 3.14 shows the optical transmittance T, reflectance R, and absorptance A (= $100-T-R$) of the baddeleyite NbON thin film. The absorption spectrum showed clear visible light absorption at the absorption edge around 540 nm (E_g = ~2.3 eV).

This value is smaller than the bandgap of β-TaON (2.5 eV) [67], although it was slightly larger than that of the polycrystalline thin films from the previous report (2.1 eV) [78]. I also observed large in-gap absorption from 500 nm to 2000 nm possibly due to defect states related to the above-mentioned oxygen deficiency or formation of amorphous or nanocrystalline NbN_x [78] that could not be detected by XRD measurement. From the Tauc plot, the optical band gap of NbON was related to the indirect transition. In indirect transition, the crystal momenta are different between conduction band and valence band in the Brillouin zone [87]. Photon cannot be emitted directly but the electron must pass through an intermediate state and transfer momentum to the crystal lattice to conserve the total crystal momentum and energy [88].

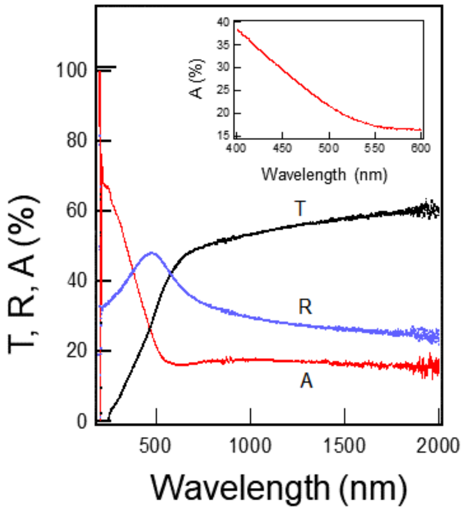

Figure 3.14. Optical transmittance, reflectance and absorptance spectra of baddeleyite NbON thin film grew at Ts = 500 ˚C with a self-seed layer. Insert shows a magnification of the absorptance spectrum around the absorption edge.

The electrical properties of baddeleyite NbON film were also investigated. The resistance (R) was ~12 kΩ by four-probe measurement. As shown in Figure 3.15(a), the I-V curve shows a straight line, obeying Ohm's law ($V = IR$). This implies that an ohmic contact was achieved between the film and the electrodes.

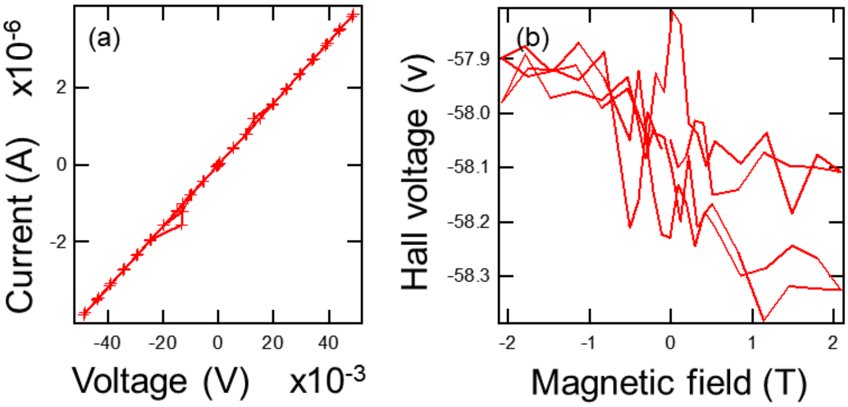

Figure 3.15. (a) *I-V* curve of baddeleyite NbON with a self-seed layer, and (b) Hall voltage as a function of magnetic field.

Electrical resistivity of the film was 2.5×10^{-1} Ωcm, which was calculated from the equation: $\rho = R \cdot (S/d)$ where S is the cross-sectional area and d is the distance between electrodes. Furthermore, the carrier density (n_e) and mobility (μ) were also determined by using the $\rho = (en\mu)^{-1}$ equation. As seen from Figure 3.15(b), Hall measurement indicated *n*-type carrier conduction, suggesting that the carrier electrons originate from anion vacancies similar to the cases of TaON [38] and oxide semiconductors. The n_e and μ values were determined as $n_e = 1.5\times10^{22}$ cm^{-3} and $\mu = 1.6\times10^{-3}$ $\text{cm}^2\text{V}^{-1}\text{s}^{-1}$, respectively. I consider that such high n_e value could not be attributed only to anion vacancies but also might originate from NbN_x phase as suggested by the in-gap optical absorption as discussed before. The small μ value is probably due to carrier scattering by densely populated defects and grain boundaries associated with the multiple domain structure mentioned above.

3.8 Conclusions

In conclusion, baddeleyite NbON thin films were successfully grown on YSZ (100) substrates by using nitrogen plasma assisted pulsed laser deposition method. Introduction of thin self-seed layer enabled to lower the film growth temperature, resulting in almost stoichiometric chemical composition.

The baddeleyite NbON thin film showed E_g value of ~2.3 eV, which is smaller than that of β-TaON. These results indicated that low temperature epitaxial growth is a promising approach to investigate the properties of baddeleyite NbON but still insufficient to avoid the reduction of Nb perfectly. On the other hand, further improvement of anion stoichiometry and suppression of multiple domain structure would be necessary for obtaining high-quality NbON thin films with high electron mobility.

To improve the film quality, I attempted to synthesize NbON films with different crystal structure. With tetragonal crystal system (Figure 3.16), the problems related to the multiple domain can be solved. From calculation for various crystal phases of NbON [89], rutile structure is suggested. Unfortunately, I failed to obtain stoichiometric rutile NbON film due to its chemical instability. The detail of the synthesis method of rutile NbON is described in Appendix Chapter A.

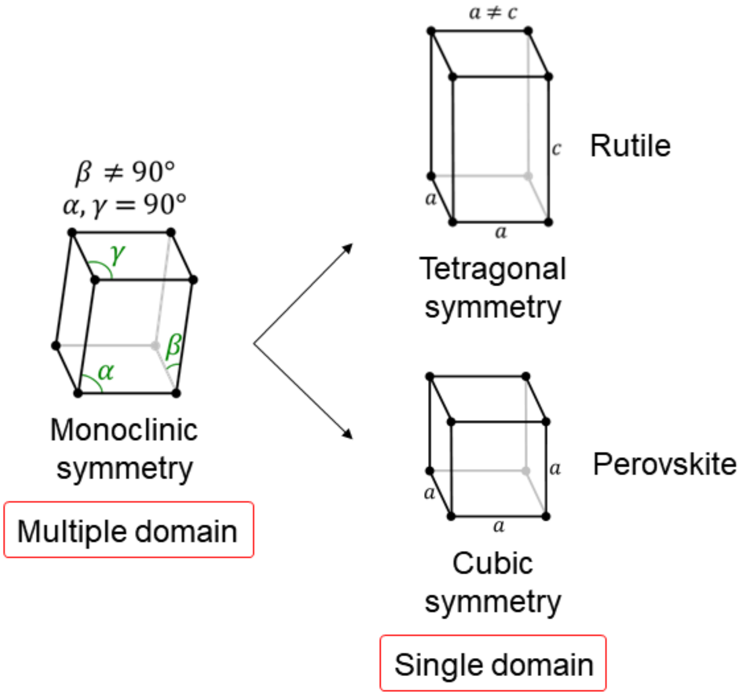

Figure 3.16. Schematics illustration of the polymorphs.

Because it is difficult to reduce the bandgap of ternary oxynitride with chemically unstable Nb^{5+}, I next focused on perovskite-type (cubic crystal system, Figure 3.16) quaternary Ta-based oxynitride semiconductor, such as ATaO$_2$N (A = Ca, Sr, and Ba). In these compounds, structural modification by

A-site cation enables narrower bandgap than those of ternary oxynitrides. In the next chapter, I will describe synthesis of perovskite-type quaternary Ta-based oxynitride semiconductor with nitrogen plasma assisted pulsed laser deposition.

Chapter 4

Buffer-layer-enhanced growth of single-domain perovskite $BaTaO_2N$ epitaxial thin films

4.1 Introduction

Among perovskite quaternary oxynitrides, $BaTaO_2N$ is particularly promising as a material for high efficiency solar water splitting because it has the smallest absorption edge (~1.9 eV) [94] (Figure 4.1) with chemically stable Ta^{5+} ion. The photocurrent observed for perovskite $BaTaO_2N$ with Co cocatalyst is as high as >4 mA cm^{-2} under standard AM 1.5G sunlight [96-97] and stables in long usage which is appropriate for practical uses. The H_2 and O_2 gases evolved by $BaTaO_2N$ photoanode were confirmed to be >90% of the ideal value expected from the photocurrent generated by the $BaTaO_2N$ electrode. These photocatalytic activities data are shown in Figure 4.2. However, there are a few reports on the synthesis of $BaTaO_2N$ epitaxial thin films [95, 98] due to the lack of commercially available single crystalline substrate with good lattice matching.

In a previous report, an epitaxial thin film of $BaTaO_2N$ (a = 4.113 Å) was deposited on a $SrTiO_3$ (a = 3.905 Å) single crystal substrate with a pseudo-cubic $SrRuO_3$ (a = 3.95 Å) [99] buffer layer, where the lattice mismatch between $BaTaO_2N$ and $SrRuO_3$ buffer layer was ~4.1%. They succeeded in fabricating a pure phase of perovskite $BaTaO_2N$. Unfortunately, cross-sectional TEM (XTEM) measurements revealed that the $BaTaO_2N$ film had small grains at the interface, as shown in

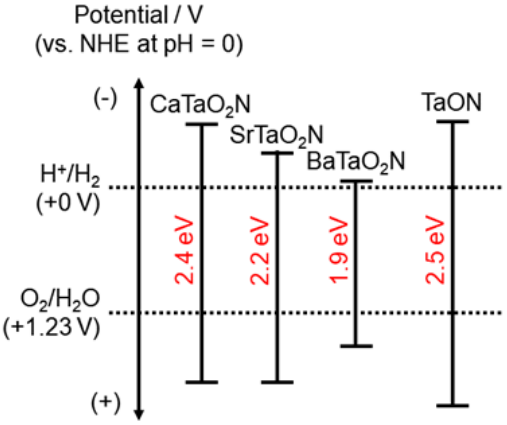

Figure 4.1. Positions of the conduction and valence bands and band gap values of Ta-based oxynitrides.

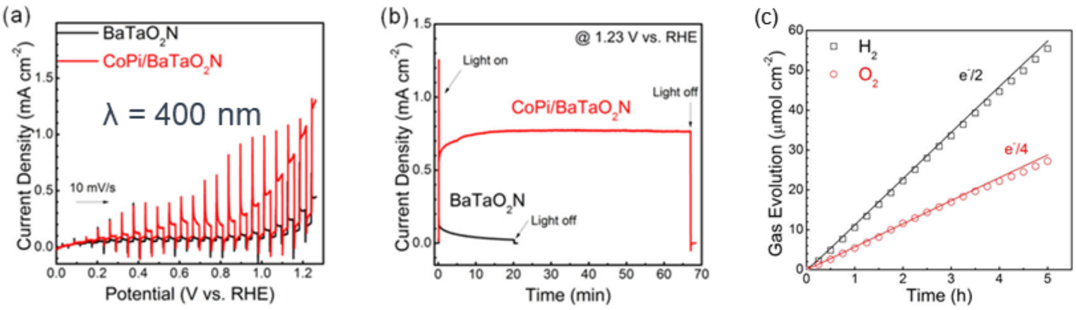

Figure 4.2. (a) Current-potential curves for CoPi-covered $BaTaO_2N$ electrodes, (b) current-time curve for CoPi/$BaTaO_2N$ held at 1.23 V versus RHE, and (c) hydrogen and oxygen evolution from a CoPi/$BaTaO_2N$ photoanode held at 1.23 V versus RHE in pH 13. Adapted and reprinted with permission from American Chemical Society: The Journal of Physical Chemistry C [96], copyright 2016

Figure 4.3. Moreover, the film suffered from surface defects due to large lattice mismatch between the buffer layer and thin film. As discussed in Chapter 1, defects will lead to electron-hole recombination and thus to decrease in photocatalytic activity. Therefore, lattice matched buffer is required to improve the crystallinity, surface flatness and surface tensile strain for reducing the density of defects.

Recently, it was reported that $BaSnO_3$ [100-101], of which lattice constant is well matched with $BaTaO_2N$ (+0.1% mismatch), could be fabricated on $SrTiO_3$ (STO) substrates (−5.4% mismatch) by pulsed laser deposition method. Figure 4.4(a) shows the atomically flat surface of $BaSnO_3$/(Sr,Ba)SnO_3/$SrTiO_3$ after annealing in air at high temperature.

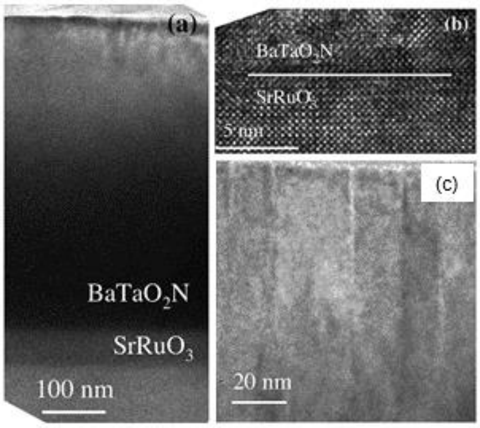

Figure 4.3. XTEM images of a $BaTaO_2N/SrRuO_3/SrTiO_3$ film with (a) and (c) for low-magnification of the cross-section, and (b) for high-magnification. Adapted and reprinted with permission from American Chemical Society: Chemistry of Materials [98], copyright 2007

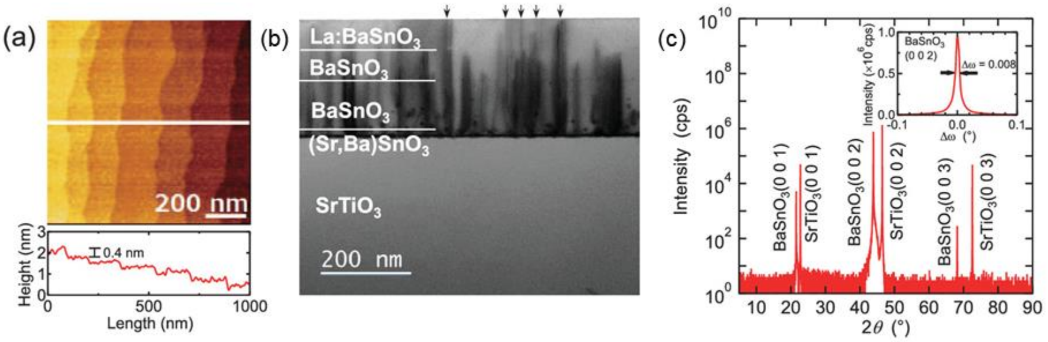

Figure 4.4. (a) Atomic force micrograph of annealed $BaSnO_3$/(Sr,Ba)SnO_3 directly grown on $SrTiO_3$, (b) cross-sectional bright-field (BF) image of TEM, and (c) θ-2θ XRD patterns of $BaSnO_3$ with insert rocking curve of $BaSnO_3$ (0 0 2) diffraction peak. Adapted and reprinted with permission from CC BY 4.0: AIP Advances [101], copyright 2016 (Open Access)

Figure 4.4(b) presents the cross-sectional STEM image of the film. It was obviously demonstrated that with a thicker film, defects were largely reduced on the surface. It was also claimed that by inserting the (Sr,Ba)SnO_3 buffer layer, the amount of the dislocation defects was decreased. The XRD pattern in Figure 4.4(c) shows single phase of $BaSnO_3$ without impurity phases. As seen from the insert, the rocking curve of (0 0 2) diffraction shows the full width at hall maximum (FWHM) value as narrow as 0.008˚ which indicates high crystallinity with less number of defects. Moreover, $BaSnO_3$ has a large band gap (E_g = 3.7 eV [103]), which implies almost no contribution to visible light absorption. Indeed, its transparency is experimentally confirmed in a wide energy range up to ultraviolet light.

Furthermore, $BaSnO_3$ is thermally stable up to 530 ˚C [102]. Consequently, $BaSnO_3$ is supposed to behave as a good buffer layer for a perovskite oxynitride $BaTaO_2N$ with a large lattice constant.

Therefore, in this study, I fabricated single crystalline perovskite $BaTaO_2N$ epitaxial thin films with improved crystallinity and surface morphology by inserting a $BaSnO_3$ buffer layer for enhancing photoelectrochemical efficiency.

4.2 Fabrication condition to fabricate $BaSnO_3$ buffer layer

The conditions to fabricate $BaSnO_3$ (cubic, a = 4.116 Å) buffer layer were based on the previous report [101], where $BaSnO_3$ and $Sr_{0.5}Ba_{0.5}SnO_3$ were used as ceramic targets. Films were grown by using PLD on (001) and (110)-oriented $SrTiO_3$ single crystal substrates. Before the fabrication, $SrTiO_3$ substrates were annealed at T = 1050 ˚C under air atmosphere for preparation of clean and atomically flat step-and-terrace surfaces. Ceramic targets of $BaSnO_3$ and $Sr_{0.5}Ba_{0.5}SnO_3$ were ablated by KrF excimer laser (λ = 248 nm). Energy fluence of excimer laser was adjusted to around 15 mJ with frequency of 2 Hz in order to control the deposition rate at 1-2 nm/min. Substrate temperature (Ts) was 900 ˚C under the oxygen partial pressure of 100 mTorr. The structure of the buffers is schematically illustrated in Figure 4.5.

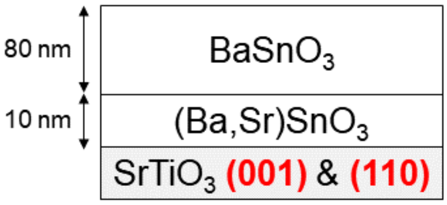

Figure 4.5. Schematic illustration of perovskite $BaSnO_3$ / $Sr_{0.5}Ba_{0.5}SnO_3$ buffer on $SrTiO_3$ substrate.

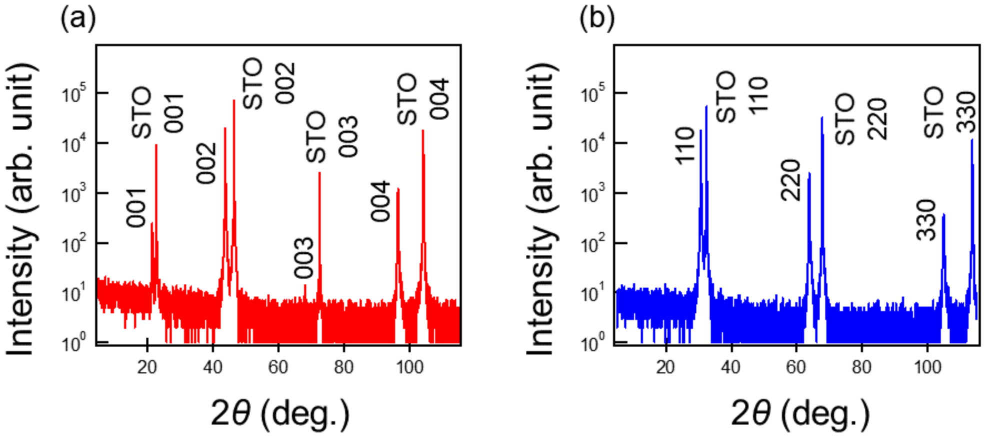

Figure 4.6. θ-2θ XRD patterns of the (a) (001)-oriented and (b) (110)-oriented BaSnO$_3$ epitaxial thin films grown on Sr$_{0.5}$Ba$_{0.5}$SnO$_3$ / SrTiO$_3$ at Ts = 900 ˚C.

Figure 4.6(a) shows θ-2θ XRD patterns of the BaSnO$_3$ thin films grown on Sr$_{0.5}$Ba$_{0.5}$SnO$_3$ / STO (001) substrate. Diffraction peaks were observed at 2θ ~ 21˚, 44˚, 68˚, and 96˚ which corresponded to the 001, 002, 003, and 004 diffraction from perovskite BaSnO$_3$, respectively. On the other hand, as shown in figure 4.6(b), the (110)-oriented BaSnO$_3$ thin film exhibited peaks at 2θ ~ 31˚, 64˚, and 105˚ which corresponded to 110, 220, and 330 diffraction, respectively. Moreover, both films were confirmed to be single crystalline without impurity phases. From the XRD results, it was proved that single phases of (001)- and (110)-oriented perovskite BaSnO$_3$ were successfully obtained by using PLD method. The lattice constant was evaluated as a = 4.13 Å, which is somewhat larger than that previously reported, 4.112 Å, possibly due to slight non-stoichiometry or epitaxial strain from the substrate.

The crystallinity of the films was evaluated from ω-scan rocking curves. Figure 4.7 compares the rocking curves of (002) and (110) reflections for the (001)- and (110)-oriented BaSnO$_3$ buffer layers, respectively. The FWHM of the (002) rocking curve is 0.03˚ which is one order of magnitude smaller than that of (110) rocking curve, 0.3˚. This demonstrates that the crystalline quality of (001)-oriented BaSnO$_3$ buffer is much superior to that of (110)-oriented films.

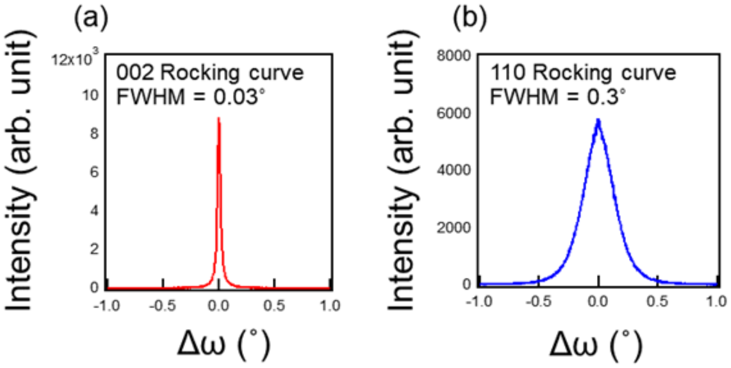

Figure 4.7. Rocking curves (ω-scans) of (001) (a), and (110) (b) $BaSnO_3$ buffers.

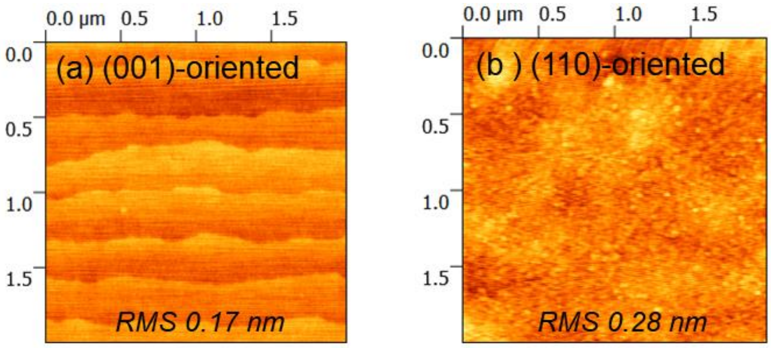

Figure 4.8. AFM images of (001) (a), and (110) (b) $BaSnO_3$ buffers after post annealing with 1100 ˚C for 2 h in air atmosphere.

The surface morphology of (001)- and (110)- oriented $BaSnO_3$ buffers is shown in Figure 4.8(a) and (b), respectively. The AFM image of (001)-oriented film in Figure 4.8(a) presents an atomically flat surface with step-and-terrace structure. On the other hand, the (110)-oriented film shows a rougher surface. In fact, the root mean square (RMS) roughness values of the (001)- and (110)-oriented thin films were 0.17 nm and 0.28 nm, respectively. This suggests that the (001) surface of $BaSnO_3$ is thermodynamically more stable than the (110).

In conclusion, I succeeded in fabricating (001) and (110) orientated single crystalline perovskite $BaSnO_3$ thin films with high crystallinity and flat surfaces by using PLD method. In the next section, the effect of the buffer layer on the crystal growth of (001)-orientated $BaTaO_2N$ thin films will be discussed.

4.3 Buffer layer effect on (001)-oriented $BaTaO_2N$ thin films

$BaTaO_2N$ (cubic, *a* = 0.4113 nm) [104] epitaxial thin films were grown on STO (001) (cubic, *a* = 0.3905 nm) substrate with NPA-PLD method. Prior to the PLD growth, the substrate was annealed for two hours at 1050 ˚C in air to prepare automatically flat surface. A ceramic pellet of $Ba_2Ta_2O_7$ was used as a target, which was obtained by sintering $Ba_2Ta_2O_7$ powder at 1400 ˚C for fifty hours. Details of NPA-PLD method was described in Chapter 2. Briefly, a ceramic pellet of $Ba_2Ta_2O_7$ was ablated by a KrF excimer laser (λ = 248 nm). Energy fluence of the excimer laser was adjusted between 8 mJ and 13 mJ to control the deposition rate at 10 - 13 nm/h. The $Ba_2Ta_2O_7$ target was degraded while repeating deposition run, similar to the $Nb_2O_{4.8}$ target

In this study, (001)-oriented perovskite $BaTaO_2N$ films were fabricated with and without (001)-oriented $BaSnO_3$ buffer layer under the following optimized conditions:

Radical source	: radio frequency with input power 400W
Target	: $BaTaO_X$
Substrate	: STO (001)
Growth temp. (˚C)	: 600 ˚C
Repetition rate	: 3 Hz
Atmosphere	: N_2 gas with $1x10^{-5}$ Torr

Figure 4.9 shows θ-2θ XRD patterns of the $BaTaO_xN_y$ thin films grown on STO (001) substrate with and without $BaSnO_3$ (001) buffer layer. Both films showed peaks at $2\theta \sim 21°$, 30°, and 43° which corresponded to 001, 110, and 002 diffraction from perovskite $BaTaO_2N$, respectively. With this method, perovskite $BaTaO_2N$ with multiple orientation of (001) and (110) was obtained. In general,

the growth orientation of the film relies on the surface energy of each material. I speculated that the lowest-energy surfaces of $BaTaO_2N$ is (110) plane. The difference in surface energies of completing crystal planes will play an important role to determine whether interfacially-driven epitaxy can be achieved. On the other hand, the film deposited on the (001)-oriented $BaSnO_3$ buffer layer exhibited epitaxial growth of (001)-oriented thin film with a suppressed amount of (110)-orientation. However, a trace amount of (110) peak was still observed even after inserting the $BaSnO_3$ buffer layer. Therefore, in order to obtain single orientation $BaTaO_2N$ thin films, I decided to fabricate $BaTaO_2N$ epitaxial thin films on STO (110) substrate.

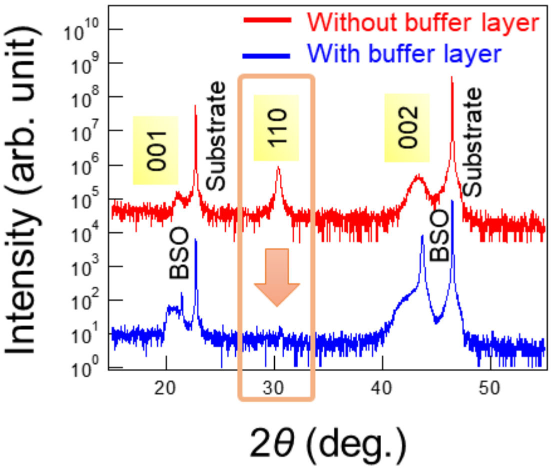

Figure 4.9. θ-2θ XRD patterns of the $BaTaO_xN_y$ thin films fabricated on (001)-oriented $BaSnO_3$ buffer layer and directly grown on $SrTiO_3$ (001) substrate at *T*s of 600 ˚C.

4.4 Buffer layer effect on (110)-oriented $BaTaO_2N$ thin films

The $BaTaO_2N$ film directly grown on STO (110) substrate showed only the diffraction peaks corresponding to *hh*0 diffraction of perovskite crystal (Figure 4.10) without any peaks from impurity phases such as Ta_2O_5, TaON and $BaTaO_x$. However, the crystallinity of the film was low, as seen from the much broadened rocking curve of (110) diffraction with FWHM of ~1.25°. Furthermore, the surface of the film was rather rough, of which root-mean-square (RMS) roughness was ~5 nm.

The θ-2θ XRD pattern of the $BaTaO_2N$ thin film fabricated on the $BaSnO_3$ buffer layer also indicated epitaxial growth of a (110)-oriented perovskite $BaTaO_2N$ thin film. Notably, however, the crystallinity and the surface morphology of the film were much improved (FWHM on (110)-oriented peak = 0.3° (Figure 4.10(b)) and the RMS of surface roughness = ~1 nm) compared with the films directly grown on STO (110) substrate (Figure 4.10(c)). It should also be noted that the crystallinity and the surface morphology of the main layer is strongly related with the crystal quality of $BaSnO_3$ buffer layer.

Figure 4.11 shows X-ray diffraction reciprocal space mapping (RSM) recorded around the (130) reciprocal lattice point of $SrTiO_3$ substrate along [110] and [-110]. The RSM indicated peaks corresponding to the 100 nm thick $BaTaO_xN_y$ and 80 nm thick $BaSnO_3$, together with the peak from $SrTiO_3$ (110). Notably, the $BaSnO_3$ buffer layer was fully relaxed. Consequently, the $BaTaO_xN_y$ thin film was coherently grown on the $BaSnO_3$ buffer layer. In conclusion, the X-ray and AFM results demonstrated that (110)-oriented $BaTaO_xN_y$ film was successfully grown by using PLD method with the aid of $BaSnO_3$ buffer layer, where the $BaSnO_3$ buffer layer improved the crystallinity and surface flatness of the film due to the coherent growth of $BaTaO_xN_y$ on it.

To evaluate chemical composition and larger area surface morphology, SEM-EDX measurements were conducted. Figure 4.12 (a) compares the surface morphology of the $BaTaO_xN_y$ films with and without buffer layer measured by SEM, and Figure 4.12(b) is an EDX spectrum of $BaTaO_2N$ thin films deposited on $BaSnO_3$ buffer layer.

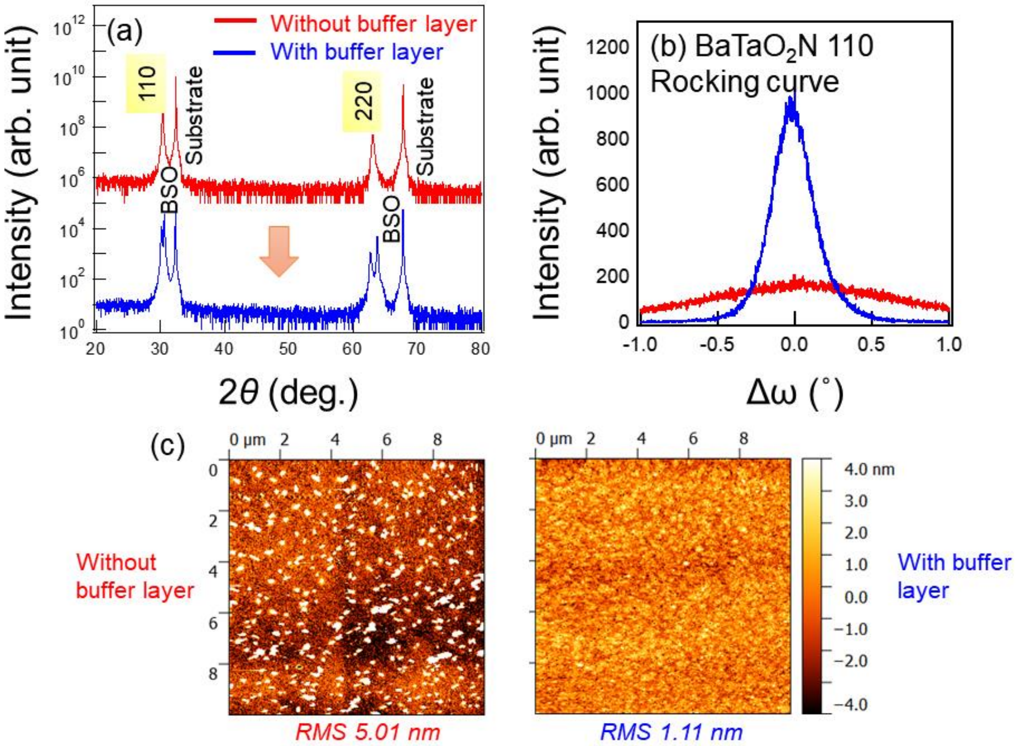

Figure 4.10. (a) θ-2θ XRD patterns, (b) X-ray rocking curves of 110 peak, and (c) AFM images of the $BaTaO_xN_y$ fabricated on (110) $BaSnO_3$ buffer layer and directly grown on $SrTiO_3$ (110) substrate at *T*s of 600 ˚C.

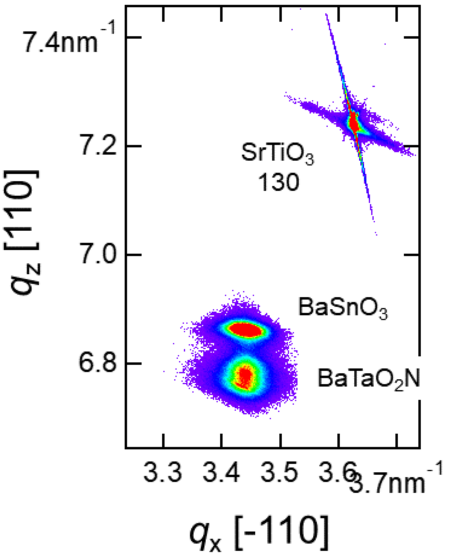

Figure 4.11. Reciprocal space mapping (RSM) around (130) peak of $SrTiO_3$ substrate.

The SEM images of the $BaTaO_xN_y$ films with and without buffer layer showed the same tendency as the AFM images in Figure 4.10(c). That is, even in a large area scale, the $BaTaO_xN_y$ film directly grown on STO substrate had a rougher surface compared to the film grown on $BaSnO_3$ buffer layer. The composition analysis of N/O ratio performed by EDX with ERDA normalization indicated that almost stoichiometric 1.95±0.1:0.99±0.1. On the other hand, the ERDA was mainly used to analyze Ba and Ta because high voltage in EDX is required in order to investigate cations in $BaTaO_2N$ system. With high voltage, the X-ray will penetrate to the buffer and substrate layers. Therefore, the accuracy of the Ba and O atoms will be distracted from those layers. As a result, the Ba/Ta ratio was 0.951 which demonstrated slight deficiency of Ba.

To improve the cation stoichiometry, I decided to increase the Ba content of the sintering target. $Ba_{1.05}TaO_x$ and $Ba_{1.1}TaO_x$ targets were prepared with the same sintering condition as mentioned before. By using these Ba-rich targets, the Ba/Ta ratio was increased to 0.979 and 0.999, respectively. As a consequence, a ceramic target with a nominal composition of $Ba_{1.1}TaO_x$ was needed to obtain stoichiometric thin films ($Ba_{0.99}TaO_{1.95}N_{0.99}$). Buffer layer had no effect on the chemical composition. Hereafter, I refer to this sample as $BaTaO_2N$. Moreover, the chemical composition of the surface $BaTaO_2N$ was studied by XPS. Remarkably, no Sn was detected at the surface of the $BaTaO_2N$ layer, which means that Sn was not diffused from the buffer layer to the film. Figure 4.13 shows the XPS spectrum of Ta $4f_{5/2}$ and $4f_{7/2}$ doublet. All of the observed Ta peaks were assigned to Ta^{5+} bonded to N^{3-} and O^{2-}, as previously reported.

The lattice constants were calculated as a, b = 4.13 Å and c = 4.17 Å. The in-plane lattice slightly expanded from the bulk value due to the epitaxial force from the buffer layer which has the lattice constant of a = 4.13 Å. Slight lattice distortation yielded c/a = 1.008, which is comparable with the previous report (c/a ~ 1.009). I also noted that the lattice constant of $BaTaO_2N$ system is mainly determined by the cations. In conclusion, I succeeded in fabricating single crystalline perovskite

$BaTaO_2N$ thin films with (110)-orientation by PLD method. Moreover, the crystallinity and surface flatness were much improved by inserting $BaSnO_3$ buffer layer.

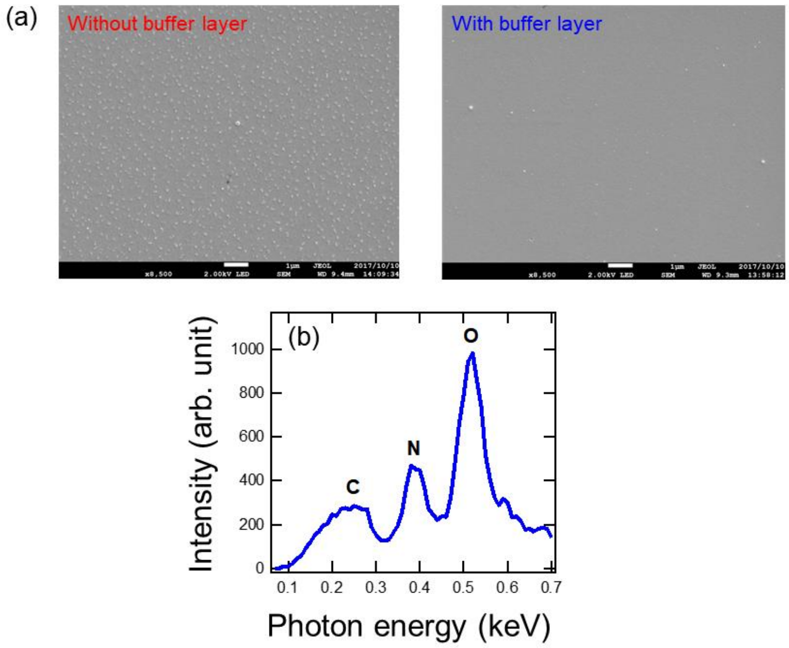

Figure 4.12. (a) SEM images of $BaTaO_2N$ thin films with and without $BaSnO_3$ buffer layer, and (b) EDX spectrum of $BaTaO_2N$ thin film on $BaSnO_3$ buffer layer.

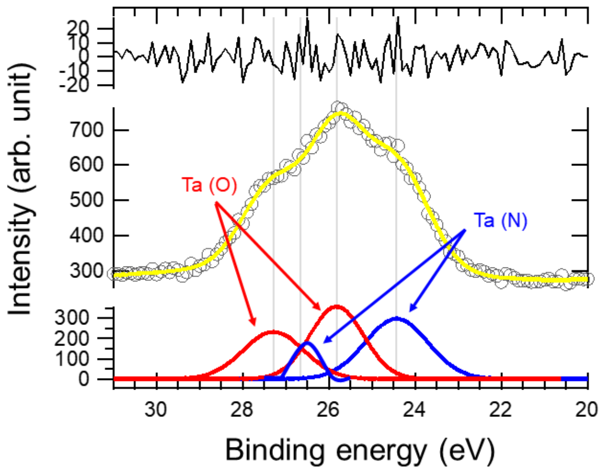

Figure 4.13. Ta 4f XPS spectrum of $BaTaO_2N$ thin film.

4.5 Physical properties of perovskite $BaTaO_2N$

Figure 4.14 shows optical transmittance T, reflectance R, and absorptance A (= $100-T-R$) spectra of the perovskite $BaTaO_2N$ thin films with and without buffer layer together with those of $BaSnO_3$ buffer layer to confirm that the buffer layer did not contribute to the visible light absorption. The absorption spectrum showed clear visible light absorption at the absorption edge around 650 nm (E_g = ~1.9 eV), which is consistent with the previous report. Particularly, stronger absorption in the visible light region with sharper absorption onset was observed in the $BaTaO_2N$ thin film grown on $BaSnO_3$ buffer layer (Figure 4.15). This might be because the buffer layer improved the homogeneity of the film. Small in-gap absorption was observed from 640 nm to 2300 nm possibly due to defect states associated with the above-mentioned oxygen deficiency inside the film or STO (110) substrate arising from high temperature fabrication.

While the crystallinity, the surface morphology, and the optical properties were improved by the $BaSnO_3$ buffer layer, defects in the film were not completely eliminated: Dielectric measurements of the films by using an LCR meter indicated large dielectric loss tangent even for the film on the $BaSnO_3$ buffer layer, suggesting the existence of anion deficiency (Figure 4.16).

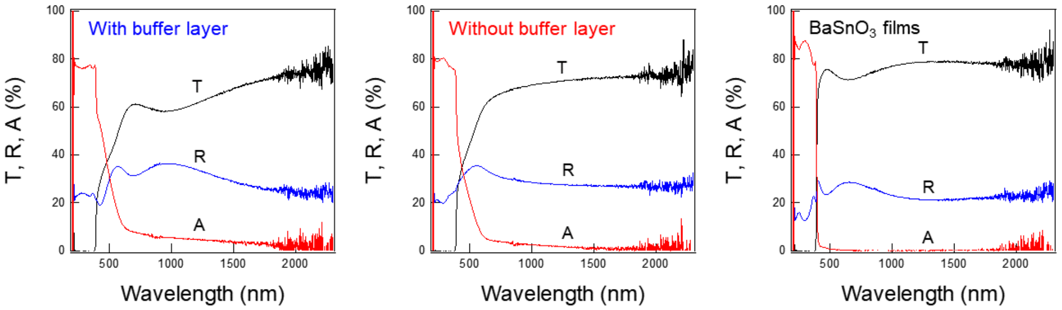

Figure 4.14. Optical transmittance, reflectance and absorptance spectra of perovskite $BaTaO_2N$ films with and without buffer layer and the $BaSnO_3$ buffer layer.

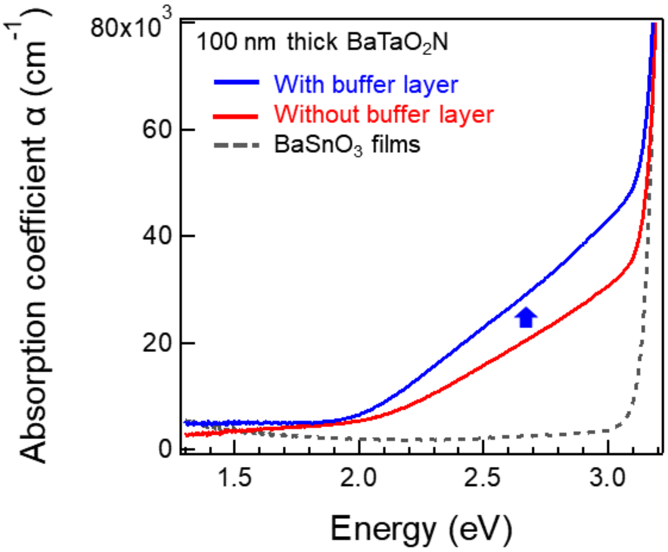

Figure 4.15. Absorption coefficient vs. photon energy plots for the $BaTaO_2N$ films with and without buffer layer and the $BaSnO_3$ buffer.

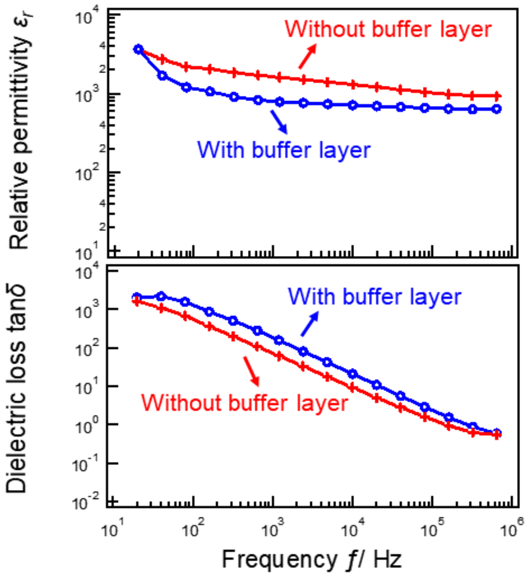

Figure 4.16. The frequency dependent dielectric constant and dielectric loss tangent of the $BaTaO_2N$ film with and without buffer layer.

Photoelectrochemical properties of $BaTaO_2N$ were determined form current-potential curves measured under simulated AM 1.5G light. Figure 4.17 shows the current-potential curves measured by using the $BaTaO_2N$ films with and without $BaSnO_3$ buffer layer as electrodes. The $BaTaO_2N$ film with buffer layer presented higher photocurrent as compared to the $BaTaO_2N$ film without buffer layer.

Notably, use of buffer layer improved of the net photocurrent density from 12 μA/cm^2 to 16 μA/cm^2 at 1.23 V versus RHE, possibly due to enhanced crystallinity. As mentioned before, the $BaTaO_2N$ film without buffer layer had a rough surface with many grains and boundaries due to poor crystallinity. Such surface defects would cause recombination of excited electrons and holes. A similar tendency was also reported in $LaTiO_xN_y$ thin film in which better crystallinity showed higher capacitive currents [105]. Nevertheless, in my opinion, it should be remarked that the photons absorbed at the $BaTaO_2N/BaSnO_3$ interface are not necessarily utilized efficiently because holes generated in the $BaTaO_2N$ film have a higher probability of recombining with the electrons before reaching the surface [106].

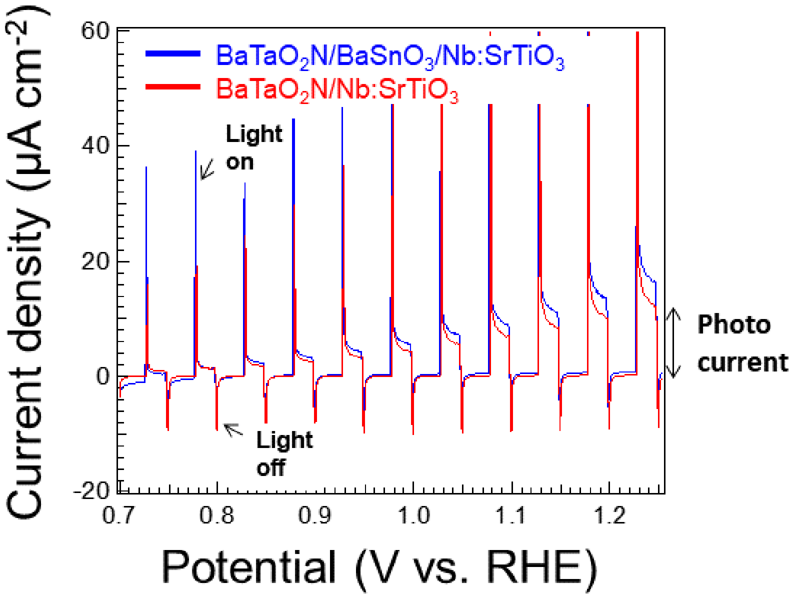

Figure 4.17. Current-potential curves of the $BaTaO_2N$ film with and without $BaSnO_3$ buffer layer.

4.6 Conclusions

In conclusion, (110)-oriented perovskite $BaTaO_2N$ thin films were successfully grown on STO (110) substrate by using nitrogen plasma assisted pulsed laser deposition method. Introduction of a thick $BaSnO_3$ buffer layer improved crystallinity and made the film surface smoother with less precipitations and grain boundaries, resulting in higher absorption in the visible light region. The perovskite $BaTaO_2N$ thin film exhibited E_g of ~1.9 eV (650 nm), which is small enough to absorb almost all visible light radiation. These results indicated that using lattice matched buffer layer with favorable orientation is a promising approach to reduce lattice defects of perovskite $BaTaO_2N$. The preliminary data on photocurrent suggested that the $BaTaO_2N$ film with buffer layer showed higher photocurrent density at 1.23 V versus RHE than the $BaTaO_2N$ without buffer layer. Further improvement of anion stoichiometry by post-annealing would be necessary for obtaining high-quality $BaTaO_2N$ thin films and investigating the relationship between crystallinity vs. permittivity.

Chapter 5

General conclusion

In this thesis, I focused on crystal growth of d^0 transition metal oxynitride thin films by nitrogen plasma assisted pulsed laser deposition (NPA-PLD) for the sake of understanding their photoelectrochemical and physical properties. I achieved substantial improvement of crystal quality by introducing self-seed or buffer layer.

In Chapter 3, I succeeded in fabricating single crystal baddeleyite NbON epitaxial thin films on YSZ (100) substrates by using NPA-PLD technique. In previous researches, bulk powder samples and polycrystalline thin film were synthesized, where the samples did not contain sufficient amounts of N^{3-} and had rough surfaces with grain boundaries. In order to understand the intrinsic physical properties and to achieve high efficiency of photocatalytic activity, single crystalline sample is more suitable than polycrystalline one because it is relatively free from the extrinsic factors such as defects and grain boundaries. For growth of single crystalline baddeleyite NbO_xN_y thin films, Ts $\geq$500 °C was needed to crystallize the baddeleyite phase, of which crystallinity was increased with increasing Ts. However, the color of the film fabricated at high T_S turned black, indicating formation of a large amount of nitrogen deficiency. These results indicate that high T_S is effective for the crystal growth while low T_S is necessary for growing films with good stoichiometry. By inserting self-seed layer, it attained low temperature growth of baddeleyite NbON thin films with almost stoichiometric chemical composition. The baddeleyite NbON thin film showed E_g value of ~2.3 eV, which is smaller than that of β-TaON as expected. These results indicated that low temperature epitaxial growth is a promising approach to investigate the intrinsic properties of baddeleyite NbON but still is insufficient to avoid the reduction of Nb perfectly. Further improvement of anion stoichiometry and suppression of multiple domain structure would be necessary for obtaining high-quality NbON thin films with high electron mobility.

In Chapter 4, I focused on the lowest bandgap material in perovskite-type quaternary oxynitride semiconductors with chemically stable Ta^{5+} ions, $BaTaO_2N$. There were only a few reports on the synthesis of $BaTaO_2N$ epitaxial thin films due to the lack of commercially available single crystalline substrate with good lattice matching. In this study, I fabricated $BaTaO_2N$ epitaxial thin films with improved crystallinity on $SrTiO_3$ substrate by inserting a matched $BaSnO_3$ buffer layer. The $BaTaO_2N$ film directly grown on STO (110) substrate at Ts = 600 ºC was stoichiometric without impurity phases such as Ta_2O_5, TaON and $BaTaO_x$. However, the crystallinity of the film was low (FWHM of the (110) rocking curve = ~1.25°). Furthermore, the surface of the film was rather rough, of which root-mean-square (RMS) roughness was ~5 nm. On the other hand, the $BaTaO_2N$ thin film fabricated on the $BaSnO_3$ buffer layer indicated much improvement in both crystallinity and surface morphology (FWHM of (110) rocking curve = 0.3° and RMS surface roughness = ~1 nm), compared to the films directly grown on STO (110) substrate. Both of the $BaTaO_2N$ films fabricated with and without buffer layer showed clear visible light absorption with absorption edges of ~1.9 eV (650 nm), being consistent with the previous report. On the other hand, stronger absorption in the visible light region with sharper absorption onset was observed in the $BaTaO_2N$ film grown on the $BaSnO_3$ buffer layer. As for photoelectrochemical properties, the net photocurrent density of the $BaTaO_2N$ films on buffer layer showed improvement in current density. While the crystallinity, the surface morphology, and the optical properties were improved by the $BaSnO_3$ buffer layer, defects in the film were not completely removed: Dielectric measurements indicated large dielectric loss tangent even on the $BaSnO_3$ buffer layer, suggesting the existence of anion deficiency.

In conclusion, I have succeeded in synthesizing epitaxial thin films of narrow band gap oxynitrides, baddeleyite NbON and perovskite $BaTaO_2N$, by inserting a self-seed layer or a buffer layer. The crystallinity and physical/photochemical properties of the NbON and $BaTaO_2N$ were improved by using the seed/buffer layer. The present study demonstrated that improving the crystallinity of the thin films by using seed/buffer layer is an effective way to improve photoelectrochemical solar water splitting properties.

Appendix chapter A

Synthesis of rutile NbON: growth, crystal structure, and physical properties

A.1 Introduction

As mention in Chapter 3, rutile NbON with tetragonal crystal symmetry could not only suppress the multiple domain in baddeleyite structure but also reduce the optical band gap. As referred to TiO_2, different polymorphs generally show different optical properties. That is, the optical band gaps of TiO_2 were reported to be ~3.0 eV for rutile [90-91], ~3.4 eV for anatase [92] and ~3.3 eV for brookite [93]. With this tendency, rutile NbON is expected to have a smaller band gap than baddeleyite one. However, rutile NbON has been scarcely reported so far, mainly due to the difficulty in synthesis. In this study, I fabricated single crystal rutile NbON epitaxial thin films and investigated its optical and transport properties.

A.2 Preparation of the substrate

In this study, single crystalline TiO_2 (110) was used as a substrate, although large lattice mismatch between NbON and substrate (~8%) might generated tensile strain leading to dislocation defects in the film.

Cleaning of substrate surface before film fabrication is generally very important. Namely, in order to promote perfect epitaxial growth of film, a clean substrate surface is required. However, TiO_2 is unstable at high temperature (Ts >500 °C) in vacuum condition, due to generation of oxygen vacancies. It is not suitable to measure transport properties on reduce TiO_2 substrate, because the incorporation of oxygen vacancy reduces the valence state of Ti to Ti^{3+}, which releases conduction electrons and prevents the accurate measurement of transport properties of the thin film layer.

A.3 Fabrication condition of rutile NbO_xN_y

The first trial was done on TiO_2 (110) substrate with the same condition for the baddeleyite NbON, Ts = 600 ˚C, Figure A.1(a) shows a θ-2θ XRD diffraction pattern indicating peaks from rock-salt (body centered cubic) structure. The RHEED pattern (Figure A.1(b)) of the film showed intense streaks which represent a single-crystalline nature. That is, at Ts = 600 ˚C, rutile NbON was not formed. The obtained film showed dark to black color, indicating anion deficiency as discussed before.

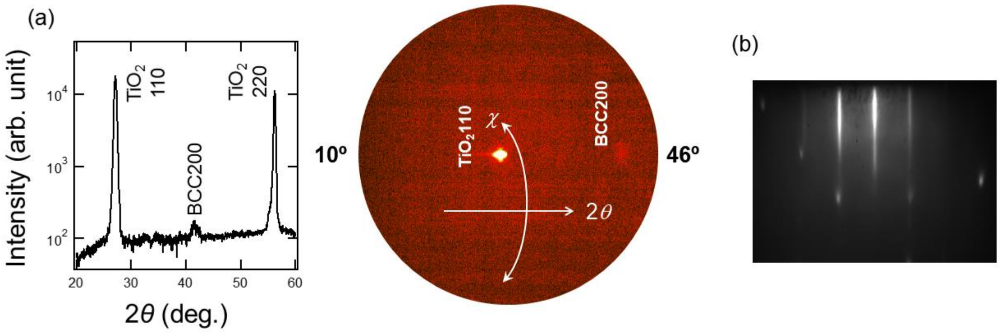

Figure A.1. (a) θ-2θ XRD pattern and (b) RHEED pattern of NbO_xN_y film grown on TiO_2 (110) substrate at Ts = 600 ˚C.

Next, I increased Ts to obtain the unable rutile phase [89]. The experimental conditions are as follows:

Radical source : radio frequency with input power 350W

Target : $Nb_2O_{4.8}$ (commercial target)

Substrate : TiO_2 (110)

Growth temp. (˚C) : 650 ˚C

Repetition rate : 3 Hz

Atmosphere : O_2 gas with $1x10^{-6}$ Torr

N_2 gas with $1x10^{-5}$ Torr

Seed layer : with and without TiO_2 seed layer

Figure A.2 shows θ-2θ XRD patterns of the NbO_xN_y thin films grown on TiO_2 (110) substrate at Ts = 650 ˚C with and without TiO_2 seed layer. The films fabricated on a TiO_2 seed layer, which has smaller lattice parameters, showed that the film had poor crystallinity. On the other hands, the film directly grown on TiO_2 (110) substrate showed more intense diffraction peaks than the NbO_xN_y thin films grown on the seed layer although both of them had rutile structure, as seen from the 110 and 220

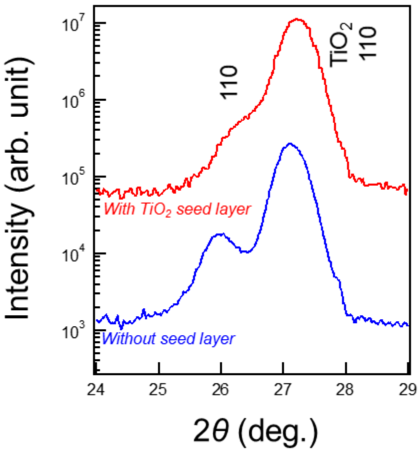

Figure A.2. θ-2θ XRD patterns of the NbO_xN_y thin films grown on TiO_2 (110) substrate with and without TiO_2 seed layer.

diffraction peaks observed at 2θ ~ 26˚ and 54˚, respectively, without impurity phases. The surface morphology of the films was analyzed by AFM, SEM and RHEED. Figure A.3 compares the surfaces between the rutile NbO_xN_y films grown with and without TiO_2 seed layer. With TiO_2 seed layer, the surface roughness was significantly suppressed possibly due to the strain from the seed layer. Another possibility is that the seed layer behaved as a preliminary layer for achieving a smooth and clean surface on the substrate, although the detailed mechanism is unclear. It can be said that Ts of 650 ˚C is suitable to form a rutile phase and that the seed layer enhances the surface flatness but suppresses the crystallinity.

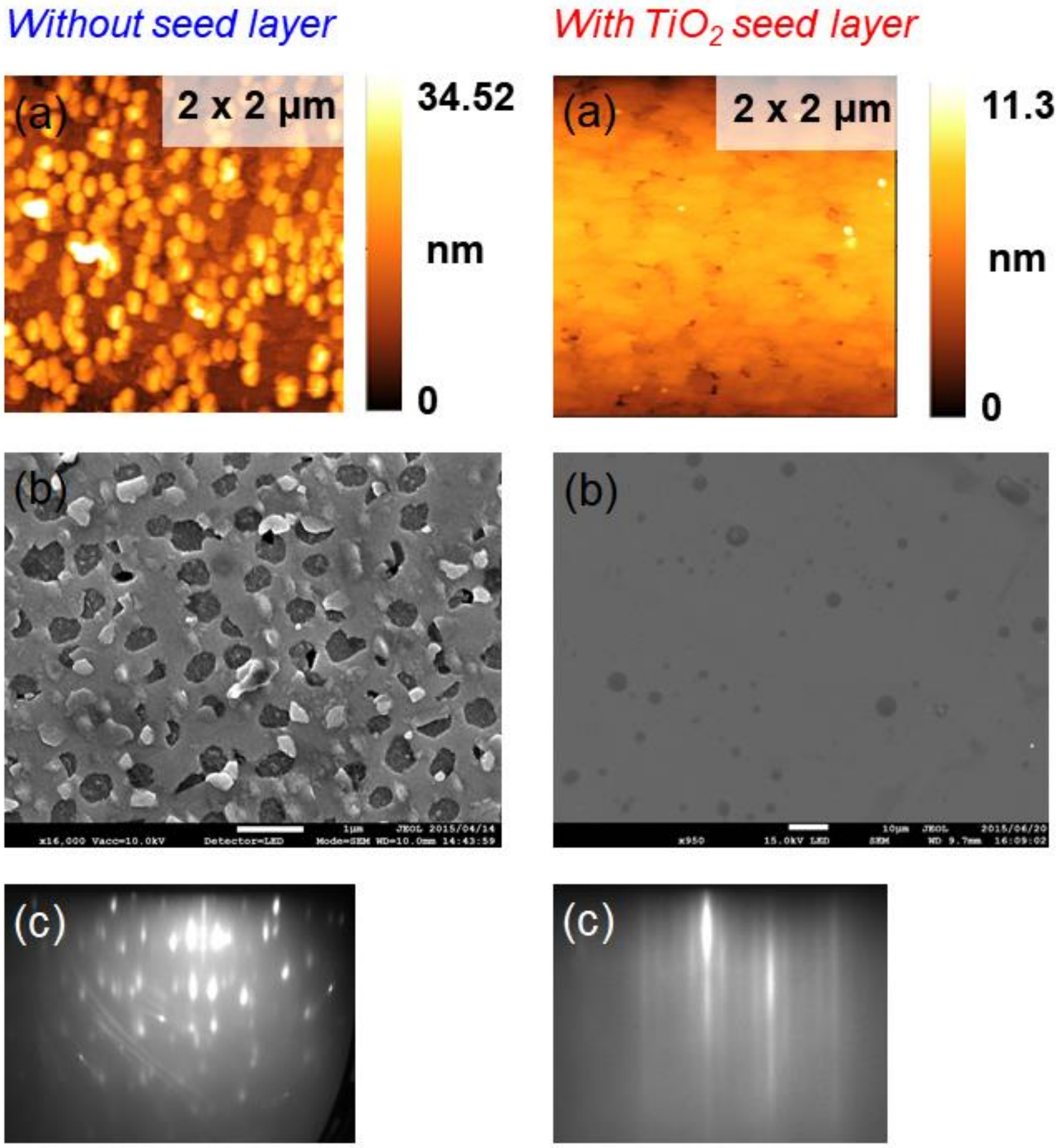

Figure A.3. (a) AFM images, (b) SEM images, and (c) RHEED patterns of rutile NbO_xN_y films with and without TiO_2 seed layer.

A.4 Cross-section image and chemical composition of rutile NbO_xN_y thin films by TEM-EDX

The chemical compositions of a rutile NbO_x film, which was fabricated with the same condition as NbO_xN_y but without N_2 gas introduction, was evaluated by transmission electron microscopy equipped with EDX (TEM-EDX) for examining cation contamination from substrate and its effect on film quality. Figure A.4 shows intermixing between film and substrate with surface defects.

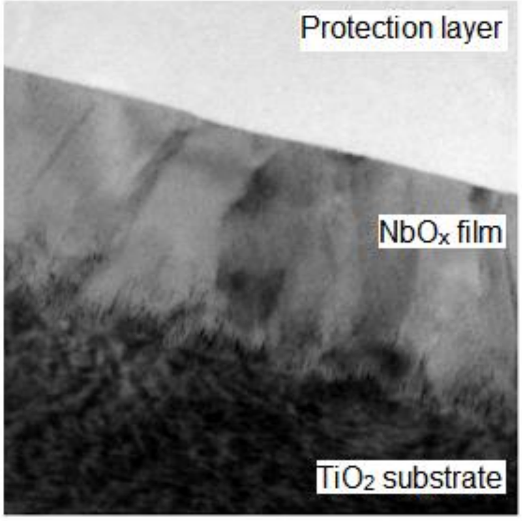

Figure A.4. Cross-sectional TEM image of NbO_x thin film directly grown on TiO_2 (110) substrate.

This implies that Ti ions might diffuse from the substrate to the film, resulting in the formation of defects under high *T*s. The EDX data in Figure A.5(a) also supports the diffusion of Ti ions. On the other hand, no Nb ions were diffused into the TiO_2 substrate. The EDX data in Figure A.5(b) revealed that the film could be regarded as oxygen-rich NbO_2 with 8% Ti. Figure A.6 is a SEM-EDX spectrum of the rutile NbO_xN_y film. Combining SEM-EDX and TEM-EDX data, it is suggested that the rutile NbO_xN_y had an oxygen-rich composition with several % of Ti. It is speculated that the chemical composition of the films was NbO_2N doped with Ti. In conclusion, pure rutile NbON without impurities doping was not obtained in this study.

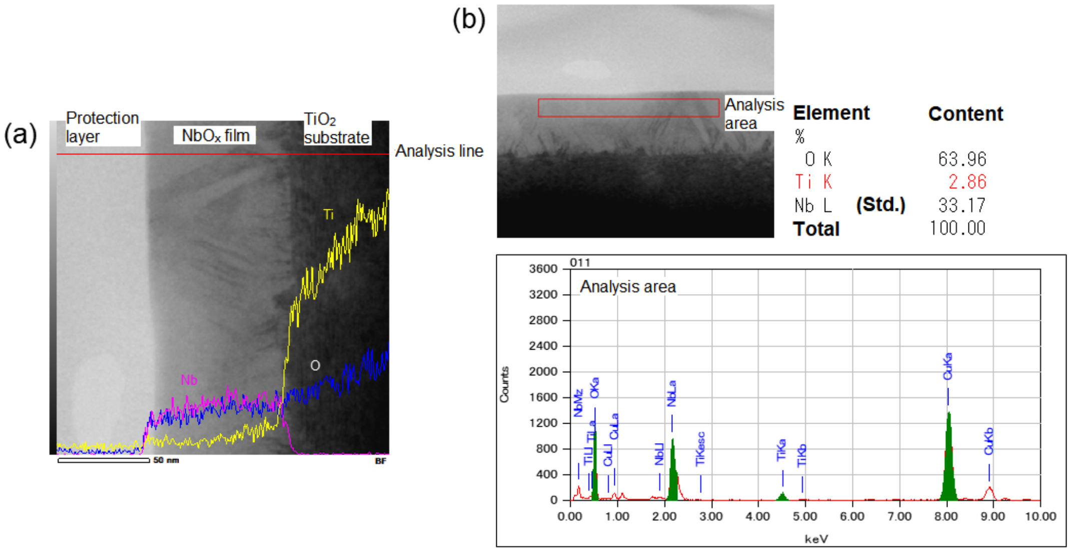

Element %		Content
O K		63.96
Ti K		2.86
Nb L	(Std.)	33.17
Total		100.00

Figure A.5. (a) Composition analysis along the depth direction, and (b) EDX spectrum on the surface of NbO_x thin film grown on TiO_2 (110) substrate.

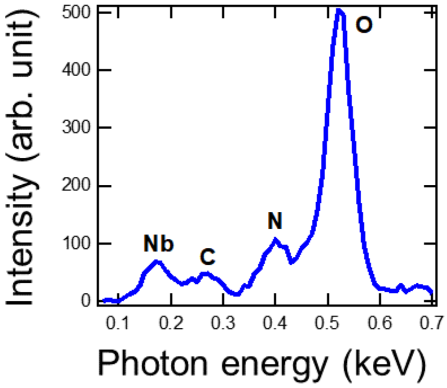

Figure A.6. EDX spectrum of the rutile NbO_xN_y thin film directly grown on TiO_2 (110) substrate.

A.5 Physical properties of rutile NbO_xN_y

Figure A.7 shows optical transmittance *T*, reflectance *R*, and absorptance *A* (= 100−*T*−*R*) spectra of the rutile NbO_xN_y thin film directly grown on TiO_2 (110) substrate. An absorption edge was located around 560 nm (~ 2.22 eV) which is slightly smaller than that of baddeleyite NbON, as discussed in Chapter 3. Moreover, the absorptance of rutile NbO_xN_y was larger than that of baddeleyite phase. However, I also observed large in-gap absorption possibly due to nitrogen deficiency.

From the Tauc plot, the optical band gap of rutile NbO_xN_y was considered to be indirect one.

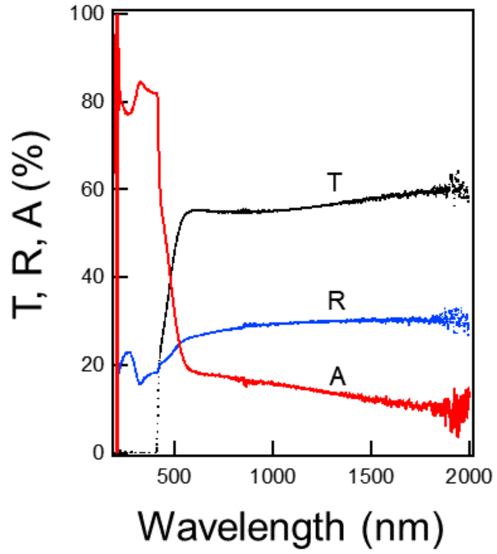

Figure A.7. Optical transmittance, reflectance and absorptance spectra of rutile NbO_xN_y thin film grown on TiO_2 (110) substrate at *T*s = 650 ˚C.

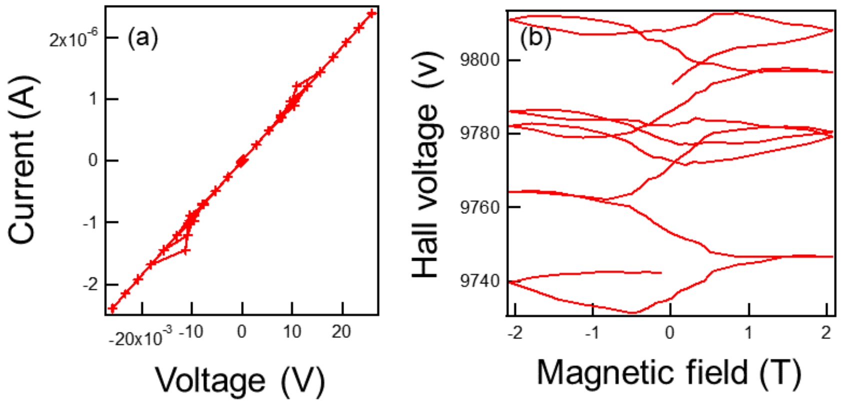

Figure A.7. (a) *I-V* curve of rutile NbO_xN_y film on TiO_2 (110) substrate, and (b) Hall voltage as a function of magnetic field.

The electrical properties of the rutile NbO_xN_y thin film were also investigated. As shown in Figure A.8(a), the *I-V* curve was a straight line, implying that Ohmic contact was achieved. The electrical resistivity of the film was 2.3×10^{-2} Ωcm.

---

* The physical properties shown in this chapter were measured from the NbO_xN_y samples with Ti contamination.

But I failed to measure Hall resistance, as shows in Figure A.8(b), probably due to poor crystallinity or large surface roughness, which would cause carrier trapping. Thus, carrier density and Hall mobility could not be evaluated.

A.6 Conclusions

In conclusion, rutile NbO_xN_y thin films were successfully grown on TiO_2 (110) substrates by using nitrogen plasma assisted pulsed laser deposition method. But it was failed to obtain stoichiometric phase without Ti impurities. The rutile NbON thin film showed an E_g value of 2.22 eV, which is smaller than that of β-TaON and baddeleyite NbON.

Bibliography

[1] A. Fujishima, and K. Honda, *Nature* **238**, 37 (1972).

[2] A. Kudo, and Y. Miseki, *Chem. Soc. Rev.* **38**, 253 (2009)

[3] A.J. Bard, and M.A. Fox, *Acc. Chem. Res.* **28**, 141 (1995)

[4] H.W. Eng, P.W. Barnes, B.M. Auer, and P.M. Woodward, *J. Solid State Chem.* **175**, 94 (2003)

[5] M. Jansen, and H.P. Letschert, *Nature* **404**, 980 (2000)

[6] B. Modak, and S.K. Ghosh, *J. Phys. Chem. C.* **120(13)**, 6920 (2016)

[7] J. Portier, G. Campet, C.W. Kwon, J. Etourneau, and M.A. Subramanian, *Int. J. Inorg. Mater.* **3**, 1091 (2001)

[8] J. Portier, G. Campet, A. Poquet, C. Marcel, and M.A. Subramanian, *Int. J. Inorg. Mater.* **3**, 1039 (2001)

[9] L. Pauling, *J. Am. Chem. Soc.* **54**, 3570 (1932)

[10] J. Portier, H.S. Hilal, I. Saadeddin, S.J. Hwang, M.A. Subramanian, and G. Campet, *Prog. Solid State Ch.* **32**, 207 (2004)

[11] F.D. Quarto, C. Sunseri, S. Piazza, and M.C. Romano, *J. Phys. Chem. B* **101**, 2519 (1997)

[12] L. Pauling, *The Nature of Chemical Bond; Cornell University Press: Ithaca, NY; Chapter 3* (1960)

[13] J.C. Phillips, *Bonds and Bands in Semiconductors, Academic Press: NY, London* (1973)

[14] J.A. Alonso, N.H. March, *Electrons in Metals and Alloys; Academic Press: NY, London* (1989) and C. Kittel, *Introduction to Solid State Physics, 3rd ed.; John Wiley & Sons: NY; Chapter 3* (1966)

[15] J.A. Herron, J. Kim, A.A. Upadhye, G.W. Huber, and C.T. Maravelias, *Energy Environ. Sci.* **8**, 126 (2015)

[16] A.G.S. Prado, L.B. Bolzon, C.P. Pedroso, A.O. Moura, and L.L. Costa, *Appl. Catal., B* **82**, 219 (2008)

[17] R. Asai, H. Nemoto, Q. Jia, K. Saito, A. Iwase, and A. Kudo, *Chem. Commun.* **50**, 2543 (2014)

[18] A. Kudo, K. Ueda, H. Kato, and I. Mikami, *Catal. Lett.* **53**, 229 (1998)

[19] H. Kato, and A. Kudo, *J. Phys. Chem. B* **106**, 5029 (2002)

[20] H. Kato, H. Kobayashi, and A. Kudo, *J. Phys. Chem. B* **106**, 12441 (2002)

[21] H. Gerisher, and M. Lubke, *Ber. Bunsenges. Phys. Chem.* **87**, 123 (1983)

[22] A.J. Bard, and M.S. Wrighton, *J. Electrochem. Soc.* **124**, 1706 (1977)

[23] C.M. Fang, E. Orhan, G.A. De Wijs, H.T. Hintzen, R.A. De Groot, R. Marchand, J.Y. Saillard, and G. De With, *J. Mater. Chem.* **11**, 1248 (2001)

[24] M. Jansen, and H. Letshert, *Nature* **404**, 980 (2000)

[25] T. Takata, P. Chengsi, and K. Domen, *Sci. Technol. Adv. Mater.* **16**, 033506 (2015)

[26] K. Maeda, and K. Domen, *J. Phys. Chem. C* **111**, 7851 (2007)

[27] B. Siritanaratkul, K. Maeda, T. Hisatomi, and K. Domen, *ChemSusChem.* **4**, 74 (2011)

[28] B. Armytage, and B.E.F. Fender, *Acta. Crystallogr. B* **30**, 809 (1974)

[29] R. Abe, *J. Photochem. Photobiol. C: Photochem. Rev.* **11**, 179 (2010)

[30] R.D. Shannon, and C.T. Prewitt, *Acta. Crystallogr. B* **25**, 925 (1969)

[31] A. Fuertes, *J. Mater. Chem.* **22**, 3293 (2012)

[32] F. Tessier, and R. Marchand, *J. Solid State Chem.* **171**, 143 (2003)

[33] B.L. Cushing, V.L. Kolesnichenko, and C.J. O’Connor, *Chem. Rev.* **104**, 3893 (2004)

[34] P. Antoine, R. Assabaa, P. L’haridon, R. Marchand, and Y. Laurent, *Mater. Sci. Eng. B* **5**, 43 (1989)

[35] M. Yang, J. Oro’Sole, A. Kusmartseva, A. Fuertes, and J.P. Attfield, *J. Am. Chem. Soc.* **9**, 4823 (2010)

[36] Y. Masubuchi, S.-K. Sun, and S. Kikkawa, *Dalton Trans.* **44**, 10570 (2015)

[37] K. Kato, H. Kondo, M. Sakashita, and S. Zaima, *Thin Solid Films* **518**, S226 (2010)

[38] A. Suzuki, Y. Hirose, D. Oka, S. Nakao, T. Fukumura, S. Ishii, K. Sasa, H. Matsuzaki, and T. Hasegawa, *Chem. Mater.* **26(2)**, 976 (2014)

[39] K. Watanabe, and T. Tatsumi, *Appl. Phys. Lett.* **76**, 2940 (2000)

[40] I. Marozau, A. Shkabko, M. Dobeli, T. Lippert, D. Logvinovich, M. Mallepell, C.W. Schneider, A. Weidenkaff, and A. Wokaun, *Materials* **2**, 1388 (2009)

[41] M. Pichler, W. Si, F. Haydous, H. Tellez, J. Druce, E. Fabbri, M.E. Kazzi, M. Dobeli, S. Ninova, U. Aschauer, A. Wokaun, D. Pergolesi, and T. Lippert, *Adv. Funct. Mater.* **27**, 1605690 (2017)

[42] T.N. Bondarenko, V.N. Uvarov, S.V. Borisenko, Y.A. Teterin, V.P. Dzeganovski, A.M. Sych, and Y. A. Titiv, *J. Korean Phys. Soc.* **32**, S65 (1998)

[43] T. Ukita, Y. Hirose, S. Ohno, K. Hatabayashi, T. Fukumura, and T. Hasegawa, *J. Appl. Phys.* **111**, 07D909 (2012)

[44] S. Havelia, S. Wang, K. R. Balasubramaniam, and P. A. Salvador, *J. Solid State Chem.* **182**, 1603 (2009)

[45] S.-Y. Ting, P.-J. Chen, H.-C. Wang, C.-H. Liao, W.-M. Chang, Y.-P. Hsieh, and C.C. Yang, *J. Nanomater.* 929278 (2012)

[46] I. Akasaki, H. Amano, Y. Koide, K. Hiramatsu, and N. Sawaki, *J. Cryst. Growth* **98**, 209 (1989)

[47] K. Matsubara, P. Fons, A. Yamada, M. Watanabe, and S. Niki, *Thin Solid Films* **347**, 238 (1999)

[48] A. Suzuki, Y. Hirose, D. Oka, S. Nakao, T. Fukumura, and T. Hasegawa, *Jpn. J. Appl. Phys.* **54**, 080303 (2015)

[49] D. Oka, Y. Hirose, T. Fukumura, and T. Hasegawa, *Cryst. Growth Des.* **14**, 87 (2014)

[50] J. Takahashi, Y. Hirose, D. Oka, S. Nakao, C. Yang, T. Fukumura, I. Harayama, D. Sekiba, and T. Hasegawa, *Appl. Phys. Lett.* **107**, 231906 (2015)

[51] L. Guan, D. Zhang, X. Li, and Z. Li, *Nucl. Instrum. Meth.* **266**, 57 (2008)

[52] C. Kittel, *Introduction to Solid State Physics*, Wiley, New York (2004)

[53] C.J. Tung, J.C. Ashley, and R.H. Ritchie, *Surf. Sci.* **81**, 427 (1979)

[54] S. Hasegawa, *Reflection High-Energy Electron Diffraction*, Characterization of Materials, 1925 (2012)

[55] S. Ohashi, M. Lippmaa, N. Nakagawa, H. Nagasawa, H. Koinuma, and M. Kawasaki, *Rev. Sci. Instrum.* **70**, 178 (1999)

[56] B.B. He, U. Preckwinkel, and K.L. Smith, *Adv. X-ray Anal.* **43**, 273 (2000)

[57] G. Binning, C. Quate, and C. Gerber, *Phys. Rev. Lett.* **56**, 930 (1986)

[58] B. Cappella, and G. Dietler, *Surf. Sci. Rep.* **34**, 1 (1999)

[59] JEOL, *energy table for EDX analysis*, JEC6101C602A, Japan

[60] I. Harayama, K. Nagashima. Y. Hirose, H. Matsuzaki, and D. Sekiba, *Nucl. Instruments Methods Phys. Res. B* **384**, 61 (2016)

[61] W. Assmann, H. Huber, Ch. Steinhausen, M. Dobler, H. Gluckler, and A. Weidinger, *Nuclear Instruments and Methods in Physics Research B* **89**, 131 (1994)

[62] L.J. van der Pauw, *Philips Res. Repts.* **13**, 1 (1958)

[63] Agilent Impedance measurement handbook: a guide to measurement technology and techniques 4th edition, *Agilent Technology* (2013)

[64] Z. Chen, T.F. Jaramillo, T.G. Deutsch, A. Kleiman-Shwarsctein, A.J. Forman, N. Gaillard, R. Garland, K. Takanabe, C. Heske, M. Sunkara, E.W. McFarland, K. Domen. E.L. Miller, J.A. Turner, and H.N. Dinh, *J. Mater. Res.* **25**, 3 (2010)

[65] G. Wang, Y. Ling, H. Wang, X. Lu, and Y. Li, *J. Photochem. Photobiol. C: Photochem. Rev.* **19**, 35 (2014)

[66] Z. Chen, H.N. Dinh, and E. Miller, *Photoelectrochemical Water Splitting*, Springer, New York

(2013)

[67] G. Hitoki, T. Tanaka, J.N. Kondo, M. Hara, H. Kobayashi, and K. Domen, *Chem. Commun.* **16**, 1698 (2002)

[68] W.-J. Chun, A. Ishikawa, H. Fujisawa, T. Takata, J.N. Kondo, M. Hara, M. Kawai, Y. Matsumoto, and K. Domen, *J. Phys. Chem. B* **107(3)**, 1798 (2003)

[69] M. Hara, G. Hitoki, T. Takata, J.N. Kondo, H. Kobayashi, and K. Domen, *Catal. Today* **78**, 555 (2003)

[70] M. Higashi, K. Domen, and R. Abe, *J. Am. Chem. Soc.* **134(16)**, 6968 (2012)

[71] R. Abe, T. Takata, H. Sugihara, and K. Domen, *Chem. Commun.* **30**, 3829 (2005)

[72] P.-D. Dr. J. Strahle, *Z. Anorg. Allg. Chem.* **402**, 47 (1973)

[73] G. Hitoki, A. Ishikawa, T. Takata, J.N. Kondo, M. Hara, and K. Domen, *Chem. Lett.* **31**, 736 (2002)

[74] A. Kasahara, K. Nukumizu, G. Hitoki, T. Takata, J.N. Kondo, M. Hara, H. Kobayashi, and K. Domen, *J. Phys. Chem. A* **106(29)**, 6750 (2002)

[75] M. Hara, T. Takata, J.N. Kondo, and K. Domen, *Catal. Today* **90**, 313 (2004)

[76] M.-W. Lumey, and R. Dronskowski, *Z. Anorg. Allg. Chem.* **631**, 887 (2005)

[77] H.W. Eng, P.W. Barnes, B.M. Auer, and P.M. Woodward, *J. Solid State Chem.* **175**, 94 (2003)

[78] R. Kikuchi, T. Kouzaki, T. Kurabuchi, and K. Hato, *Electrochemistry* **9**, 711 (2015)

[79] V.M. Weishaupt, and J. Strahle, *Z. Anorg. Allg. Chem.* **429**, 261 (1977)

[80] M. Masanobu, K. Domen, and R. Abe, *J. Am. Chem. Soc.* **134**, 6968 (2012)

[81] R. Kikuchi, T. Kouzaki, T. Kurabuchi, and K. Hato, *Electrochemistry* **83(9)**, 711 (2015)

[82] H. Aoki, Y. Syono, and R.J. Hemley, *Physics Meets Mineralogy: Condensed Mater Physics in the Geosciences*, Cambridge University Press (2008)

[83] M. Mukaida, Y. Takano, K. Chiba, T. Moriya, M. Kusunoki, and S. Ohshima, *Jpn. J. Appl. Phys.*

38, L926 (1999)

[84] A.G. Roy, *J. Appl. Phys.* **91**, 8076 (2002)

[85] T. Bredow Dr., M.-W. Lumey, R.Dronskowski Prof. Dr., H. Schilling, J. Pickardt, and M. Lerch Prof. Dr., *Z. Anorg. Allg. Chem.* **629**, 2173 (2003)

[86] J. Tao, J.W. Chai, L.M. Wong, Z. Zhang, J.S. Pan, and S.J. Wang, *J. Solid State Chem.* **204**, 27 (2013)

[87] E. Rosencher, and B. Vinter, *Optoelectronics*, Cambridge (2004)

[88] J.I. Pankove, *Optical Processes in Semiconductors,* Dover Publication (2010)

[89] T. Bredow Dr., M.-W. Lumey, R. Dronskowski Prof. Dr., H. Schilling, J. Pickardt, and M. Lerch Prof. Dr., *Z. Anorg. Allg. Chem.* **632**, 1157 (2006)

[90] J. Pascual, J. Camassel, and H. Mathieu, *Phys. Rev. B* **18**, 5606 (1978)

[91] A. Amtout, and R. Leonelli, *Phys. Rev. B* **51**, 6842 (1995)

[92] H. Tang, F. Levy, H. Berger, and P.E. Schmid, *Phys. Rev. B* **52**, 7771 (1995)

[93] A. Mattsson, and L. Osterlund, *J. Phys. Chem. C* **114**, 14121 (2010)

[94] B. Ravel, Y.-I. Kim, P.M. Woodward, and C.M. Fang, *Phys. Rev. B* **73**, 184121 (2006)

[95] Y.-I. Kim, P.M. Woodward, K.Z. Baba-Kishi, and C.W. Tai, *Chem. Mater.* **16(7)**, 1267 (2004)

[96] C. Wang, T. Hisatomi, T. Minegishi, Q. Wang, M. Zhong, M. Katayama, J. Kubota, and K. Domen, *J. Phys. Chem. C* **120(29)**, 15758 (2016)

[97] K. Ueda, T. Minegishi, J. Clune, M. Nakabayashi, T. Hisatomi, H. Nishiyama, M. Katayama, N. Shibata, J. Kubota, T. Yamada, and K. Domen, *J. Am. Chem. Soc.* **137(6)**, 2227 (2015)

[98] Y.-I. Kim, W. Si, P.M. Woodward, E. Sutter, S. Park, and T. Vogt, *Chem. Mater.* **19(3)**, 618 (2007)

[99] C.W. Jones, P.D. Battle, P. Lightfoot, and W.T.A. Harrison, *Acta. Cryst.* **C45**, 365 (1989)

[100] A. Prakash, P. Xu, A. Faghaninia, S. Shukla, J.W. Ager III, C.S. Lo, and B. Jalan, *Nat. Commun.*

8, 15167 (2017)

[101] J. Shiogai, K. Nishihara, K. Sato, and A. Tsukazaki, *AIP Advances* **6**, 065305 (2016)

[102] H.J. Kim, U. Kim, H.M. Kim, T.H. Kim, H.S. Mun, B.G. Jeon, K.T. Hong, W.J. Lee, C. Ju, K.H. Kim, and K. Char, *Appl. Phys. Express* **5**, 061102 (2012)

[103] H. Mizoguchi, H.W. Eng, and P.M. Woodward, *Inorg. Chem.* **43**, 1667 (2004)

[104] F. Pros, R. Marchand, Y. Laurent, P. Bacher, and G. Roult, *Mater. Res. Bull.* **23**, 1447 (1988)

[105] M. Pichler, W. Si, F. Haydous, H. Tellez, J. Druce, E. Fabbri, M.E. Kazzi, M. Dobeli, S. Ninova, U. Aschauer, A. Wokaun, D. Pergolesi, and T. Lippert, *Adv. Funct. Mater.* **27**, 1605609 (2017)

[106] C. Wang, T. Hisatomi, T. Minegishi, M. Nakabayashi, N. Shibata, M. Katayama, and K. Domen, *J. Mater. Chem. A* **4**, 13837 (2016)